

ABSTRACT

Folkert, Karalyn Faith. Metrology Artifact Design. (Under the direction of Thomas A. Dow)

Part acceptance is based on dimensional inspection by comparison to the tolerance specifications of the part drawing. These measurements are often taken on Coordinate Measuring Machines (CMMs); but the dynamics of the machine will influence the overall measurement. Traditionally, a calibration artifact determines the static influences of the machine such as machine geometry. The goal of this project is to design and fabricate a calibration artifact that will test a CMM both statically and dynamically and determine the effects of those influences.

The artifact developed is a ring gauge (6" ID, 8" OD, 1" thickness) that represents the typical size of parts of interest. The ring is 17-4PH stainless steel with a plated layer of electroless nickel (150 μ m) on the surface. Each face of the ring was diamond turned to a mean surface finish of 37nm RMS due to tool damage and machine error. Sine wave features were machined on the inside and outside diameter (ID and OD) of the ring using a fast tool servo. The wavelength of the sine wave varies continuously along the surface from long wavelength to short wavelength and back to the starting long wavelength over one revolution of the ring. The actual spatial wavelength of the wave sequences from 0.4mm to 6.4mm. The machined peak-to-valley (PV) is within 4% of the desired PV of 10 μ m. A reference flat surface was also machined on the ID and OD for static measurements.

The final artifact is to be measured using a similar measurement strategy as a part to be measured; the same probe diameter is used with various measurement speeds in one orientation. The transfer function of the CMM dynamics is found by comparing the accepted swept sine wave with the measured wave. Each different speed defines a frequency range of the transfer function. By using this artifact to define the magnitude and phase characteristics of the dynamic system, the operator can make decisions referring to the machine's capabilities that exhibit an anticipated error and uncertainty in a measurement.

METROLOGY ARTIFACT DESIGN

KARALYN F. FOLKERT

A thesis submitted to the Graduate Faculty of
North Carolina State University
in partial fulfillment of the
requirements for the Degree of
Master of Science

**MECHANICAL ENGINEERING
NORTH CAROLINA STATE UNIVERSITY**

Raleigh, NC
2005

APPROVED BY:

Advisory Committee Chair

BIOGRAPHY

Karalyn Folkert, born October 18, 1980, grew up in Zeeland, Michigan. She graduated from Zeeland High School in 1999. She attended Western Michigan University in Kalamazoo, MI where Kara became active in various engineering organizations including Tau Beta Pi in which she held the position of President. She also participated in research in the Tribology Laboratory under the direction of Dr. Philip Guichelaar and Dr. Molly Williams for two years. During her tenure at WMU, she also attained two internships during the summers at Consumers Energy Company and Armstrong Service, respectively. Following Kara's graduation with her Bachelor of Science in Engineering (Mechanical) from the Lee Honors College, she pursued her Masters in the fall of 2003 at North Carolina State University. Upon completion of her MSME in the summer of 2005, she'll begin work at Cummins Consolidated Diesel Company in Rocky Mount, NC.

ACKNOWLEDGEMENTS

I will always be grateful for the invaluable experience and trials that come with pursuing a Masters. There have been many people who have been influential throughout these last two years at NC State. I would personally like to thank a number of them.

- Dr. Thomas Dow, my advisor, for continuing to push me to perfection. His insatiable desire for detail and knowledge has been inspirational. Thank you for taking the time to explain anything and everything that I did not understand pertaining to research.
- Ken Garrard, who spent countless hours with me and Matlab. I will always be amazed by all that you know. Thank you for your patience when I know you've been extremely busy with other work.
- Alex Sohn, for showing me some of the ins and outs of machining. I appreciate your expertise that you shared with me on the ASG and the milling machine.
- Dr. Jeffrey Eischen and Dr. Ron Scattergood, my committee members, for your willingness to be a part of this research. Each of your classes have also taught me a lot.
- Brett Brocato, Nathan Buescher and Anthony Wong, for helping me out in the beginning stages of this research. You guys have been great!
- My fellow graduate students at the PEC: Karl, Witoon, Simon, Dave, Tim, Yanbo, Lucas, Rob and Nadim. I've thoroughly enjoyed the Friday lunches and comic relief!
- Lara Masters, for answering all my miscellaneous questions and taking care of my travel reservations and purchase orders.
- My roommates, Candice, Stephanie and Denise, for constant support and understanding throughout.

- Lauren, for praying for me and being the voice of encouragement every time I needed it. I will always appreciate your listening ear.
- To my parents, Al and Judi Folkert, thanks for always supporting me in all that I do. Thank you for all your love and encouragement. I could not ask for better parents. Love you both.
- Lastly, thanks be to my Lord and Savior (Isaiah 55:9)

This research was sponsored by BWXT Y-12, L.L.C.

TABLE OF CONTENTS

LIST OF FIGURES	VIII
LIST OF TABLES	XIII
1 INTRODUCTION.....	1
1.1 HARDWARE	1
1.1.1 <i>Rotary Contour Gage</i>	1
1.1.2 <i>Coordinate Measuring Machines (CMMs)</i>	2
1.1.3 <i>Probes</i>	6
1.1.3.1 Touch Trigger Probes.....	7
1.1.3.2 Scanning Probes.....	8
1.2 EXISTING TECHNIQUES TO REDUCE MEASUREMENT ERRORS.....	9
1.2.1 <i>Error Map</i>	9
1.2.2 <i>Calibrated Artifacts</i>	11
1.2.2.1 Gauge Block.....	12
1.2.2.2 Ring Gauge	12
1.2.2.3 Ball Bar.....	13
1.2.2.4 Hole Bar.....	14
1.2.2.5 Ball Plate and Hole Plate.....	15
1.2.2.6 Space Frame.....	16
1.2.2.7 Modular Freeform Gauge.....	17
1.2.2.8 Multi-Wave Standard.....	18
1.3 DESIGN OBJECTIVES.....	19
2 ARTIFACT DEVELOPMENT.....	20
2.1 RING GAUGE SHAPE	20
2.1.1 <i>Material</i>	21
2.2 RING GAUGE SURFACE FEATURES.....	21
2.3 DYNAMIC ANALYSIS THEORY	22
2.3.1 <i>Discrete Fourier Transform (DFT)</i>	23
2.3.2 <i>Single Frequency Sine Wave</i>	23
2.3.3 <i>Multiple Single Frequency Sine Waves</i>	24
2.3.4 <i>Concatenation of Waves</i>	25
2.3.5 <i>Swept Sine Wave</i>	27
2.3.5.1 Swept Sine Wave Excitation.....	29
3 ARTIFACT FABRICATION.....	34
3.1 ALUMINUM ARTIFACT	34

3.1.1	<i>Machining Ring Structure</i>	34
3.1.2	<i>Swept Sine Wave Machining Process Development</i>	38
3.1.2.1	Ring Analysis.....	38
3.1.2.2	FTS Analysis.....	39
3.1.3	<i>FTS Open Loop Control</i>	40
3.1.4	<i>Fabrication</i>	42
3.1.5	<i>Artifact Analysis</i>	44
3.1.5.1	Probe Calibration.....	44
3.1.5.2	Distortion of the Ring.....	47
3.1.5.3	Y-12 Measurements.....	48
3.2	CYLINDRICAL ARTIFACT.....	50
3.2.1	<i>Sources of Error</i>	52
3.2.1.1	Tool Clearance.....	52
3.2.1.2	Probe Tip Diameter.....	53
3.2.1.3	LVDT Calibration.....	55
3.2.1.4	Profilometer Measurement.....	56
3.3	FINAL ARTIFACT.....	58
3.3.1	<i>Closed Loop Control</i>	58
3.3.2	<i>Deconvolution</i>	61
3.3.3	<i>Ring Design Modifications</i>	66
3.3.4	<i>Ring Tolerances</i>	67
3.3.5	<i>Preparation for Fabrication</i>	69
3.3.6	<i>Fabrication</i>	73
3.3.6.1	Machining of each face.....	73
3.3.6.2	Preparation to machine ID and OD.....	78
3.3.6.3	Reference Command Generation.....	81
3.3.6.4	Machining the ID.....	82
3.3.6.5	Machining the OD.....	84
3.3.6.6	Angular Fiducial.....	86
3.3.7	<i>Measurement of Top and Bottom Surfaces of Ring 1</i>	87
3.3.8	<i>LVDT Measurement</i>	97
3.3.8.1	Calibration of LVDT.....	98
3.3.8.2	Swept Sine Wave Measurement.....	98
3.3.8.3	Comparison to the Desired Wave.....	108
3.3.8.4	Fiducial Measurement.....	112
3.3.8.5	Ridge Height Measurement.....	113
3.3.9	<i>Comparison of Ring 1 and Ring 2</i>	115
3.3.9.1	Surface Finish.....	115
3.3.9.2	Roundness.....	117
3.3.9.3	Swept Sine Wave Surface.....	119

4	APPLICATION OF ARTIFACT TO CMM CALIBRATION.....	125
4.1	UNCERTAINTY	125
4.2	DEFINITION OF MEASURAND	128
4.3	UNCERTAINTY OF CALIBRATED ARTIFACT	129
4.4	DEMONSTRATION OF USE	130
4.4.1	<i>Verification of LVDT Dynamics.....</i>	<i>134</i>
4.4.2	<i>Dynamic Implications</i>	<i>136</i>
5	CONCLUSIONS AND FUTURE WORK	137
6	REFERENCES	141
7	APPENDICES	144
7.1	APPENDIX A – EQUIPMENT SPECIFICATIONS	145
7.1.1	<i>dSPACE 1104 R&D Controller Board.....</i>	<i>145</i>
7.1.2	<i>Rotary Encoder</i>	<i>147</i>
7.1.3	<i>Capacitance Gage.....</i>	<i>150</i>
7.1.4	<i>Fast Tool Servo.....</i>	<i>154</i>
7.1.5	<i>Linear Variable Differential Transformer (LVDT).....</i>	<i>156</i>
7.1.6	<i>Torque Wrench.....</i>	<i>158</i>
7.2	APPENDIX B – LABVIEW CAPTURE OF TRANSFER FUNCTION	161
7.3	APPENDIX C – DTM SPINDLE SPEED CONTROL	165
7.4	APPENDIX D – MATLAB PROGRAMS	170
7.4.1	<i>Swept Sine Wave</i>	<i>170</i>
7.4.2	<i>Deconvolution</i>	<i>173</i>
7.4.3	<i>Fiducial.....</i>	<i>175</i>
7.4.4	<i>Averaging LVDT Data</i>	<i>178</i>
7.4.5	<i>Find Transfer Function.....</i>	<i>180</i>
7.5	APPENDIX E – DTM PROGRAMS	182
7.6	APPENDIX F – SIMULINK MODELS	184

LIST OF FIGURES

Figure 1-1. Rotary contour gage	2
Figure 1-2. Moving bridge CMM [1]	2
Figure 1-3. Fixed bridge CMM [1].....	3
Figure 1-4. Cantilever CMM [1].....	3
Figure 1-5. Gantry CMM [1]	4
Figure 1-6. Column CMM [1]	4
Figure 1-7. Moving bridge CMM at NCSU [9].....	5
Figure 1-8. Six degrees of freedom on a CMM axis [2].....	6
Figure 1-9. Touch trigger probe [8].....	7
Figure 1-10. Example of lobing in the X-Z plane with a 4mm diameter ball and 20mm stylus length [3].....	8
Figure 1-11. Proportional displacement probe [8].....	9
Figure 1-12. Gauge blocks.....	12
Figure 1-13. Ring gauge	13
Figure 1-14. Ball bars [13].....	14
Figure 1-15. Hole bar.....	14
Figure 1-16. Geostep™ 10 [14].....	15
Figure 1-17. Ball plate [11].....	16
Figure 1-18. Ceramic hole plate [15].....	16
Figure 1-19. Modular space frame [16].....	17
Figure 1-20. (a) Regular geometric shapes to simulate (b) a freeform object such as a turbine blade.....	18
Figure 1-21. R-type MWS around the circumference of a cylinder	18
Figure 1-22. Form profile of a MWS with corresponding amplitude spectrum [18]	19
Figure 2-1. Ring gauge drawing and 3-D image with dimensions	20
Figure 2-2. 6 Hz sine wave (left); FFT frequency response with peak magnitude of 4 and -90° phase at 6 Hz (right).....	24
Figure 2-3. Addition of multiple sine waves (left); FFT frequency spectrum (right).....	25
Figure 2-4. Concatenation of two single frequency sine waves (left); FFT frequency spectrum (right).....	25
Figure 2-5. Eight single frequency sine waves placed side by side (left); FFT frequency spectrum (right).....	27
Figure 2-6. Swept sine wave on the OD/ID of the ring	28
Figure 2-7. FFT of the first quadrant of the swept sine wave (5µm amplitude) on the ID....	30
Figure 2-8. FFT of swept sine wave with maximum amplitude of 5µm and 20,000 points..	31
Figure 2-9. Theoretical second-order dynamic system.....	32
Figure 2-10. Simulated swept sine wave measurement.....	33
Figure 3-1. Assembly of ring on mount.....	34

Figure 3-2. Setup for machining of the ring gauge with the FTS on the ID	37
Figure 3-3. First mode shape of natural frequency	38
Figure 3-4. Open loop characteristics of the FTS	40
Figure 3-5. Simulink model of FTS control.....	42
Figure 3-6. Cubic fit of PZT displacement	42
Figure 3-7. Schematic of Al ring cross section.....	43
Figure 3-8. Setup with FTS and ring gauge.....	44
Figure 3-9. Calibration data of LVDT with best-fit line.....	45
Figure 3-10. LVDT measurement of entire swept sine wave	46
Figure 3-11. Surface profile of ring gauge with bolts in place	47
Figure 3-12. Cross section of ring attachment to spacers	47
Figure 3-13. Surface profile of ring gauge with bolts removed.....	48
Figure 3-14. Ring gauge in a horizontal orientation on CMM (left) and scanning probe in contact with ring (right)	49
Figure 3-15. Measurement of the swept sine wave on the ID (left) and measurement of the roundness of the gauge (right)	49
Figure 3-16. Experimental setup to machine swept sine wave on OD of cylinder and the air-bearing LVDT used to measure the final shape.....	51
Figure 3-17. Cap gage reading of 2.5 μ m amplitude input (left); LVDT measurement of sine waves (right)	51
Figure 3-18. Swept sine wave output thru the HV amplifier as seen on an oscilloscope	52
Figure 3-19. Chip formation during machining with associated angles [23]	53
Figure 3-20. Probe compensation concept [20]	54
Figure 3-21. Top subplot is the expected measurement and bottom is actual LVDT measurement	55
Figure 3-22. Setup of LVDT calibration (left), and determination of calibration slope (right)	56
Figure 3-23. Profilometer measurement of swept sine wave.....	57
Figure 3-24. System characteristics of the FTS with larger view of phase from 1-600Hz....	58
Figure 3-25. Hysteresis loops for different amplitudes of motion for the PZTs in the FTS..	59
Figure 3-26. Various parameters for the PI gains of the closed loop controller.....	60
Figure 3-27. Comparison of closed and open loop system identifications up to 600Hz	61
Figure 3-28. Closed loop FTS transfer function up to 800Hz	62
Figure 3-29. FTS transfer function complex values and their conjugate.....	63
Figure 3-30. Frequency range of transfer function increased.....	64
Figure 3-31. Expanded section of adjusted input (dots) to demonstrate altered amplitude; time relates to spindle speed	65
Figure 3-32. Expanded section of adjusted input (dots) to show phase-lead and amplitude reduction of input signal	65
Figure 3-33. Comparison of control methods	66

Figure 3-34. New design of the ring gauge artifact	67
Figure 3-35. Drawing with tolerance specifications of ring gauge.....	68
Figure 3-36. Ring 1 after plating with Ni build-up at two counter bores	70
Figure 3-37. Adjustable reamer (left); valve seat cutter (right).....	71
Figure 3-38. Verification of plating thickness for Ring 1.....	72
Figure 3-39. Profilometer measurement of a chamfer on Ring 1	72
Figure 3-40. z-axis touch-off on the surface of the spacers.....	74
Figure 3-41. Setup to machine each ring face flat	75
Figure 3-42. Profilometer measurements of first machined face of Ring 1 before (top) and after (bottom) interrupted cut.....	77
Figure 3-43. Profilometer measurements of second machined face of Ring 1 before (top) and after (bottom) interrupted cut.....	78
Figure 3-44. Lever-type electronic gage capture of ring centering	79
Figure 3-45. Lever-type electronic gage measuring tilt of the FTS.....	80
Figure 3-46. Measurement of tool height	80
Figure 3-47. Measurement of the squareness of the tool to the ID.....	81
Figure 3-48. Cross section view of probe measurement of wave; left demonstrates shanking problem with stylus.....	83
Figure 3-49. Cap gage captures of the swept sine wave cut on the ID of Ring 1	84
Figure 3-50. Cap gage captures of the swept sine wave cut on the OD of Ring 1	85
Figure 3-51. Comparison of expected and actual fiducial machined on the surface	86
Figure 3-52. Definition of counter bore positions on the ring	87
Figure 3-53. Surface map of the ring near CB1 with chips at edge.....	87
Figure 3-54. Surface map of the ring near one of the through holes (Side 1)	88
Figure 3-55. Surface map of CB5 on Side 2 opposite through hole on Side 1	89
Figure 3-56. Surface map of through hole associated with CB2.....	89
Figure 3-57. Surface map of counter bore 2 with ring attached to spacers	90
Figure 3-58. Surface map of CB2 with ring taken off mount.....	91
Figure 3-59. Surface map of CB5 on Side 2.....	92
Figure 3-60. Surface map of CB6 on left and zoomed in on right.....	93
Figure 3-61. OD of the ring on Side 2 as measured by the NewView	93
Figure 3-62. ID of the ring on Side 1 as measured by the NewView	94
Figure 3-63. Surface finish near through hole of CB5 on Side 1	94
Figure 3-64. Profilometer measurement of surface finish on the ID of Ring 1	95
Figure 3-65. Profilometer measurement of surface finish on the OD of Ring 1	96
Figure 3-66. Set up for the LVDT measurement of the wave	97
Figure 3-67. Calibration of LVDT with determined conversion factor.....	98
Figure 3-68. Incremental swept sine wave measurement with the LVDT	99
Figure 3-69. Roundness of the ring on the OD.....	99
Figure 3-70. Concentricity between the flat and wave sections on the OD of Ring 1.....	100

Figure 3-71. Comparison of flat section of OD before and after fit was applied	101
Figure 3-72. Verification of wave with averaged data	102
Figure 3-73. All 12 measurements of the wave on the OD of Ring 1	102
Figure 3-74. Average of measurements along with wave deviation on the OD of Ring 1 ..	103
Figure 3-75. Roundness of the ring on the ID of Ring 1	105
Figure 3-76. Concentricity between the flat and wave sections on the ID	105
Figure 3-77. Comparison of flat section of ID before and after fit was applied.....	106
Figure 3-78. All 12 measurements of the wave on the ID of Ring 1	107
Figure 3-79. Average of measurements along with wave deviation on the ID of Ring 1 ...	107
Figure 3-80. Comparison of the desired wave to the actual wave on the OD of Ring 1	109
Figure 3-81. The measured wave subtracted from the compensated wave (bottom) with an expanded view at the highest frequency on the OD (top) of Ring 1.....	110
Figure 3-82. Comparison of the desired wave to the actual wave on the ID of Ring 1.....	111
Figure 3-83. The measured wave subtracted from the compensated wave (bottom) with an expanded view at the highest frequency on the ID (top) of Ring 1	112
Figure 3-84. LVDT measurement of fiducial on the OD of Ring 1	112
Figure 3-85. Illustration of ridge measurement	113
Figure 3-86. Determination of ridge height on the OD of Ring 1	114
Figure 3-87. Determination of ridge height on the ID of Ring 1	114
Figure 3-88. Profilometer measurement of surface finish on the ID of Ring 2.....	115
Figure 3-89. Profilometer measurement of surface finish on the OD of Ring 2	116
Figure 3-90. Roundness and concentricity of ID of Ring 2.....	117
Figure 3-91. Roundness and concentricity of OD of Ring 2	118
Figure 3-93. Comparison of roundness of both rings	118
Figure 3-94. Average of measurements along with wave deviation on the ID of Ring 2 ...	119
Figure 3-95. Comparison of the desired wave to the actual wave on the ID (Ring 2)	121
Figure 3-96. The measured wave subtracted from the compensated wave with an expanded view at the highest frequency on the ID on Ring 2.....	122
Figure 3-97. Average of measurements along with wave deviation on the OD of Ring 2..	123
Figure 3-98. Comparison of the desired wave to the actual wave on the OD (Ring 2).....	124
Figure 3-99. The measured wave subtracted from the compensated wave with an expanded view at the highest frequency on the OD on Ring 2.....	125
Figure 4-1. Transfer function of the LVDT on ID of Ring 2 at (a) 1RPM, (b) 2RPM, (c) 3RPM	132
Figure 4-2. Transfer function of the LVDT on OD of Ring 2 at (a) 1RPM, (b) 2RPM, (c) 3RPM	133
Figure 4-3. Measurement of the swept sine wave on Ring 2 with different speeds on the (a) OD and (b) ID.....	134
Figure 4-4. Setup to determine dynamics of LVDT	135
Figure 4-5. Transfer function of the LVDT	136

Figure 7-1. Side mounting of rotary encoder [25]	147
Figure 7-2. Schematic and specifications of rotary encoder [26]	147
Figure 7-3. TTL incremental signals [27].....	148
Figure 7-4. 15-pin, female Sub-D connectors located on the front of the controller panel [28].....	148
Figure 7-5. Construction of a capacitance gage probe [30]	151
Figure 7-6. Cap gage probe with dimensions	153
Figure 7-7. Cap gage calibration certificate.....	153
Figure 7-8. The fast tool servo without the tool shown	154
Figure 7-9. Cross section of the FTS with specifications	155
Figure 7-10. Coil assembly of a LVDT [29].....	156
Figure 7-11. LVDT output based on the position of the core [29]	157
Figure 7-12. Dual scale torque wrench from CDI	159
Figure 7-13. Dial torque wrench calibration certificate.....	159
Figure 7-14. Instructions on use from CDI Operation Manual.....	160
Figure 7-15. Pinout of the SCB-68 connector block.....	162
Figure 7-16. “System_ID_v2.vi” front panel.....	163
Figure 7-17. Simulink model of the closed loop controller with the LabView input.....	164
Figure 7-18. Sample of data saved by LabView	164
Figure 7-19. x-axis is commanded speed while y-axis is the actual speed.....	165
Figure 7-20. Motor open loop step response	167
Figure 7-21. Verification of modeled system	168
Figure 7-22. Step response of both systems	169
Figure 7-23. Speed control comparison after implementation.....	169

LIST OF TABLES

Table 3-1. Determination of feed rate.....	36
Table 3-2. Determination of minimum and maximum frequency during fabrication	39
Table 3-3. Individual chamfer depth measurements for Ring 1 (all values in inches).....	73
Table 3-4. Summary of interferometer surface measurements of Side 1	88
Table 3-5. Summary of interferometer surface measurements of Side 2	89
Table 3-6. Side 1 surface measurements with ring attached to disk and spacers	90
Table 3-7. Side 1 surface measurements with ring taken off mount	91
Table 3-8. Side 2 surface measurements with ring taken off mount	92
Table 3-9. Zoomed in sections on Side 2; 2 counter bores, 2 small holes.....	93
Table 3-10. Summary of statistics for all OD measurements (units μm) based on the individual errors from the average measurement value.....	104
Table 3-11. Summary of statistics for all ID measurements (units μm).....	108
Table 3-12. Summary of statistics for all ID measurements on Ring 2 (units μm).....	120
Table 3-13. Summary of statistics for all OD measurements on Ring 2 (units μm)	123

1 INTRODUCTION

The Y-12 National Security Complex (Y-12) manufactures precision workpieces for the government and private companies. Part acceptance is based on dimensional inspection by comparison to the tolerance specifications of the part drawing. In the past, Y-12 used specialized gages such as a rotary contour gage to measure a round part. Coordinate Measuring Machines (CMMs) are preferred because of their flexibility; yet this flexibility may make estimating uncertainty more difficult with additional input parameters defining the measurand. The goal of this project is to design and fabricate an artifact that can accurately predict the measurement uncertainty for a task, such as scanning around a workpiece, by determining a transfer function between the measurement and the artifact.

1.1 HARDWARE

Two of the dominant dimensional inspection machines are rotary contour gages and CMMs. The rotary contour gage has fewer degrees of freedom than the CMM making it less flexible. A description of each machine follows.

1.1.1 Rotary Contour Gage

A rotary contour gage consists of a rotary table and an LVDT on a tilting stage. The part is placed on the table where it is inspected by the LVDT probe that can move in the Y and Z directions. The inspection of the part can be accomplished in one of two ways. One approach is to place the probe at a particular location on the part and then rotate the table to make the latitude measurement. The other method keeps the table stationary

while moving the probe to make a longitudinal measurement. Some machines may have dual opposing probes that are able to measure the ID, OD and thickness at the same time.

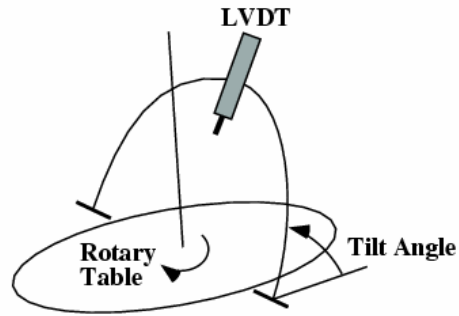


Figure 1-1. Rotary contour gage

1.1.2 Coordinate Measuring Machines (CMMs)

A CMM typically consists of three carriages that are mutually orthogonal. Each machine can have a different configuration. The most common configurations include moving bridge, fixed bridge, cantilever, horizontal arm, gantry, and column [1]. Figure 1-2 is an example of a moving bridge CMM where the three axes are able to move while the table remains fixed. The moving bridge is one of the more typical designs [1].

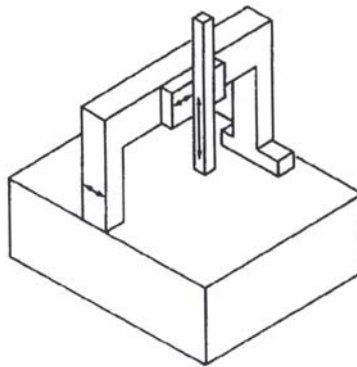


Figure 1-2. Moving bridge CMM [1]

Conversely, a fixed bridge CMM (Figure 1-3) allows the table to move on the base while the ram (z-axis) moves vertically on a cross slide, creating less moving mass than the

moving bridge design. However, the weight of the granite table may create bending of the table [1].

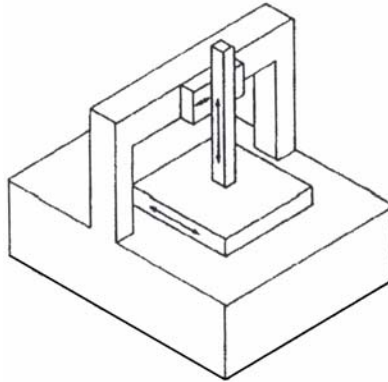


Figure 1-3. Fixed bridge CMM [1]

The cantilever type CMM (Figure 1-4) uses a cantilever beam that moves left to right across the table. The z-axis is mounted on a carriage that moves in and out on the cantilever beam as the cantilever moves left to right over the table [1].

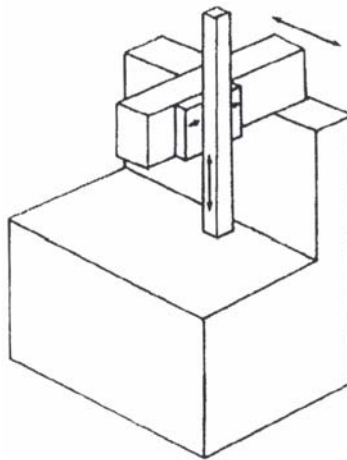


Figure 1-4. Cantilever CMM [1]

The horizontal arm CMM is typically used in the automotive industry and may or may not include moving tables. The only way to access both sides of a part with this machine is to use a rotary table [1].

The gantry CMM (Figure 1-5) is useful for large parts because of the two, large fixed beams that the coordinate axes rest on. One carriage moves back and forth on the beams while another axis, attached to the first carriage, moves from side to side. The ram moves up and down the same as the previously described CMMs with the exception of the horizontal arm CMM [1].

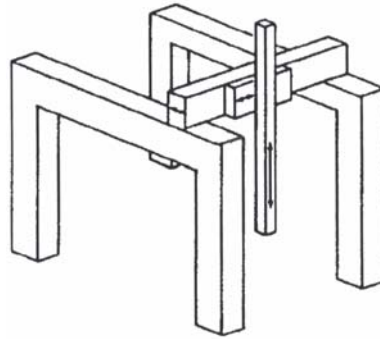


Figure 1-5. Gantry CMM [1]

The column CMM (Figure 1-6) consists of a table that moves in X and Y and a fixed column. The ram is attached to the column and moves vertically. A camera is another component that can be incorporated into this design [1].

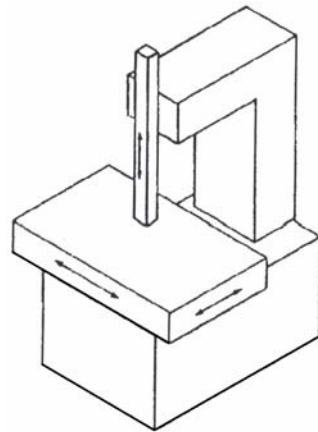


Figure 1-6. Column CMM [1]

The three orthogonal axes give the CMM its flexibility. Depending on the measurement application, one configuration may be better suited than another. However, all

configurations exhibit inherent geometry error that must be accounted for during static calibration. The configuration will also affect the dynamics of the machine so it is important that the designed artifact can be used on any CMM.

Displacement transducers are used to find the displacement (coordinate) of each axis of the CMM. The displacement transducers may be Moiré scales, interferometric gratings, or laser interferometers. Moiré scales, the most common, consist of fringe patterns that are made up of sine and cosine waves that are of equal amplitude but are out of phase [1]. The placement of the transducers allows a spatial reference point on the probe to be used to determine the displacement along a coordinate path in the working volume of the CMM.

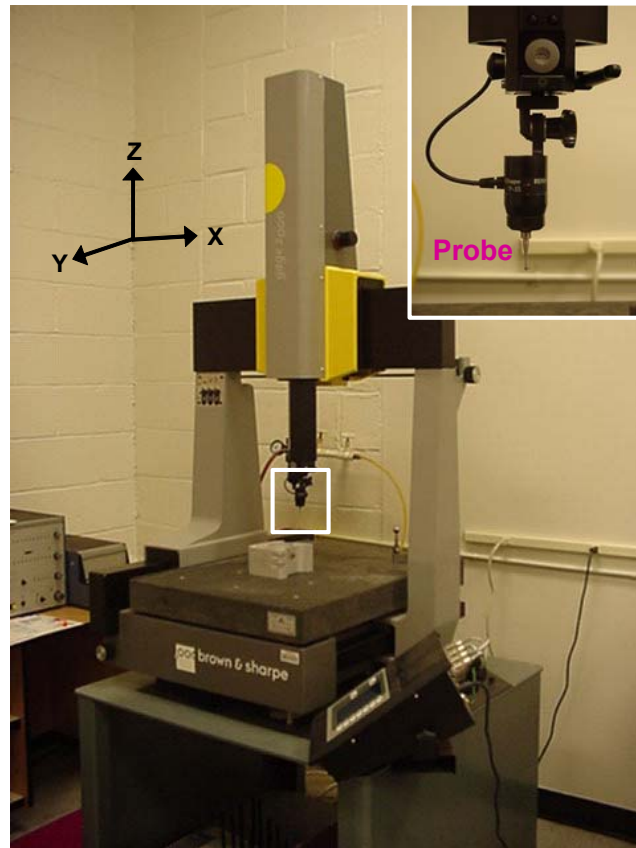


Figure 1-7. Moving bridge CMM at NCSU [9]

On each axis of the CMM, there are six degrees of freedom. These can be segregated into three translational components (linear positioning and mutually orthogonal straightness) and three rotational components (roll, pitch, and yaw). Furthermore, the axis pairs (XY, YZ, XZ) form three out-of-squareness elements. Three axes with six degrees of freedom plus three out-of-squareness components equal 21 geometric (parametric, volumetric) errors associated with the CMM [2]. Figure 1-8 demonstrates the six degrees of freedom on an axis.

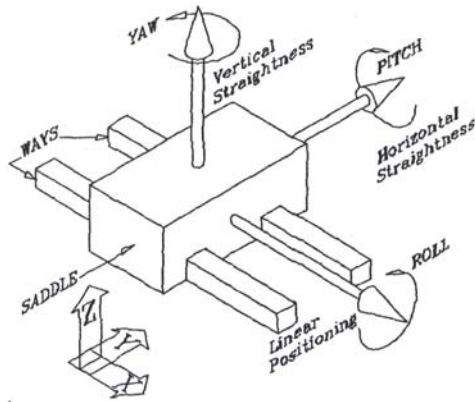


Figure 1-8. Six degrees of freedom on a CMM axis [2]

1.1.3 Probes

Another component of the CMM is a probe. In Figure 1-7, the probe is attached to the end of the z-axis carriage. As the carriages move, the probe may come into contact with the surface of a workpiece. When a particular force or displacement of the probe has been reached, the CMM records the coordinate. The probe is an integral part of the CMM but increases the error and uncertainty of the CMM. A probe can be used in one of two modes: point to point or scanning.

1.1.3.1 Touch Trigger Probes

A touch-trigger is one type of a point to point probe. It examines the surface of a part by contacting a point on the surface, where it takes a reading, and then moves out to engage another point to inspect on the workpiece. The axes on the CMM can be moved manually or programmed to touch the surface in a pre-determined pattern. For the probe in Figure 1-9, the armature of the probe consists of three arms that rest on three sets of two balls or cylinders located 120° apart [3]. The stylus of the probe deflects when it comes into contact with the workpiece and causes one or two of the arms to lift out of its neutral position. The electronic interface notices the change and triggers the CMM to take a reading [3]. After a number of readings, the CMM can compare the measurement data to basic geometric shapes [4].

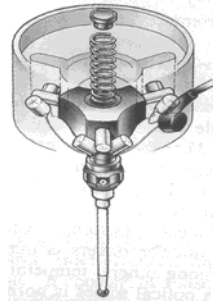


Figure 1-9. Touch trigger probe [8]

The accuracy of the touch-trigger probe depends on the inherent errors of the probe. Pre-travel variations are the main source of its error. A pre-travel variation is defined as the “distance traveled by a probe between the actual touching of a surface and the trigger event [5].” The probe stylus will deflect by a different amount before each trigger event, creating lobing errors. The kinematic arrangement of the arms permits different probing forces to produce a signal, depending on the direction of approach [3,5]. A map of the displacement of the lobing errors can be seen in Figure 1-10. Lobing errors are

dependent on the reference plane (X-Y, Y-Z, X-Z) and the orientation and length of the stylus. Lobing will produce a variation in the out-of-roundness measurement along with repeatability errors [3].

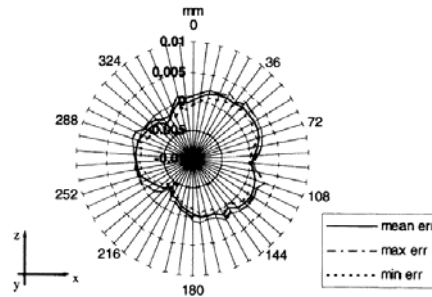


Figure 1-10. Example of lobing in the X-Z plane with a 4mm diameter ball and 20mm stylus length [3]

1.1.3.2 Scanning Probes

A scanning probe remains in continuous contact with the workpiece as the measurement is performed [4]. One type of continuous analog scanning probes is proportional displacement [6]. With the proportional displacement probe, it is not necessary to have a pre-defined path as the displacement at each coordinate is captured. The SCEPTRE™ proportional displacement probe [7] is mechanically configured with three cubes that are formed with two right-angle brackets; the brackets are held with spring steel wires. Two infrared LEDs are affixed to the fixed bracket; two photodiodes are attached to each moveable bracket. As the sides of the cube move, the corresponding photodiodes detect the energy emitted from the LEDs. The two photodiodes on each cube are electronically connected in a differential mode to detect the deflection of the probe.



Figure 1-11. Proportional displacement probe [8]

There are two methods for using the scanning probe to obtain measurements. The probe can provide feedback to the CMM to maintain a constant force on the workpiece, which requires no prior knowledge of the shape of the surface. If the shape was known, the probe could operate independently as the CMM re-traces the fabrication tool path and make a faster measurement because the path is pre-defined [6]. The accuracy of the measurement depends on the linearity and the dynamics of the probe as it responds to changes in the surface [4]. The increased number of measurement readings using a scanning probe as compared to the point to point method also improves the quality of the measurement with respect to repeatability and uncertainty.

1.2 EXISTING TECHNIQUES TO REDUCE MEASUREMENT ERRORS

1.2.1 Error Map

There is an important need to quantify the capability of measuring machines to characterize the dimensional features of 3-D workpieces. For a given measurement task, different machines and measurement procedures will produce different results depending on the shape, weight and surface features of the part. Over the years, significant effort has been expended to find methods to reduce errors in a measuring machine [9].

Typically, errors are defined statically due the geometry of the CMM. The working volume is divided into regions and the position errors in each region are defined in the x, y and z directions. This error information can be put into look-up tables on the machine controller and the actual part dimensions can be determined based on compensating the machine measurements for the errors in position from the error map. The uncertainty, discussed in further detail in Section 4.1, in the measurement result will be comprised of the uncertainty of the correction factor applied to the measurement and the repeatability of that error for a specific machine position. Error mapping the entire working volume of the CMM provides one solution for calibration by correcting the slide position based on the position of the probe [9].

Error mapping of the CMM highlights the parametric errors of the machine but does not consider the dynamic errors during a measurement. Sharp features on a part will affect the resulting measurement error due to the corresponding complexity of the CMM motion which may require a change in speed and accelerations of each axis [10]. Changing surface features will increase the movement of the axes which affects the speed of the measurement. This may cause the CMM to exhibit more error at a particular feature, depending on the size of the feature and speed of the measurement as they relate to the CMM's dynamics. Accordingly, higher measurement speeds will result in higher accelerations when measuring anything other than a flat surface. The changing accelerations will magnify the static geometric errors; since these errors are dependant on carriage positions, the acceleration of one carriage will vary the moment applied to

another carriage [10]. One way to estimate dynamic errors is to use additional sensors attached to each carriage of the CMM and to construct a kinematic model to estimate probe position [10]. However, this method only demonstrates improved measurement accuracy with single axis motion. Instead of modeling the dynamic errors of the machine, an artifact may be designed to determine the actual dynamic characteristics of the machine.

1.2.2 Calibrated Artifacts

Since the shape of a part will influence the measurement error of that part, a standard of the same design measured prior to the part of interest will indicate where the greatest errors of the CMM measurement will occur and a correction factor may be applied. To address the measurement-specific errors, the artifact should be the approximate size and weight of a typical workpiece. Therefore, if boxes are to be measured, then a box of roughly the same size, shape and weight of the box to be measured should be calibrated. The artifact box or series of artifact boxes must exhibit the typical errors of the boxes to be measured to validate the machine capability relative to those types of errors. However, since a task-specific standard is not available for all manufactured parts, features need to be designed into an artifact to test the dynamic limits of the CMM to allow its characteristics to be defined. These features may simulate various conditions that the probe may encounter on a part. The shape of the artifact can be used to determine the static characteristics of the CMM. Some other major considerations for an artifact are ease of use, transportability, stability, time needed for calibration and ability to diagnose the error [9].

Throughout the years, there have been a number of artifacts [2,11-17] developed to evaluate the performance of a coordinate measuring machine and/or to assist in its calibration. The artifacts may be used for a specific application or for a more generalized purpose. Artifacts may also be classified by the methods in which they are used to assess the accuracy of a CMM. Those methods include kinematic reference standard technique, parametric calibration technique, and transfer standard technique [16].

1.2.2.1 Gauge Block

One of the most straightforward methods to test CMMs is by use of a gauge block. A gauge block is a piece of metal of calibrated length. It is measured in various orientations and positions on the working volume of the CMM. A variety of gauge blocks can be used as length transfer standards [12]. The length measurement of a gauge block can be directly related to the length measurement of a part.

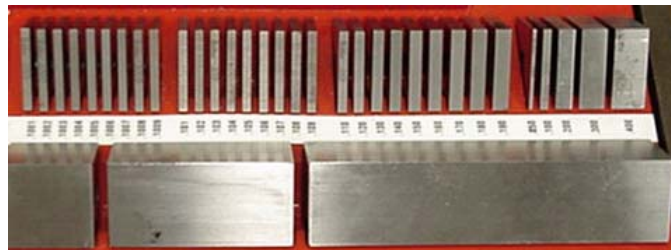


Figure 1-12. Gauge blocks

1.2.2.2 Ring Gauge

A ring gauge is a circular artifact with calibrated diameter and circularity that is used to tell how well diameter and circularity can be measured by a CMM. It should be measured in at least two positions in space along with various stylus configurations due to the dissimilar errors along the working volume of the CMM and lobing characteristics of the probe. Two of the positions in space may be in the horizontal and vertical orientations. For accurate verification of the CMM, it is suggested that 30 points be

probed or scanned. The probed data is compared with the calibration data of the ring gauge. The lobing error is based on the geometry data comparison, and machine geometric errors, such as scale and orthogonality errors, are determined from the error pattern of circular error of the gauge [12]. The measurement of a ring gauge is appropriate for the day to day survey of CMM performance.

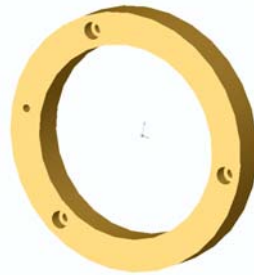


Figure 1-13. Ring gauge

1.2.2.3 Ball Bar

A ball bar consists of a rigid bar with a sphere at each end. Multiple types of ball bars exist today. They can be free-standing or have fixed magnetic sockets. The length between the centers of each sphere remains constant. The free-standing ball bar is placed on a gauge stand in a number of orientations in the working volume of the CMM. Each ball is probed and the difference in the length measurement between ball centers is compared to the calibrated distance. The operator should measure along edges, in-plane diagonals and cross-diagonals in the working volume to assess deviations from the geometrical structure. The magnetic ball bar includes a magnetic socket fixed to the CMM table while the other magnetic socket takes the place of the probe. The ball bar is kinematically supported in the sockets. The CMM can be moved to different positions to take the length measurements. The deviation to actual length contributes to the

development of an error map for the CMM; the volumetric machine errors are determined using this technique without finding the probe errors [12].



Figure 1-14. Ball bars [13]

1.2.2.4 Hole Bar

The hole bar is approximately 540mm in length with an I-beam cross section. As seen in Figure 1-15, the bar includes 11 holes along the length. These holes have a diameter of 13mm with a uniform distance between any two hole centers of 50 mm. The artifact can be used to determine the 21 parametric errors of the CMM. The artifact is oriented and mounted in 17 different positions to evaluate the performance. The positions cover all the parametric errors of a moving bridge CMM. The 17 sets of measurement data are compared with the calibrated artifact database to calculate the errors. The location of the hole centers are used in the transfer method in the validation of the CMM [2].

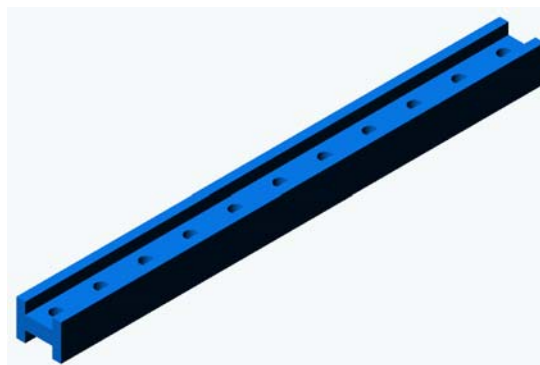


Figure 1-15. Hole bar

A variation in the basic hole bar involves mounting spheres in the center of each hole to transform the hole bar from a two-dimensional artifact to one that is three-dimensional. The Geostep™ 10, Figure 1-16, has a length of 850mm, a width of 101.6mm, and a thickness of 38.1mm. The ten, 19mm diameter spheres are mounted along the centerline of the beam. Center to center distance between the spheres is approximately 85mm. The center to center dimensions are varied to separate the systematic errors from the step standard. The three-dimensionality of the spheres negates the possibility of alignment or cosine errors of the artifact or positioning on the CMM because the origin of a sphere is characterized by its radius as an infinitesimal value in three-dimensional space [14]. The spheres are treated as single points rather than 3D objects.

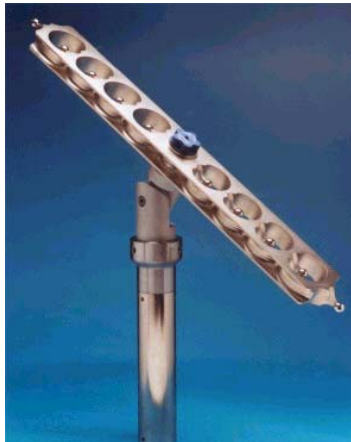


Figure 1-16. Geostep™ 10 [14]

1.2.2.5 Ball Plate and Hole Plate

The ball plate is comprised of a square plate with ceramic or stainless steel spheres arranged in space. The balls may be resting on the surface of the plate [11] or positioned at various heights. Four points on each sphere need to be probed to determine the center of the ball. If bending of the plate occurs, due to thermal expansion or other external

forces, the center dimension is susceptible to change [15]. The ball plate is predominantly used for day-to-day verification of the CMM parametric errors.

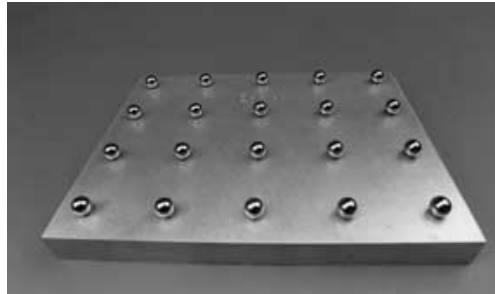


Figure 1-17. Ball plate [11]

The hole plate is very similar to the ball plate. Instead of balls configured in space, precision-machined holes are configured on the plate at qualified distances. Each hole has three points probed to determine the center. Bending of the plate does not have much effect on the center dimensions because bending would occur along the same plane as the centers. The hole plate is used for the parametric error calibration of the CMM [15].

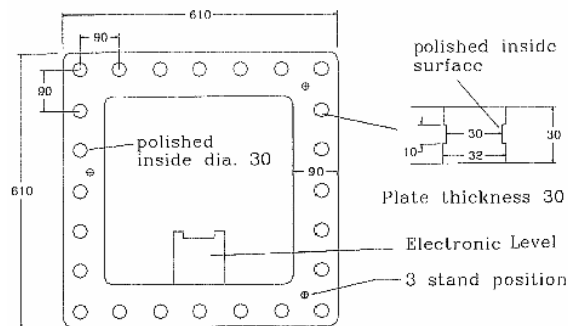


Figure 1-18. Ceramic hole plate [15]

1.2.2.6 Space Frame

The modular space frame includes a triangular plate along with three magnetic ball links attached to a sphere at the apex. The links are made of carbon reinforced plastic for its low coefficient of expansion and high stiffness-to-weight ratio [12,16]. It is important that the spheres resist corrosion and be accurate in shape and size. With the space frame, it is only necessary to calibrate the magnetic ball links and the plate before use with a

CMM [16]. The main function of the space frame is to indicate error tendencies of the machine and where adjustments are needed without representing a large amount of detail of machine errors as a whole [12]. The space frame is moved in a well-defined sequence within the working volume of the CMM. Each individual measurement is compared to the frame calibration data. By using the differences of the means and standard deviations as statistical parameters, the location of specific errors may be determined [12].

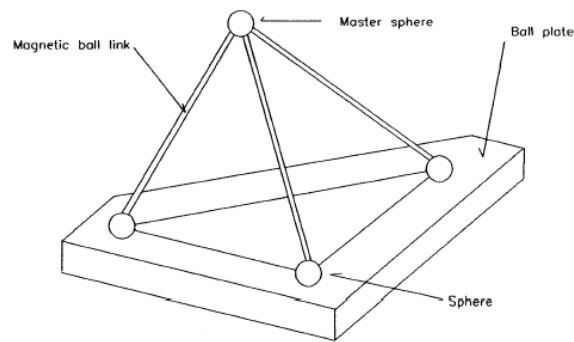


Figure 1-19. Modular space frame [16]

1.2.2.7 Modular Freeform Gauge

The modular freeform gauge is intended for the task-specific measurement of complex parts such as turbine blades. A freeform object is non-rotationally symmetric about any axis. This artifact models an object by combining regular geometric shapes. For a turbine blade, two cylinders of different diameters are chosen. Each shape is calibrated separately to reduce the calibration uncertainty. For measurement, the calibrated shapes are placed on the CMM, and their relative positions are determined. The assembly is modeled in CAD with the relative position points from the measurement. The experimental uncertainty can be established and used with the calibration data to ascertain the uncertainty of the freeform measurement. This artifact is not useful with

objects that have varying shapes because the shape must be able to be approximated by calibrated artifacts. This artifact is also not useful for concave surfaces [17].

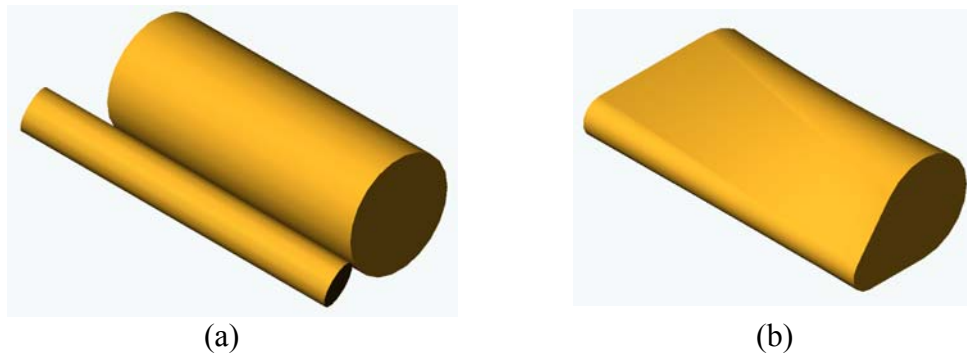


Figure 1-20. (a) Regular geometric shapes to simulate (b) a freeform object such as a turbine blade

1.2.2.8 Multi-Wave Standard

The Multi-Wave Standard (MWS) consists of several sinusoidal frequencies added together. The R-type (or roundness) form of the MWS places the waveform around the circumference of a cylinder, either on the outside or the inside. If the R-type MWS is machined on the inside, it can be used as an inner surface calibration standard. The other form is the S-type (or straightness) MWS. In this case, the waveform is machined along straight lines of the cylinder. This waveform may also be machined onto a flat surface and be used for calibration with roughness measurement instruments [18]. Figure 1-21 demonstrates a R-type MWS on the outer surface of a cylinder.



Figure 1-21. R-type MWS around the circumference of a cylinder

A Fourier analysis of the waveform produces an amplitude spectrum with lines at each single frequency of the wave; no other signal is present within the amplitude spectrum. This makes it insensitive to small local variations or damages. Errors in the machine will be represented by random peaks outside of the intended wave frequencies. Measurements of a MWS may give three indications about the performance of the measuring instrument. These include the overall sensitivity calibration, the spectral distortion of the profile, and the influence of filtering [18]. Figure 1-22 displays the form profile with its corresponding amplitude spectrum.

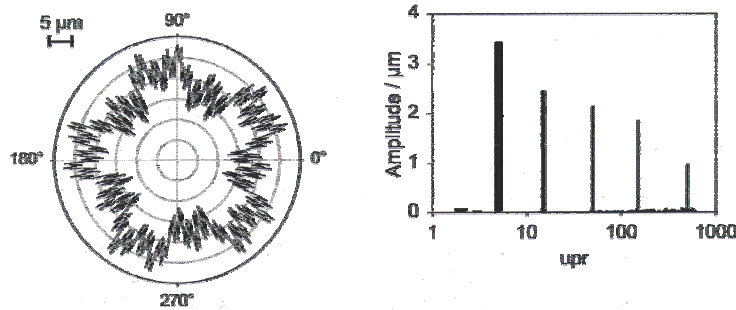


Figure 1-22. Form profile of a MWS with corresponding amplitude spectrum [18]

1.3 DESIGN OBJECTIVES

There are a number of objectives in the design of an artifact. They are as follows:

- 1) The artifact should be a standard shape (or several standard shapes) that can be measured on multiple machines to determine a transfer function between the artifact and the measurement.
- 2) Any spatial features on the artifact must permit probe radii of 0.25mm to 0.5mm to fit.
- 3) The artifact surface must be sufficiently robust that it is not damaged when used with various CMM probes, in either scanning or point-to-point inspection modes; probe forces may reach 2.5N.

2 ARTIFACT DEVELOPMENT

After considering the artifact standards discussed in Section 1.2.2, a ring gauge was chosen for further development. The overall attributes of the ring gauge (outside diameter (OD), inside diameter (ID), and wall thickness) can be used to exercise multiple axes of a CMM. In addition, small features can be added to the ID and OD to assess the capability of the machine to deal with small temporal and spatial variations in surface features. The ring gauge can also be measured in different orientations and positions on the CMM to cover the entire working volume.

2.1 RING GAUGE SHAPE

The ring's OD will measure 8" (203.2mm) with an ID of 6" (152.4mm) and an overall thickness of 1" (25.4mm). The dimensions are the approximate size of typical parts manufactured by the sponsor. The OD will have a groove that acts as a reference surface with the features being placed onto the ID. A small through hole has been designed into the ring that will provide a reference for angular position during a measurement. Figure 2-1 illustrates the dimensions and features of the ring.

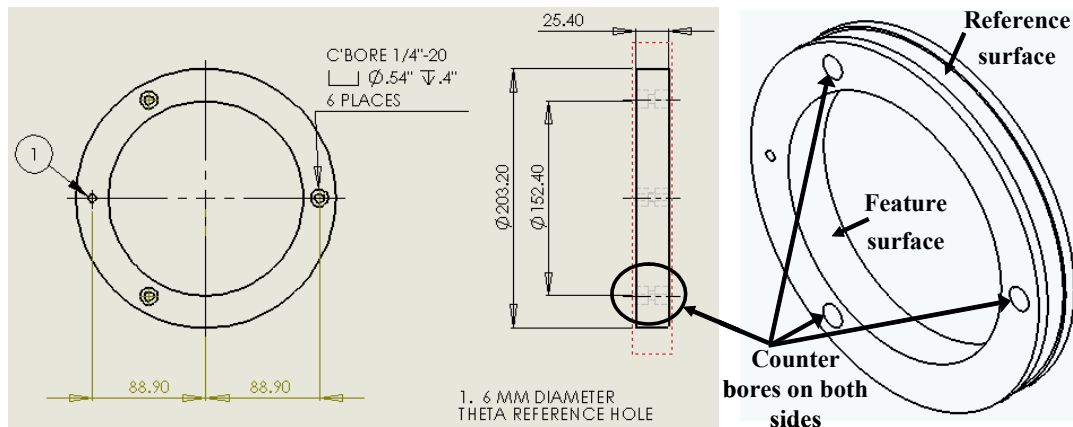


Figure 2-1. Ring gauge drawing and 3-D image with dimensions

2.1.1 Material

The material chosen for the trial fabrication of the ring gauge was Aluminum 6061-T6 because it is easy to machine. One of the attributes of Al 6061 is its high coefficient of thermal expansion ($23.6\mu\text{m}/\text{m}\cdot^{\circ}\text{C}$ or $13.1\mu\text{in}/\text{in}\cdot^{\circ}\text{F}$). The size of the part may change a significant amount depending on the temperature of its environment. For calibration purposes, it is important that the artifact not fluctuate in size. Thus, the material for the final artifact is 17-4PH stainless steel which was heat treated for maximum dimensional stability. Its coefficient of thermal expansion is $10.8\mu\text{m}/\text{m}\cdot^{\circ}\text{C}$ or $6\mu\text{in}/\text{in}\cdot^{\circ}\text{F}$ or roughly half that of the aluminum. Stainless steel cannot be machined with a diamond tool due to the amount of damage possible to the tool. For this reason, the ring is plated with electroless nickel which exhibits a non-ferrous characteristic, making diamond tool machining possible. The plating also adds to the microhardness of the stainless steel (44 Rockwell C, 430 Vickers); the actual quantity (500-700 Vickers) is dependant on the phosphorus content of the plating.

2.2 RING GAUGE SURFACE FEATURES

The small features on the surface should create a range of frequencies for evaluation of the CMM performance in the dynamic environment. There are a number of possibilities for types of features. Some of those include:

- A single frequency sine wave around the entire ring
- Addition of multiple single frequency sine waves
- Concatenation of single frequency sine waves
- A swept sine wave with varying frequencies

The analysis of such features will be discussed in the following section.

2.3 DYNAMIC ANALYSIS THEORY

The candidate surface features listed in the last section can be used to study the dynamic performance of the CMM. Each type of wave has features in the shape of a wave or combination of waves. If a measurement of a feature is made as a function of time, the apparent shape can be determined. However, it is difficult to quantify the amount of error when compared to the true wave shape. Possible sources of error may be from a shift in the actual location of the wave with the correct magnitude or the measured magnitude may be incorrect. Either scenario will add to the overall error of the CMM, but the correction factors for each error may be different. Thus, it is important to separate the major source of error: magnitude or phase. A possible solution is to convert the time domain measurement to the frequency domain.

The desired feature is to be measured using different measurement speeds to expand the frequency range for dynamic analysis. One approach to analyzing the wave is to apply a Fast Fourier Transform (FFT) to the data set. By knowing the measurement speed, the sampling rate, and the spatial wavelength of the wave, the measurement can be placed in the frequency domain; the FFT converts the time domain measurement into the frequency domain. An FFT may be used to determine other frequencies present in a data set that would normally not be apparent in the time sampled measurement. Due to the complexity of Fourier transforms, it may be useful to first understand the theory with the frequency domain response of each proposed feature.

2.3.1 Discrete Fourier Transform (DFT)

If a system is defined as $f(t)$ in the time domain and δt is the sampled time with N samples, the DFT converts the time samples to N frequency samples. It creates a complex number with the real value as a cosine component and the imaginary value as a sine component [19]. Equation 1 represents the DFT operation.

$$F(k) = \sum_{t=0}^{N-1} f(t) \times \left(\cos\left(\frac{2\pi kt}{N}\right) - i \sin\left(\frac{2\pi kt}{N}\right) \right) \quad (1)$$

where: $k = 1..N$

The maximum frequency sampled is equivalent to the reciprocal of the sampling time, δt , while the minimum frequency sampled is the reciprocal of the total time of the sample. The frequency resolution is the maximum frequency divided by the number of samples. The DFT is typically calculated using an FFT algorithm to speed up the calculation because the FFT eliminates the redundant calculations present in the DFT [19]. The results of the calculation are used to create a frequency spectrum with magnitude and phase components.

2.3.2 Single Frequency Sine Wave

If an FFT is performed on a 6Hz sine wave with an amplitude of 4, the frequency spectrum will indicate the only non-zero magnitude at 6Hz with a value of 4. Since the sine wave signal is composed of the real (cosine) component only, the phase lags by 90° ; thus, the phase is equal to -90° at 6Hz. Figure 2-2 demonstrates these attributes.

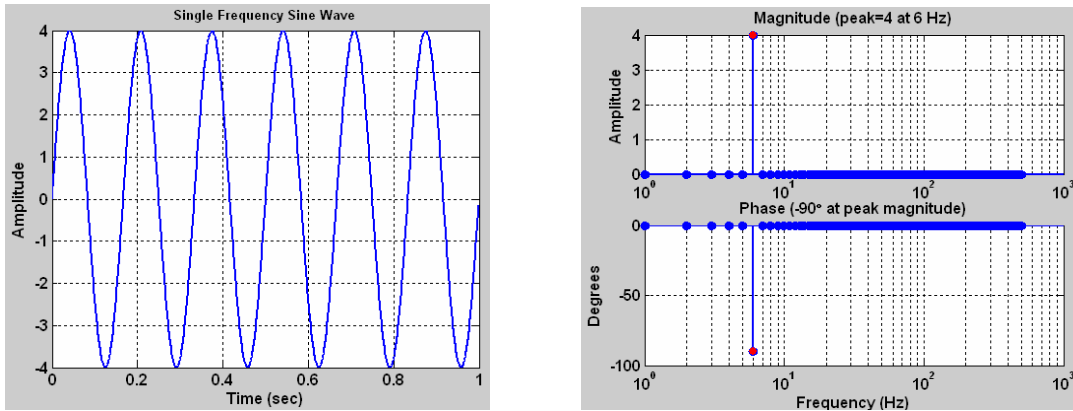


Figure 2-2. 6 Hz sine wave (left); FFT frequency response with peak magnitude of 4 and -90° phase at 6 Hz (right)

If any phase was added to the sine wave in Figure 2-2, the additional phase would be apparent on the phase plot. A phase shift of 45° to the right (delaying the sine wave in time from the reference cosine wave) increases the phase value to -135° .

A single wavelength sine wave measured with multiple speeds would create the range of frequencies necessary to determine the dynamic characteristics of the CMM. However, a considerable number of measurements would be required to produce a valid transfer function.

2.3.3 Multiple Single Frequency Sine Waves

Consider a signal with 3 separate single frequency sine waves added together (Figure 2-3). The frequency spectrum indicates that the first sine wave is 1Hz with an amplitude of 2, phase shifted to the left by 57.3° to produce a value of -32.7° . The second wave is 4Hz, has an amplitude of 1.5 and has also been shifted to the left to give a phase value of -32.7° . The final wave is 8Hz with an amplitude of 1 and -32.7° of phase.

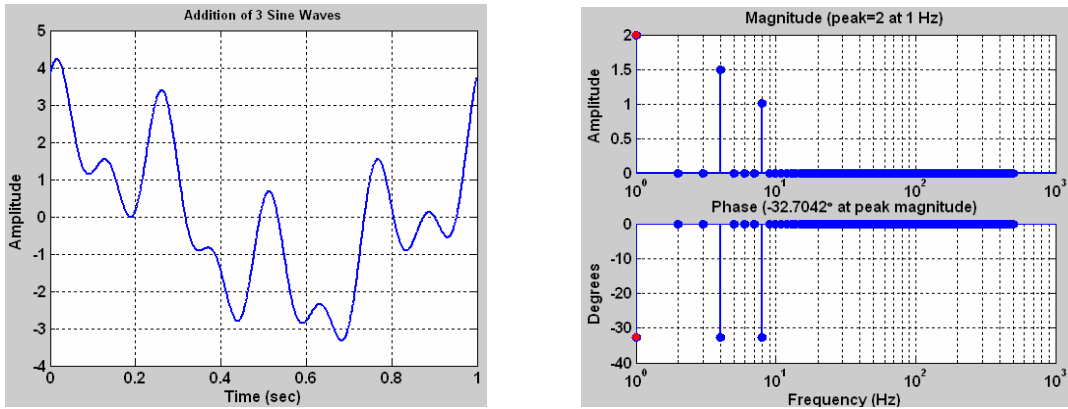


Figure 2-3. Addition of multiple sine waves (left); FFT frequency spectrum (right)

The addition of multiple single frequency sine waves is the concept behind the multi-wave standard in Section 1.2.2.8. Multiple waves increase the amount of frequencies for evaluation but it still requires a number of measurements to calculate a conclusive transfer function. The time domain signal is also difficult to interpret in terms of shape.

2.3.4 Concatenation of Waves

The placement of single frequency sine waves next to each other (concatenation) creates a different outcome than the addition of multiple single frequency sine waves. If a 4Hz sine wave is concatenated with a 5Hz sine wave, the frequency spectrum, in Figure 2-4, shows a decrease in amplitude and an increase in phase.

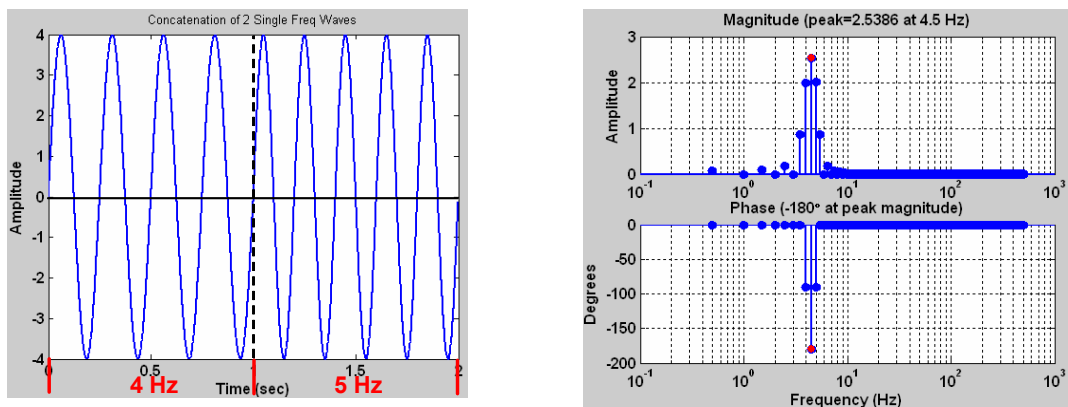


Figure 2-4. Concatenation of two single frequency sine waves (left); FFT frequency spectrum (right)

The original amplitude of both waves in Figure 2-4 was 4. However, after the FFT calculation, the peak magnitude of the sum is equal to approximately 2.5 at 4.5Hz. The concatenation of waves creates a time delay in each individual wave. For the 4Hz wave, half of the total time is spent at an amplitude of 4 while the other half has an amplitude of 0. The same is true for the 5Hz wave except that it starts with an amplitude of 0 and exhibits a second half amplitude of 4. Thus the mean amplitude of each wave is 2. Between 4 and 5Hz, the wave is transitioning which creates a different amplitude and alters the value of the peak magnitude found at 4.5Hz (the average frequency of both waves). The phase at 4.5Hz is also -180° because of an unwrapping¹ function in the FFT algorithm that adds the individual phase values of each wave.

A more complicated feature consists of concatenating several increasing single frequency sine waves, reflecting the assembled waves so that the frequencies decrease and then inverting them to begin where the original waves ended. This arrangement would create a continuous wave during fabrication; the starting and ending points connect. The concatenated wave plot in Figure 2-5 is in the time domain but shows where the division of the different frequency waves occur. The plot begins with a 4Hz sine wave; a 5Hz wave starts where the 4Hz wave ends, then a 6Hz wave is added to the end of the 5Hz wave and a 7Hz wave begins at the end of the 6Hz wave. The second half of the plot is the first 4 waves copied and rotated 180° . Each frequency section encompasses an equal amount of time. Although the amplitude of each wave is 4, the peak magnitude is smaller for the same reason as was previously described with the two single frequency

¹ Unwrapping refers to a summation of previous values to find the current value

concatenated waves. The phase alternates between -90° , 0° and 90° for the frequency range because each frequency repeats but is shifted 90° . For frequencies greater than 7Hz, the phase is an artifact of the FFT algorithm.

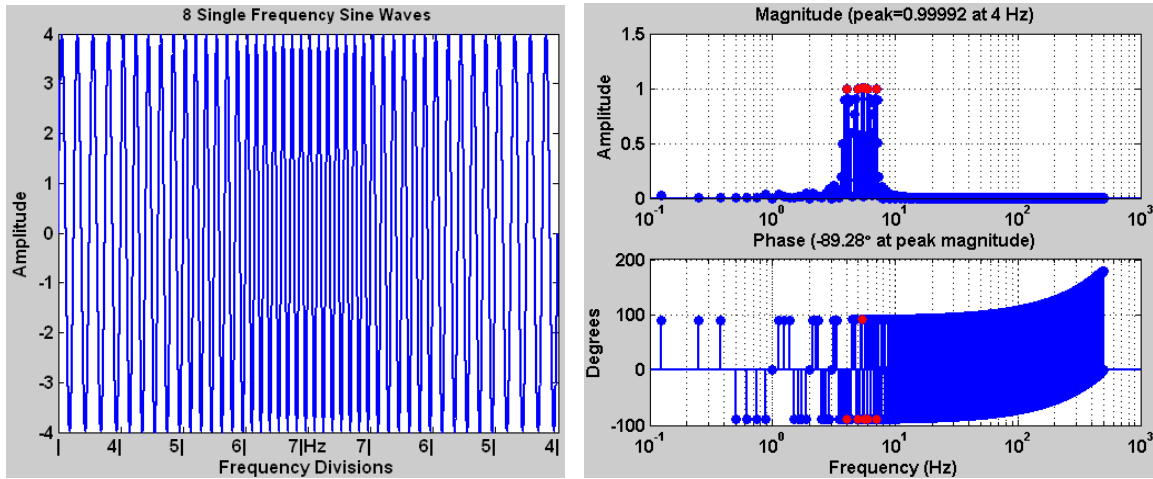


Figure 2-5. Eight single frequency sine waves placed side by side (left); FFT frequency spectrum (right)

The concatenation of waves provides a constant amplitude in the time domain and creates sections of single, observable frequencies. However, there is still a limitation on the number of different frequencies for dynamic analysis.

2.3.5 Swept Sine Wave

One method to acquire a wider frequency range is to generate a swept sine wave. A swept sine wave is a sine wave with a continuously varying wavelength; each point on the swept sine wave is a different wavelength. For the ring gauge, the wave begins at a long wavelength and progresses to a short wavelength in the first 90 degrees. To produce a continuous wave, the wave is “flipped” to line up with the last wave and then the wavelength increases to the starting point as it reaches 180 degrees. From 180 to 360

degrees, the wave is a mirror image of the first 180 degrees. Four quadrants of the same wavelengths allow a smaller section to be measured. Figure 2-6 illustrates these features.

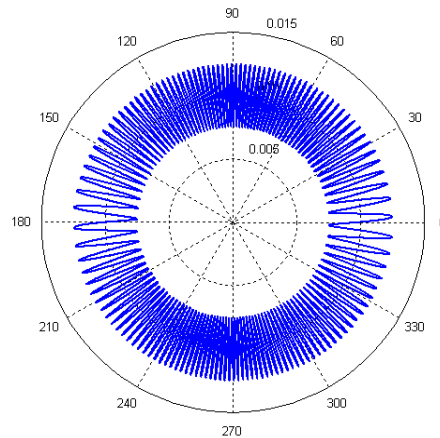


Figure 2-6. Swept sine wave on the OD/ID of the ring

The allure of the swept sine wave is that it contains a wide range of wavelengths. Different measurement speeds widen the frequency range for the transfer function while the spatial wavelength remains the same. The swept sine wave creates a frequency-rich environment such that the dynamics of the CMM can be seen.

The swept sine wave can assess the capability of the CMM to respond to small surface anomalies and to characterize the dynamic performance of the CMM as it traverses the varying wavelength features. Depending on the radius of the probe, measurement speed, radius of the part and size of features, the ability to detect small perturbations changes. If a small-radius probe was used to measure a part with small anomalies, the question arises of how the overall measurements would be affected. The different frequency of each wave creates a multitude of values to be evaluated which approximates different size features. The potential spatial wavelength of the entire feature may range from 1/4" (6.35mm) to 1/80" (0.317mm). (The smallest wavelength was selected to allow a 1 mm

diameter probe to fit into the valley of the wave.) However, the actual spatial wavelength will vary from 6.4mm to 0.4mm due to fabrication limitations. Because linear modulation was used to generate the wavelength content of the wave, there are fewer points per wave at the shortest wavelengths; this coupled with poorer FTS dynamic characteristics at the higher frequencies create more errors in the wave. So lengthening the shortest wavelength reduces some of the error by adding more points per wave. Depending on the speed of the measurement and the size of the probe, the CMM may or may not be able to measure the entire wave. However, by taking a series of measurements with different speeds, the unique dynamic characteristics of the CMM may be determined based on the probe used. This data will facilitate a decision on machine capabilities pertaining to a part measurement. Also, data from one CMM can be compared to data on another CMM to uncover the differing capabilities between the machines. Since all frequencies will be present within the range, the analysis of the FFT of a CMM's measurement becomes more difficult.

2.3.5.1 Swept Sine Wave Excitation

The values of the swept sine wave with an amplitude of 5 μ m were produced based on a minimum and maximum spatial wavelength. Because the wavelengths can be considered as individual frequencies, an FFT can be performed on the data set. With sampled data, the units on the frequency spectrum plot are in terms of Hertz. However, with the generated spatial data, it is more useful to plot the results in terms of wave numbers². The wave number is the reciprocal of the spatial wavelength. Figure 2-7 shows the FFT of the first quadrant of the ideal wave for the ID. The magnitude is largest near the

² The number of waves per unit distance (quarter of the circumference of the ring).

shortest wavelength at wave number $223/\lambda$ which translates to a wavelength of $0.537\mu\text{m}$. The phase values accumulate for half of the wavelengths and then return to zero due to the unwrapping function.

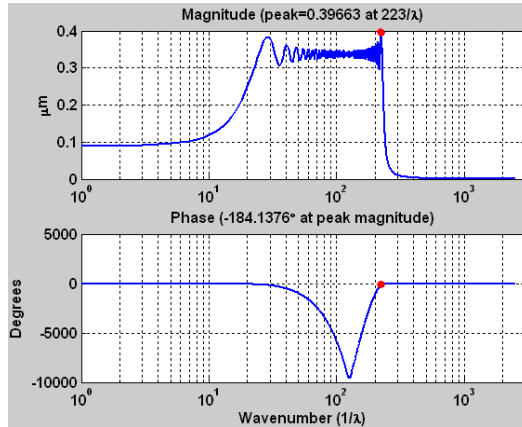


Figure 2-7. FFT of the first quadrant of the swept sine wave ($5\mu\text{m}$ amplitude) on the ID

Figure 2-8 represents the FFT of the ideal swept sine wave. The swept sine wave was generated with a maximum amplitude of $5\mu\text{m}$ and 20,000 points. The plot indicates a maximum magnitude of $0.342\mu\text{m}$ and 90° phase at wave number $32.5/\lambda$; although the magnitude looks relatively constant, every other value (or half of all values) is zero. The small magnitude is a characteristic of each wavelength only occurring 4 times and few of the other wavelengths equaling the maximum amplitude. The phase is also alternating from $+90^\circ$ to 0° to -90° and vice versa. This is due to the repetition of the individual frequencies in each quadrant; the location of each wavelength is shifted by 90° from the previous location.

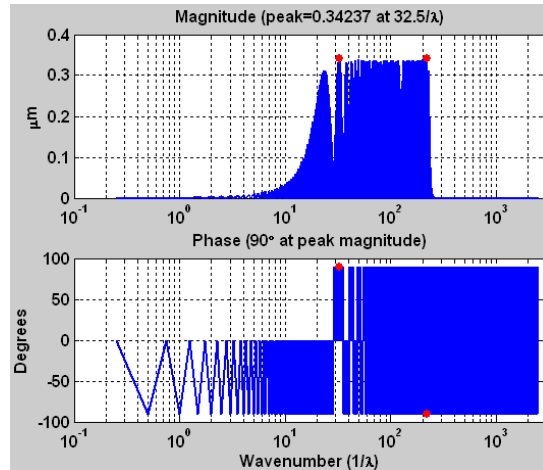


Figure 2-8. FFT of swept sine wave with maximum amplitude of 5 μm and 20,000 points

The FFT of the swept sine wave is difficult to interpret as compared to a single frequency sine wave due to the constantly varying nature of the wavelength. Rather than strictly interpreting the FFT and directly comparing it to an FFT of an actual measurement, the data analysis may be simplified.

A CMM has dynamic characteristics that will influence the overall measurement of the artifact. Since the swept sine wave on the surface of the ring is known and the CMM measurement will generate another data set, the CMM's dynamics, or transfer function, may be found using a form of deconvolution [19]. Convolution in the time domain is the multiplication of the swept sine wave and the impulse response of the dynamic system to construct an output that shows the influence of these dynamics. Since the dynamics of the CMM are not known, the inverse of convolution, or deconvolution, is used; the CMM measurement is divided by the accepted swept sine wave. To expedite calculations, deconvolution may be executed in the frequency domain. The magnitude and phase components in the frequency domain are separated to create a Bode plot of the CMM's dynamics. Figure 2-9 denotes a theoretical dynamic system. Multiple measurements

with different speeds will create the desired frequency range of the Bode plot to determine the natural frequency of the system.

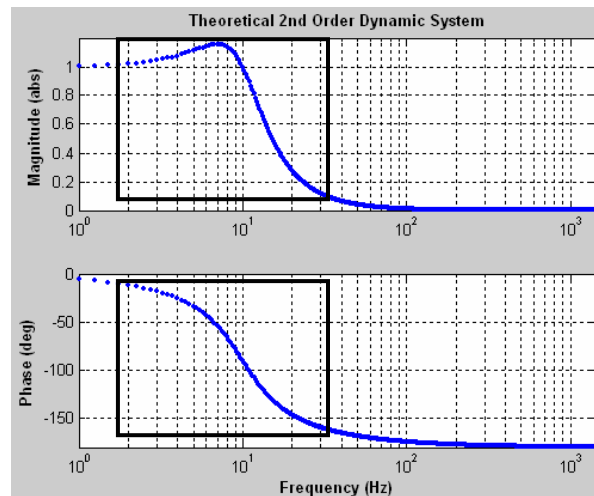


Figure 2-9. Theoretical second-order dynamic system

The transfer function of the CMM provides a significant amount of information about the machine. It specifies the natural frequency as well as the machine's performance within a frequency range. If a measurement speed is specified, the speed may be converted to frequencies present in the swept sine wave data and an appropriate CMM operating speed determined based on the transfer function and an acceptable amount of error. One measurement speed may correspond to the window illustrated in Figure 2-9. The actual measurement in the time domain should look similar to Figure 2-10. The figure shows the ideal swept sine wave with the anticipated swept sine wave measurement using the specified measurement speed on top of the ideal wave.

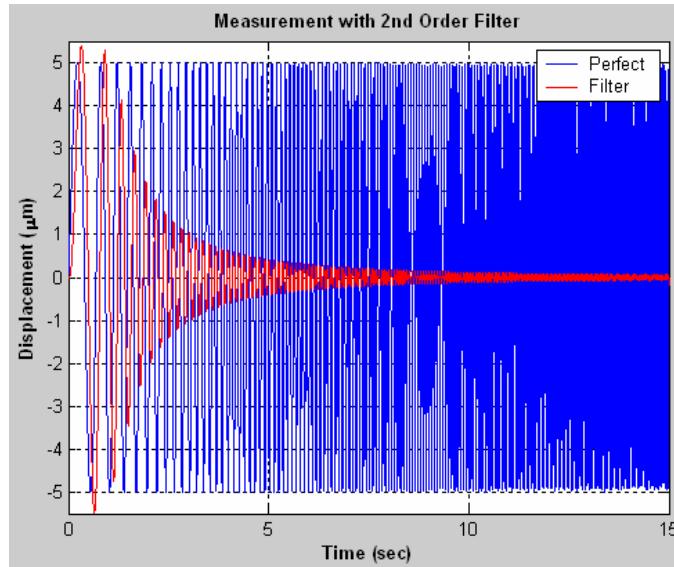


Figure 2-10. Simulated swept sine wave measurement

The Bode plot (Figure 2-9) suggested that the measurement would indicate an increased amplitude of the wave at the lower frequencies before it decreased when the natural frequency of the system was reached; the measurement should include some phase from the beginning. These attributes are observable in the time domain plot of Figure 2-10.

3 ARTIFACT FABRICATION

3.1 ALUMINUM ARTIFACT

The fabrication procedure and mounting scheme of the ring gauge was tested with the fabrication of an aluminum artifact. To machine the surfaces of the ring gauge, the ring is bolted to three – 1” long spacers that are attached to an 8” diameter, ½” thick disk (Figure 3-1). The disk is mounted to a vacuum chuck on the diamond turning machine. The ring has three counter bores on each side so that it can be flipped over to machine both sides. The following section describes the machining process. Figure 3-1 demonstrates the assembly of the disk, spacers, and ring gauge.

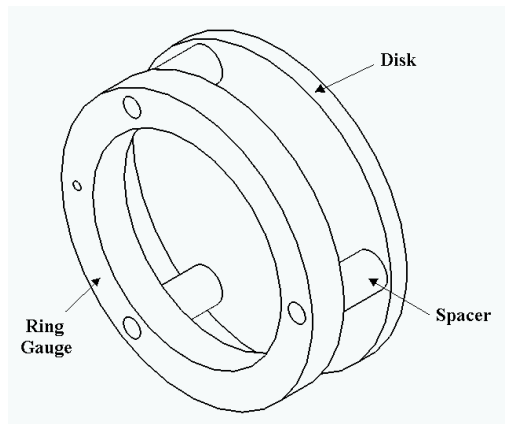


Figure 3-1. Assembly of ring on mount

3.1.1 Machining Ring Structure

The disk, spacers, and ring were rough machined³ with the finish machining completed at the Precision Engineering Center (PEC) on the ASG2500 Diamond Turning Machine (DTM). The DTM spindle includes an aerostatic bearing, a pulse width modulating

³ Weststar in Holly Springs, NC

(PWM) amplifier, a DC servomotor and a 20,000 count rotary encoder (see “Rotary Encoder” in Section 7.1.2). The DTM also has two independent axes that are operated via hydrostatic bearings, 5mm pitch ball screws, PWM amplifiers, DC servomotors and laser interferometer feedback. The vacuum chuck is attached to the end of the spindle but it cannot secure a hollow cylinder like the ring gauge. The solid disk was manufactured for this purpose while the spacers provide clearance for the cutting tool and Fast Tool Servo (FTS) when machining the ID. Each surface of the ring were machined to obtain a better surface finish and to improve the flatness of the surface profile because the CMM will use the surface as a datum for measurement.

Mounting procedure:

1. The three spacers were bolted to the aluminum disk.
2. The disk was placed on the chuck of the DTM and held by a vacuum of approximately 20in. Hg. The back of the disk had been flycut which produced a final PV of 2 μ m.
3. The ring was attached to the spacers by bolts with spherical washers between the bore and the bolt. The spherical washers were used to keep the ring from warping on the spacers under the screws. With the spherical washer, the screw allows for all three moments while restricting the three translational directions.

It is important that the ring is centered with respect to the spacers. A lever-type electronic gage head was placed on the ID of the ring. The gage head functions as a shaded-pole inductive pickup. As the vacuum chuck was rotated by hand, the inductor

showed the “high” and “low” spots on the ring. The bolts on the ring were loosened. By slightly tapping the ring, the ring was adjusted to within $\pm 2\mu\text{m}$ of center.

After the ring had been centered, the top, ID and OD were turned with a CBN tool. The first step was to “touch-off” on the ring. The z-axis on the DTM was zeroed so that a specific depth of cut could be selected. The x-axis was arbitrarily set off to the right of the ring. Because the width of each face was 1” (25.4mm), the computer could be programmed so the x-axis would traverse the width. Due to the arbitrary relative origin of the x-axis, the DTM was programmed to travel 50mm to ensure complete machining of the top surface. The conditions for machining are shown in Table 3-1.

Table 3-1. Determination of feed rate

Machining Conditions		
Type of Tool	CBN	
Depth of Cut	40	μm
Spindle Speed	500	RPM
Radius of Tool	20.32	mm
Theo. PV	10	nm
Feed	0.040	mm/rev
Feed Rate	20.159	mm/min

A theoretical surface roughness for the surface was chosen to be 10nm. Based on the radius of the tool, the feed value in Table 3-1 is found from Equation (2). Feed is multiplied by spindle speed to determine the feed rate.

$$PV_{\text{Roughness}} = \frac{f^2}{8R} \quad (2)$$

It took four passes to achieve a flat surface. During the operation, oil⁴ was used on the tool as a coolant. The bottom of the ring also had to be turned. The ring was flipped over

⁴ Mobil® Mobilmet® Omicron cutting oil

and bolted down. The ring was centered again before it was turned. The depth of cut was set to $40\mu\text{m}$ and three passes were necessary.

The OD of the ring was turned in the same fashion as the top and bottom surfaces except that the x-axis was used to touch off while the z-axis was arbitrarily set. The OD needed three passes with a $40\mu\text{m}$ depth of cut to obtain a flat surface. However, during the operation, the chips collected on the tool and may have contributed to some scratching on the surface. The setup to turn the ID of the ring was somewhat complicated (see Figure 3-2). The relative z-axis position was set slightly off the inside edge of the face near the spacers. The tool traverses from the inside to the outside so that the clearance between the FTS and the disk does not become a problem. The depth of cut was $40\mu\text{m}$ and took two passes to obtain a flat surface.

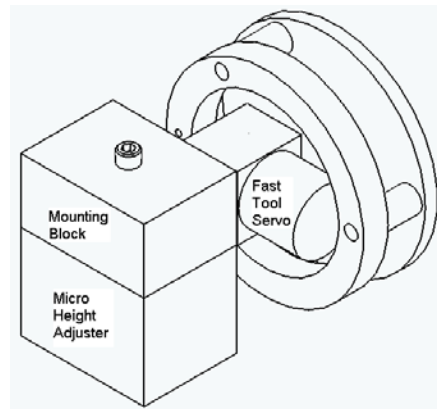


Figure 3-2. Setup for machining of the ring gauge with the FTS on the ID

The ring gauge includes a hole through its thickness that serves as an angular reference during the measurement process. The perpendicularity of the hole was checked using a lever-type electronic gage. Beginning at the edge of the hole and proceeding to the opposite edge, the values ranged from $-2\mu\text{m}$ to $12\mu\text{m}$ or approximately 0.03 degrees. It

was determined that this error was not significant enough to warrant improvements on the hole.

3.1.2 Swept Sine Wave Machining Process Development

3.1.2.1 Ring Analysis

To select the operating conditions to machine the swept sine wave on the artifact, a finite element analysis was completed on the ring gauge in SolidWorks/Cosmos. The frequency analysis was performed by fixing a restraint on each counter bored surface and applying a fine mesh to the entire ring. Figure 3-3 represents the first mode shape at a natural frequency of 1400Hz and simulates the maximum deformation of the ring. Two of the sections between the counter bores bend in one direction while the third section bends approximately twice as much in the opposite direction. The counter bores slope along with the bending section. Although the deformation would occur in the direction of the top and bottom surface and not the ID/OD, it should still be avoided during machining.

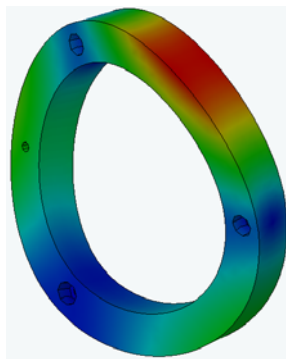


Figure 3-3. First mode shape of natural frequency

The features of the swept sine wave were to vary from 80 waves per inch to 4 waves per inch. It was possible to meet this requirement and stay below the ring's natural frequency if the ring was spun at 20RPM. Table 3-2 shows the conversion from spindle speed to

the frequency at the longest and shortest wavelength. The wavelength is converted to degrees per wave using the circumference of the ring. This value transformed into seconds per wave using the spindle speed. The inverse of seconds per wave calculates the frequency of the individual wave. The highest frequency reached would be ~480Hz which is much less than 1400Hz.

Table 3-2. Determination of minimum and maximum frequency during fabrication

20	RPM
0.333	rev/sec
152.4	mm ID
478.8	mm circumference

Shortest Waves	80	waves / in	Longest Waves	4	waves / in
	3.150	waves / mm		0.157	waves / mm
	1508	waves / rev		75	waves / rev
	0.239	degrees / wave		4.775	degrees / wave
	0.0020	seconds / wave		0.0398	seconds / wave
	502.7	Hz		25.1	Hz

3.1.2.2 FTS Analysis

The natural frequency of the Fast Tool Servo (FTS) (see “Fast Tool Servo” in Section 7.1.4) was another consideration for machining the swept sine wave on the ring. The piezoelectric stacks of the FTS are excited by the signal from a high voltage amplifier. The frequency and voltage signal affect the movement of the tool on the FTS. Any unexpected vibration of the tool would change the amplitude of the wave. Therefore, it is important to know the natural frequency of the FTS. A Stanford Network Signal Analyzer was used to generate a sine wave that sweeps through a range of frequencies. This sine wave is different from the wave machined on the ID of the ring in that it does not return to the starting frequency but rather increases to a maximum frequency. The output from Stanford was sent to dSPACE (see “dSPACE” in Section 7.1.1). dSPACE is a data acquisition system that facilitates the input and output of a Simulink control model.

In dSPACE, the wave was offset to make it entirely positive because the piezoelectric actuator cannot handle a negative voltage. The modified signal entered the high voltage amplifier where the signal was multiplied by 100 to drive the FTS. A capacitance gage captured the output of the servo and was recorded by Stanford. The swept sine wave began at 1Hz and ended at 7000Hz. The magnitude characteristic of the open loop system dynamics (Figure 3-4) seems to begin increasing around 600Hz until the first natural frequency (~5000Hz) is reached. The fabrication of the wave on the ID will occur below 600Hz.

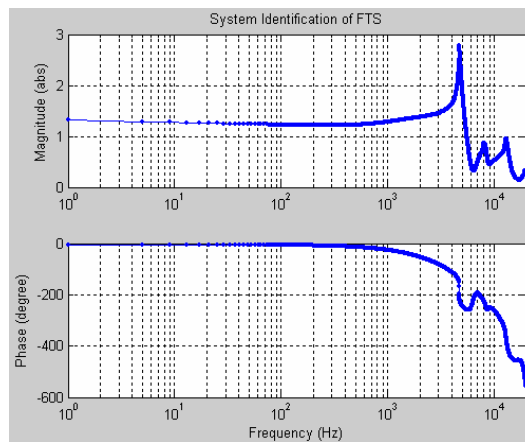


Figure 3-4. Open loop characteristics of the FTS

3.1.3 FTS Open Loop Control

The capacitance (cap) gage (see “Capacitance Gage” in Section 7.1.3) on the FTS is used to measure the displacement of the tool as it is moved by the piezoelectric stacks. For the first prototype, the decision was made to operate the FTS without position feedback (open loop mode) because the amplitude and phase were considered low. Therefore, the cap gage was not used to monitor the displacement. However, it was needed to verify the magnitude of the FTS motion as commanded by the controller. Before it could be used

for verification, it had to be calibrated. The lever-type electronic gage was calibrated using the laser interferometer on the DTM before being used to calibrate the cap gage.

A rotary encoder mounted onto the DTM keeps track of the angular position of the spindle and can also measure the rotational speed. The encoder output can be monitored through the program ControlDesk that displays the Matlab/Simulink model. The pin connectors were re-wired to create the correct configuration before being inserted into dSPACE.

Simulink was used to develop open loop commands from dSPACE to drive the FTS. One of the key elements to the Simulink program was a look-up table. A Matlab program (see “Swept Sine Wave” of Section 7.4.1) generated the points of the swept sine wave. Inputs to the program included amplitude, starting frequency, a linear modulation parameter, length, and number of data points. The length is equivalent to a quarter of the circumference to generate one quadrant of the wave; this quadrant is concatenated to produce the entire wave around the circumference. The number of data points was limited to the number of counts of the encoder (10,000). Each point from the look-up table is referenced by a single count on the encoder. The function box, the box labeled Fcn in Figure 3-5, corrects for the displacement of the FTS when a specific voltage is present by applying an equation to the voltage. Finally, the signal was sent to the FTS. Figure 3-5 represents the Simulink model.

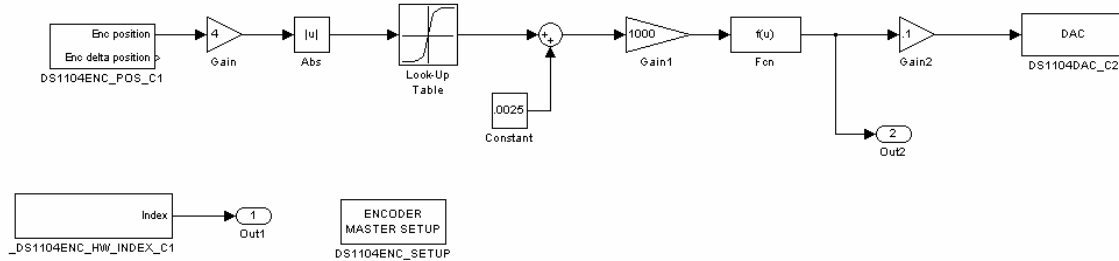


Figure 3-5. Simulink model of FTS control

Equation (3) represents the equation in the Fcn box in the Simulink model.

$$f(u) = 0.0006u^3 - 0.0213u^2 + 0.7121u + 0.044 \quad (3)$$

The equation was found by fitting a third degree polynomial to cap gage output data based on a linear voltage ramp of input data sent to the high voltage amplifier. The equation was meant to compensate for the hysteresis of the piezoelectric actuator of the FTS. Figure 3-6 shows half of the hysteresis loop that was only compensated. This was an error that was overcome with closed loop control later described in Section 3.3.1.

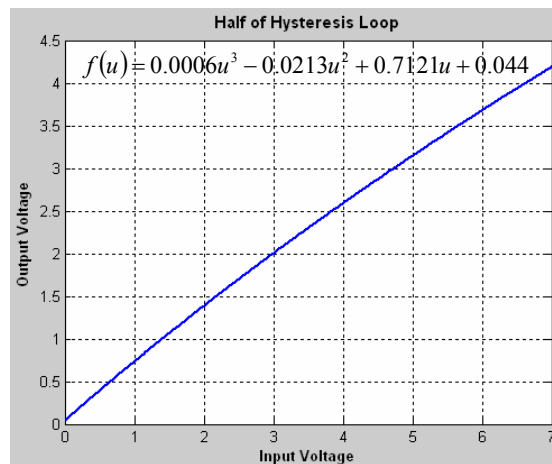


Figure 3-6. Cubic fit of PZT displacement

3.1.4 Fabrication

Before the swept sine wave could be cut into the ID of the ring, the ID had to be turned with a diamond tool to create a flat surface with a good surface finish. The ring gauge

was centered to within $4\mu\text{m}$; the rough machined OD surface made it difficult to center it better. Each bolt (zinc-plated steel, button head, $\frac{1}{4}$ "-20 thread machine screw) within the counter bores had 100 in-lbs of torque applied to it. The theoretical surface finish was 9nm peak-to-valley using a 0.5mm radius tool with a 2.1 mm/min feed rate and a 200RPM spindle speed in the clockwise direction. A total of $22\mu\text{m}$ was taken off each face. On the OD, a $30\mu\text{m}$, off-center groove was added to act as a protected reference surface. The off-center characteristic of the groove allows the user to differentiate between the sides of the ring. The groove was cut with the same feed rate and speed as the ID and the OD. Figure 3-7 displays a cross section of the ring gauge with grooves.

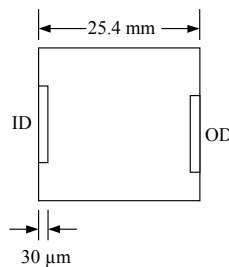


Figure 3-7. Schematic of Al ring cross section

The ID was faced off with the FTS. Figure 3-8 illustrates the following setup description. The servo was attached to a mounting block and placed on a micro height adjuster. A 17.5mm (0.689") aluminum spacer was needed between the mounting block and the height adjuster to get the tool to spindle center. Minor adjustments were made with the micro height adjuster to achieve a height of 6" (152.4mm) as defined by two gauge blocks. Previous measurements of this machine indicated the spindle center line was 6.00874" (152.622mm) above the x-axis surface plate. The ID was finished with a 2.4mm radius tool at a feed rate of 8.4mm/min and a spindle speed of 200RPM. Another groove was cut into the ID with the same feed rate and spindle speed; it was also $30\mu\text{m}$.

The purpose of the groove on the ID was to help protect the wave from damage. Finally, the swept sine wave was cut into the groove on the ID. There was no additional touch-off before the wave was cut; it was assumed the relative position of the surface was known based on the final cut of the groove. The depth of cut was equivalent to the instantaneous displacement (1-6 μm , as defined by the displacement from one encoder count to the next) of the wave with a total PV of 5 μm . The feed rate was 0.84mm/min with a spindle speed of 20RPM.

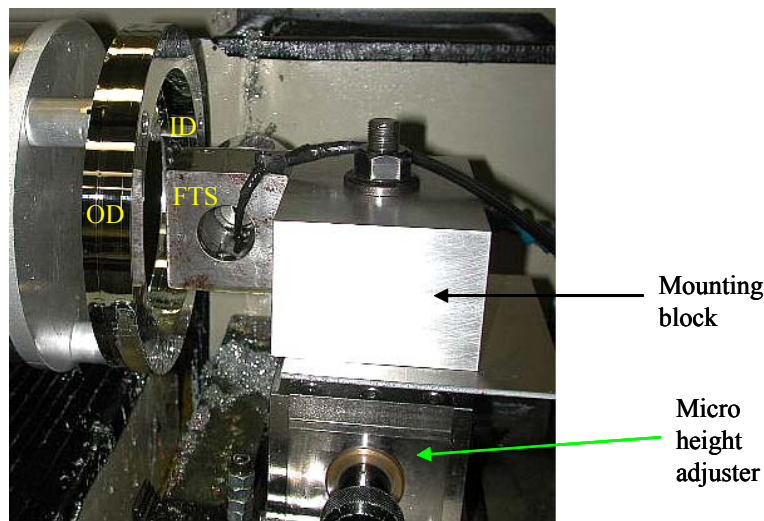


Figure 3-8. Setup with FTS and ring gauge

3.1.5 Artifact Analysis

3.1.5.1 Probe Calibration

After the swept sine wave was cut into the surface, it was measured using a Linear Variable Differential Transformer (LVDT) (see “LVDT” in Section 7.1.5). The LVDT was calibrated using the DTM and an oscilloscope. The LVDT is mounted to the x-axis; the probe is pointed perpendicular to the flat portion on the ID of the ring. While the LVDT is at the middle of its range, the x-axis is zeroed and instructed to traverse in

various μm increments. At each increment, the relative position of the x-axis laser is recorded along with the voltage output of the LVDT on the oscilloscope. After a series of measurements are taken, the points are plotted in Excel and a least-squares line is fit to the data. The slope of the line is used as the conversion factor from voltage to linear displacement. As shown in Figure 3-9, the conversion factor is $-0.24\mu\text{m}/\text{V}$ for the $\pm 2.5\mu\text{m}$ range associated with the instrument.

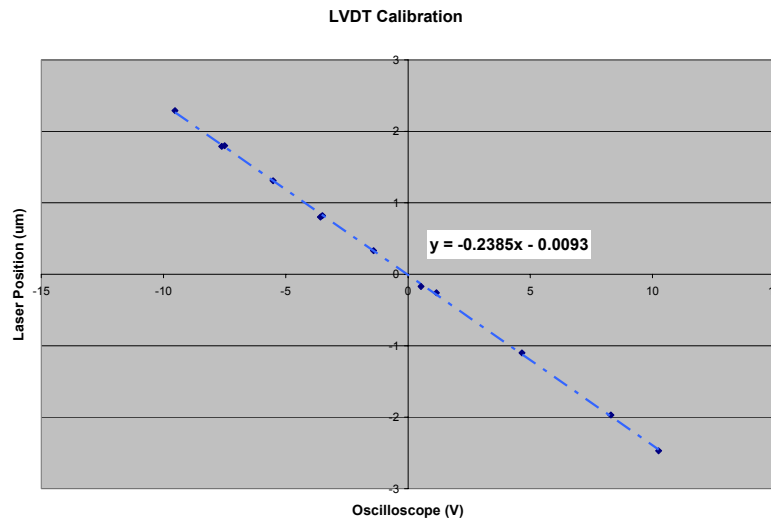


Figure 3-9. Calibration data of LVDT with best-fit line

The probe tip radius was measured using the Zeiss microscope and a video micro scaler with crosshairs. The radius is approximately 0.5mm which is slightly larger than the radius of curvature of the smallest wave; therefore, the probe will not be able to go into the valleys of the smallest waves.

The measurement demonstrated a decrease in amplitude from the $\pm 2.5\mu\text{m}$ goal. Figure 3-10 displays the measurement of the swept sine wave around the circumference. The wave starts with a low frequency, modulates to the highest frequency and reverts back to

the lowest frequency before returning to the highest frequency and finally ending where it first began.

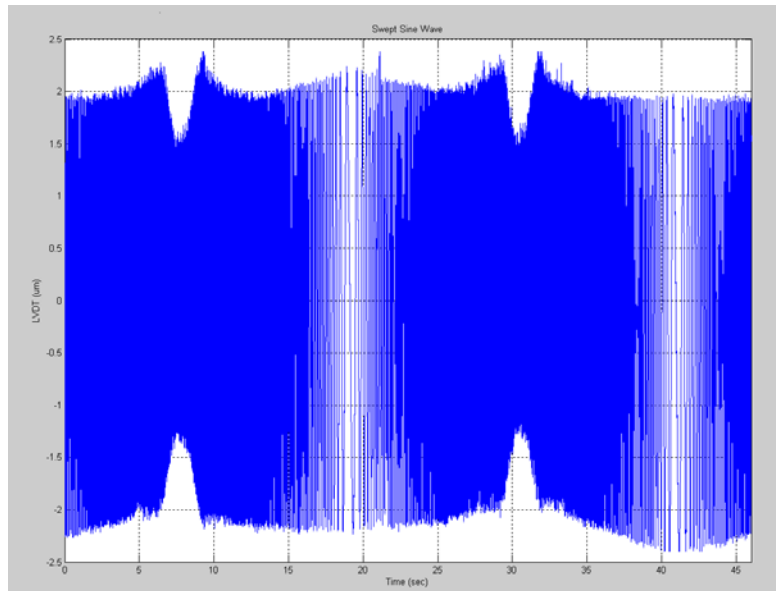


Figure 3-10. LVDT measurement of entire swept sine wave

It is apparent in Figure 3-10 that there is a large decrease in amplitude at the highest frequencies. As mentioned, this is partly attributed to the size of the LVDT probe (see Section 3.2.1.2). However, if the probe is not able to fit into the shortest wavelengths, the probe should bounce and indicate higher amplitudes on the surface of the wave. Instead, the amplitude at the peaks appears to decrease at the highest frequencies. It may be possible that the natural frequency of the LVDT has been exceeded which is causing the electronics to filter any large spikes⁵. The minimum constant rotational speed (~1 RPM) of the DTM may also be too fast for the LVDT measurement with the maximum frequency of the swept sine wave being 28Hz.

⁵ Refer to LVDT dynamics found in Section 4.4.1 – The transfer function indicates the measured amplitude would be only 90% of the true amplitude with 35° of phase at 28Hz.

3.1.5.2 Distortion of the Ring

The profile of the surface was observed with the GPI interferometer before and after the bolts were removed. The peak-to-valley (PV) values for the surface while the bolts were still torqued were 380nm, 712nm, and 858nm. Figure 3-11 shows the surface/wavefront map for a $\sim 130^\circ$ section of the top of the ring centered at one bolt location.

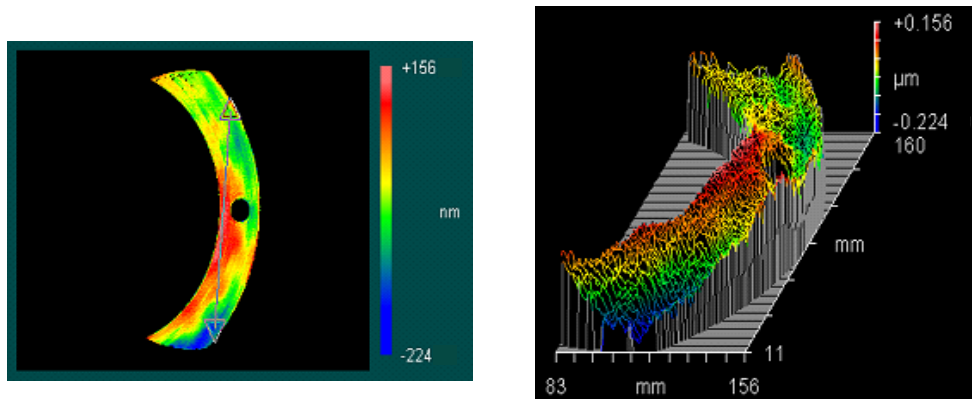


Figure 3-11. Surface profile of ring gauge with bolts in place

During fabrication, the ring was mounted onto spacers using three bolts as was described in Section 3.1.4. A force created by the bolt is applied to the thin section between the counter bores as shown in Figure 3-12.

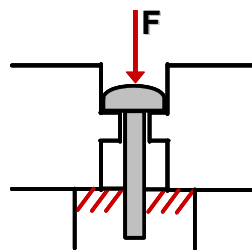


Figure 3-12. Cross section of ring attachment to spacers

When the bolts were removed, the difference in PV values increased by a factor of 10. Those values were $3.3\mu\text{m}$, $4.4\mu\text{m}$, and $4.7\mu\text{m}$. The amount of torque on the bolts was arbitrarily chosen which may have caused a distortion on the surface. Figure 3-13

magnifies the change in shape when the bolts are removed on the top surface of the ring near the counter bores; removing the bolts increases the slope.

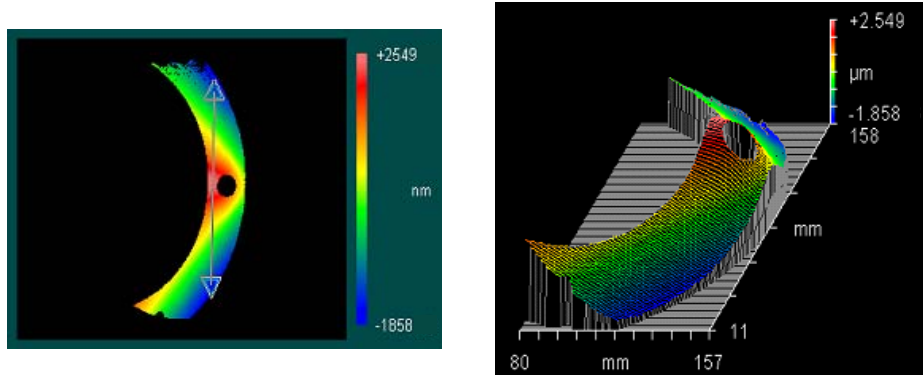


Figure 3-13. Surface profile of ring gauge with bolts removed

The apparent elastic deformation of the top surface caused by releasing the bolts will add uncertainty to the roundness measurement of the overall ring. The deformation creates 3 high spots at the counter bore locations and 3 low spots between each set of counter bores, or a total of 6 lobes are generated. Figure 3-13 illustrates one of the high spots at a counter bore and reveals the lower areas on either side of the counter bore. For this reason, the mounting method for fabrication will be altered as described in Section 3.3.3.

3.1.5.3 Y-12 Measurements

The ring gauge was sent to the Y-12 facility for further analysis and verification of shape. The correction for the lobes in determining the shape and amplitude of the swept sine wave after it has been measured will contribute to the uncertainty in the measurement. It was measured using a Coordinate Measuring Machine (CMM). The CMM and measurement setup is shown in Figure 3-14.



Figure 3-14. Ring gauge in a horizontal orientation on CMM (left) and scanning probe in contact with ring (right)

The ring gauge was placed on blocks in a horizontal orientation on a rotary table in Figure 3-14. The measurements at the PEC were made with the ring bolted to the spacers and in the vertical orientation. Neither measurement took advantage of the counter bore positions as kinematics supports. The scanning probe was placed in contact with the surface of the ring gauge. The gauge was rotated while the probe remained stationary. The results of the measurement are shown in Figure 3-15. The image on the left is a measurement of the swept sine wave placed on a polar axis; the right image shows the roundness of the ring with the measurement taken on the non-wave portion of the ID.

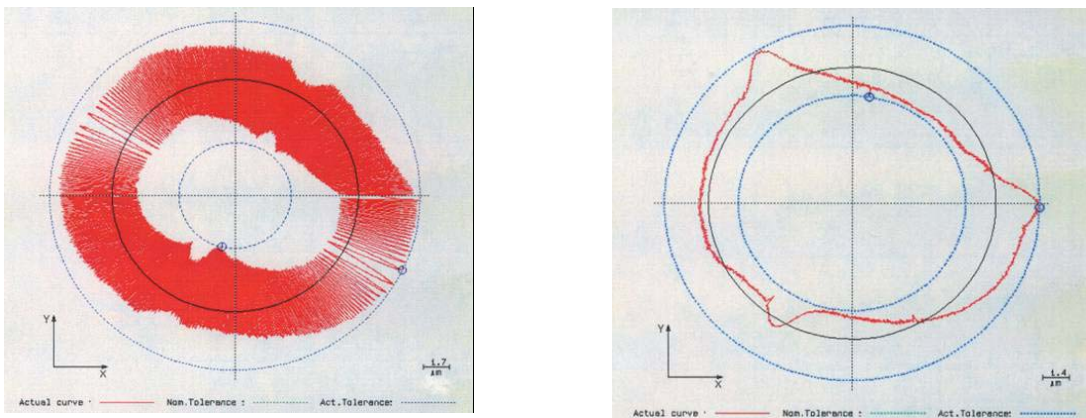


Figure 3-15. Measurement of the swept sine wave on the ID (left) and measurement of the roundness of the gauge (right)

The measured swept sine wave features shown on the left in Figure 3-15 indicate a reduction in amplitude as the wave approaches its shortest length. The reduction in amplitude is both at the peak and the valley of the wave. This distortion was also apparent in the LVDT measurements at the PEC as described in Section 3.1.5.1. The measurement of roundness, right image, confirms the lobes caused by the elastic deformation created by the bolts during fabrication. The ring is out-of-round by a PV value of 3.8 μ m. The ring was bolted to three spacers which were shown to cause some distortion when the bolts were removed. The amplitude reduction and distortion issues must be addressed before a final artifact can be produced.

3.2 CYLINDRICAL ARTIFACT

A second artifact was machined to determine the cause of the swept sine wave distortion. The aluminum ring gauge, in Figure 3-15, used open loop control without the use of a capacitance (cap) gauge position feedback to control the displacement of the FTS tool during fabrication. The source of the amplitude errors were studied by repeating the fabrication of a swept sine wave. To simplify the fabrication process, reduce distortion affects and record the cap gauge output, the sine waves were machined onto the OD of a 100mm diameter aluminum cylinder. Figure 3-16 shows the setup of the experiment. The swept sine wave signal was sent to the FTS open loop to reproduce the previous fabrication and to determine the associated errors.



Figure 3-16. Experimental setup to machine swept sine wave on OD of cylinder and the air-bearing LVDT used to measure the final shape

The cap gage output for the swept sine wave is shown in Figure 3-17, and it indicates an increase in displacement at the highest frequencies. This is consistent with the open loop characteristics of the FTS in Figure 3-4. However, a measurement of these same sine wave features shown in Figure 3-17 using the air-bearing LVDT exhibited the same features measured on the original ring gauge; that is, reduced amplitude at the higher frequencies. The discontinuity in the amplitude near the lowest frequencies is due to no features present rather than measurement error.

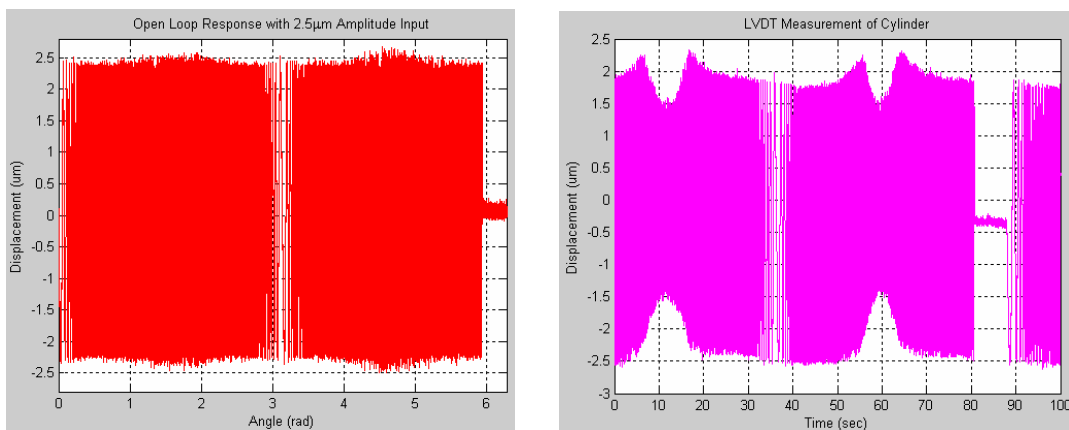


Figure 3-17. Cap gage reading of 2.5µm amplitude input (left); LVDT measurement of sine waves (right)

To verify the output of the cap gage, the output from the high voltage (HV) amplifier before it was sent to the FTS was monitored on an oscilloscope. The intention was to determine whether the amplifier had the same gain over the frequency range of interest.

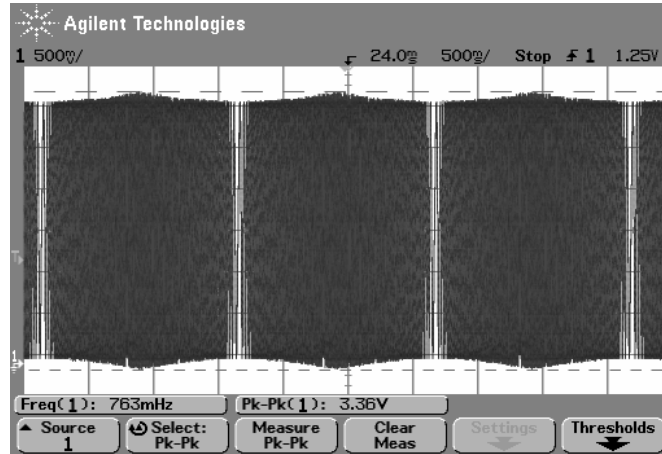


Figure 3-18. Swept sine wave output thru the HV amplifier as seen on an oscilloscope

Figure 3-18 illustrates the response of the amplifier. It is apparent that at the higher frequencies, the voltage increases as it is sent into the FTS. The peak-to-peak voltage measures 3.36V, which translates to 5.34 μ m of displacement. At the lower frequency section, the peak-to-peak voltage measures 3.11V or 4.93 μ m. The HV amplifier is adding its own dynamics to the system that is affecting the desired swept sine wave input.

3.2.1 Sources of Error

The difference between the cap gage reading and the LVDT was either due to fabrication or measurement. Several hypotheses were proposed and tested; they included tool clearance, size of LVDT probe tip diameter, LVDT electronics, and actual surface features.

3.2.1.1 Tool Clearance

The diamond tool on the FTS has a clearance angle (ψ) of 6° (Figure 3-19). The slope of a sine wave increases with the amplitude and the frequency. If the slope at the shortest

wavelength (highest frequency) is greater than the clearance angle of the tool, portions of the wave could be cut off. Equation (4) calculates the maximum slope of the swept sine wave.

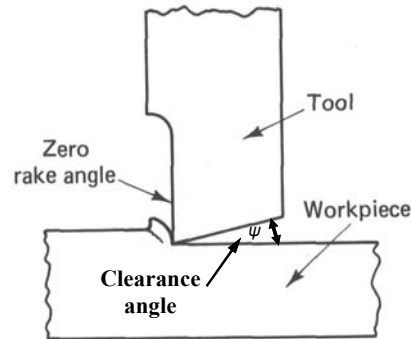


Figure 3-19. Chip formation during machining with associated angles [23]

$$Slope_{\max} = A * \left(\frac{2\pi}{L} \right) \quad (4)$$

where:

A = Amplitude of the wave (0.0025mm)

L = Minimum wavelength (0.317mm)

The maximum slope is 0.05 radian or 2.84° with the proposed values. On the cylinder, the shortest wavelength measured 0.186mm and 0.287mm on the ring gauge. This translates to 4.84° and 3.14°, respectively. Even though the shortest wavelength was shorter than desired, the waves are not cut off at the highest frequencies by the tool.

3.2.1.2 Probe Tip Diameter

The size of the probe used for measurement may also be an issue. There is a maximum probe size that is capable of fitting into each wave. The LVDT had a 1mm diameter probe. Probe compensation equations were applied to the commanded input to determine if and where the probe would not be able to measure [20].

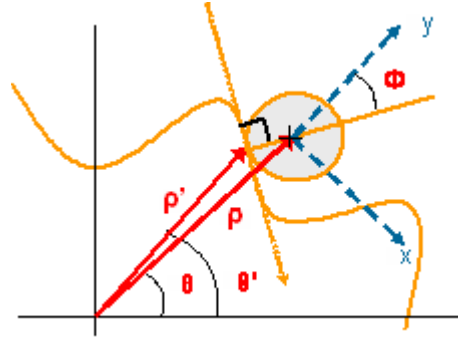


Figure 3-20. Probe compensation concept [20]

Figure 3-20 (image not to scale) demonstrates the concept behind probe compensation. The LVDT probe measures the wave as the part rotates on the DTM spindle. The measurement data contains the position of the center of the probe rather than the probe's position on the surface of the wave; the probe compensation equations find the surface position. The radius is measured from the center of the part where the probe is shown on the outside surface of the cylinder. The equations of the probe compensation are shown in Equations (5-7) with r as the radius of the probe [20].

$$\phi = \tan^{-1}\left(-\frac{1}{\rho} \frac{d\rho}{d\theta}\right) \quad (5)$$

$$\rho' = \sqrt{\rho^2 + r^2 - 2\rho r \cos \phi} \quad (6)$$

$$\theta' = \sin^{-1}\left(-\frac{r}{\rho} \sin(\phi)\right) + \theta \quad (7)$$

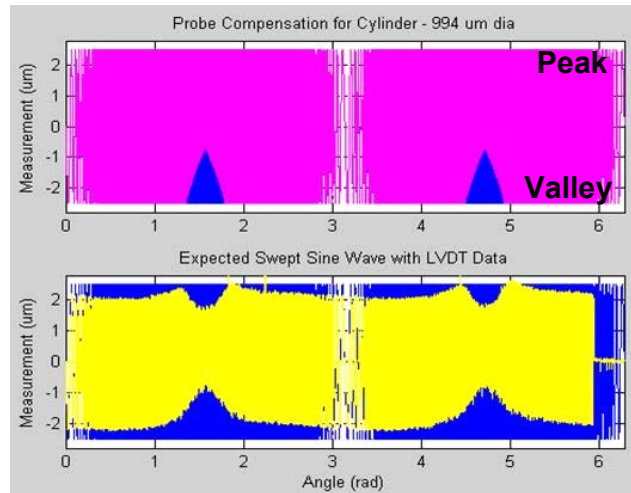


Figure 3-21. Top subplot is the expected measurement and bottom is actual LVDT measurement

The probe compensated data in the top subplot of Figure 3-21 showed that the LVDT probe could not measure the valleys of the wave (the absent triangular sections) but indicated that all the peaks could be measured. This may be attributed to a shorter than desired spatial wavelength (as discussed in Section 3.2.1.1) that prevented the probe from fitting into the valley of the wave. The reduction of the peak, at the top of the bottom subplot, at the shortest spatial wavelengths (0.187mm or 28Hz with 1RPM measurement speed) is due to the filtering of the instrument when the probe lost contact with the surface after not being able to properly measure the valleys (refer to Figure 4-5 in Section 4.4.1 for the LVDT dynamics). The compensation equations do not take into account the speed of measurement and assume exact following of the wave.

3.2.1.3 LVDT Calibration

The original LVDT reading was in units of voltage. To convert to a displacement to compare the measurement (bottom subplot) to the theoretical measurement (top subplot) in Figure 3-21, the LVDT had to be re-calibrated due to re-positioning of the probe. The

LVDT is mounted and the probe placed on a non-wave portion of the cylinder surface. The x-axis of the diamond turning machine is commanded to move $20\mu\text{m}$ and the voltage values are captured via dSPACE. The slope of the line is the conversion factor which is $-1.202\mu\text{m}/\text{V}$ using the instrument range of $\pm 12.5\mu\text{m}$. Figure 3-22 illustrates this process.

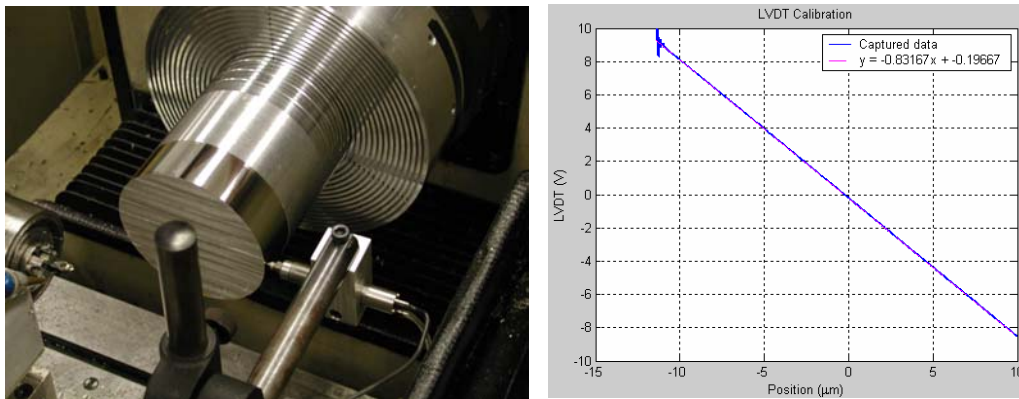


Figure 3-22. Setup of LVDT calibration (left), and determination of calibration slope (right)

3.2.1.4 Profilometer Measurement

The LVDT measurement exhibited an amplitude of less than $2.5\mu\text{m}$ as well as a greater drop in amplitude at the highest frequencies. The probe compensation indicated that the LVDT could not measure the valleys of the wave. To scrutinize the surface and determine the true amplitude, a second measurement was taken on the cylinder using a profilometer with stylus tip radius of $2.0\mu\text{m}$. The arm of the profilometer scanned across 12mm sections. Figure 3-23 shows the measurements at various frequencies.

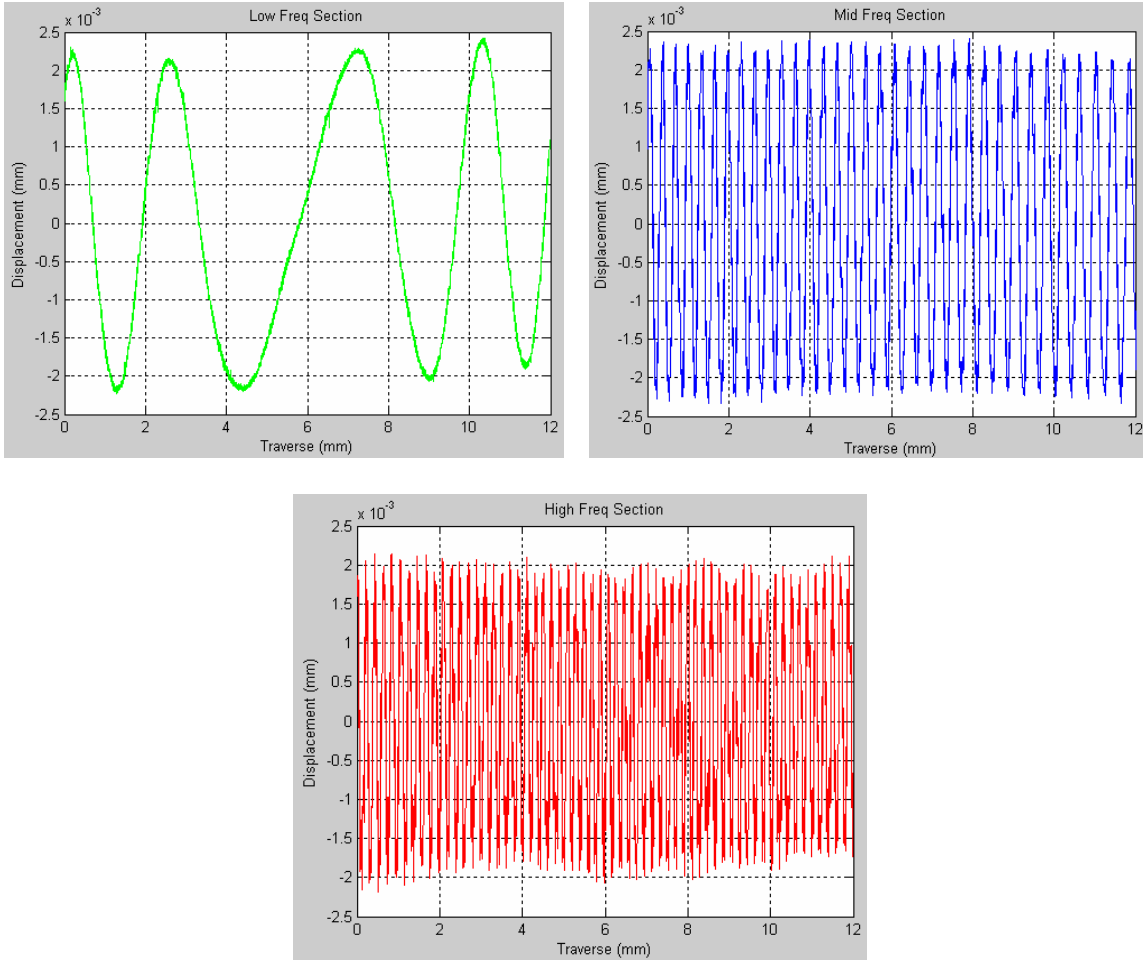


Figure 3-23. Profilometer measurement of swept sine wave

The profilometer measurement at the highest frequency clearly demonstrated an almost constant amplitude rather than a decreasing amplitude as shown with the LVDT. The smaller radius of the instrument probe fit into each wave, giving an accurate measurement of the wave. This confirms the decrease in amplitude in the valleys is due to probe size and attributes the decreases in amplitude at the peaks of the highest frequencies to the filtering of the LVDT (refer to Figure 4-5 in Section 4.4.1 for the LVDT dynamics). Closed loop control will be used to improve the fabrication of the swept sine wave.

3.3 FINAL ARTIFACT

After determining the sources of error associated with the fabrication of the aluminum ring gauge artifact, various changes were made to the fabrication procedure. Some of those changes are discussed in the following sections.

3.3.1 Closed Loop Control

To develop a closed loop control system, it is important to know the open loop response of the FTS. (Section 7.2 describes the algorithm to capture the response using LabView) Figure 3-24 shows the magnitude ratio and the phase between input and output. The first natural frequency occurs at approximately 5150Hz; the point where the magnitude peaked and the phase went through -180° . The magnitude was determined by dividing the output voltage by the input voltage. The swept sine wave will be cut into the surface in the 10 to 600Hz range. Even in this range, there is a change in the magnitude as well as phase. There is an initial phase lag of 4° that increases to 16° . A closed loop control system has been developed to correct these errors.

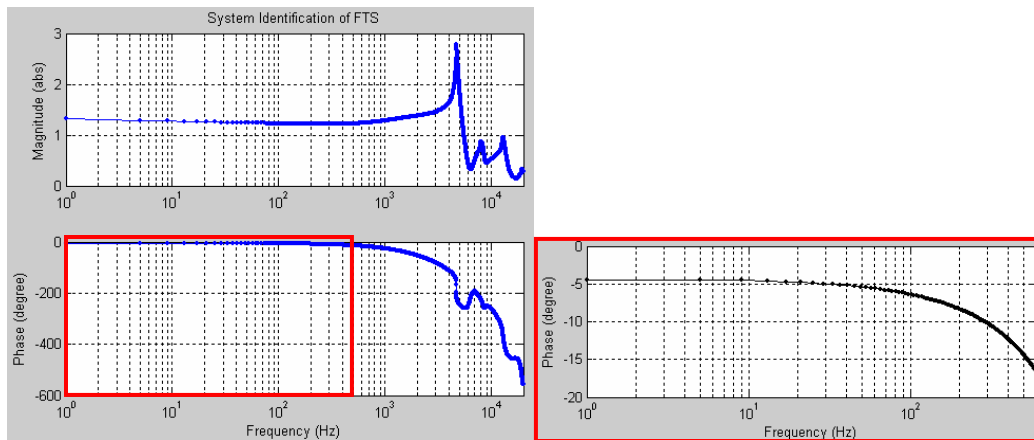


Figure 3-24. System characteristics of the FTS with larger view of phase from 1-600Hz

One complication when using piezoelectric actuators (PZTs) is that they add hysteresis to the motion and, as a result, the gain for the system is a function of the amplitude. Figure

3-25 illustrates this phenomenon. The three curves are for 100%, 75% and 20% of the range of motion. Note that the peak-to-peak (P-P) voltage divided by the P-P motion is not a constant: it varies from 1.846 to 1.365 at 100% and 20% respectively. This is a significant drop in gain; 25% from the full range to 20% of full range. As a result, the open-loop transfer function will change with different amplitudes of the swept sine wave. Such non-linear behavior may complicate control for an arbitrary input shape.

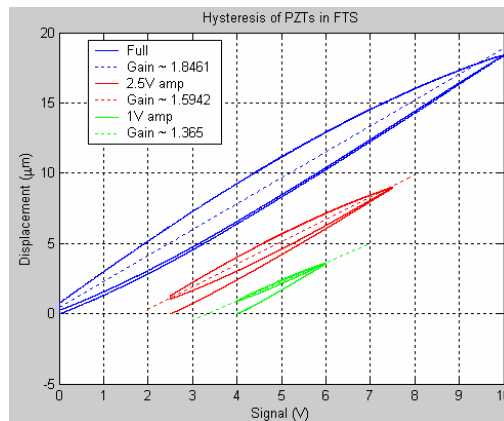


Figure 3-25. Hysteresis loops for different amplitudes of motion for the PZTs in the FTS

Feedback control can correct for position error at low frequency. The closed loop controller uses feedback from the capacitance gage position sensor along with a proportional-integral (PI) control algorithm to correct position error. Gains are selected to shape the response of the system, to prevent overshoot and to correct for the following error. However, the hysteresis of the PZTs, shown in Figure 3-25, created complications in compensating for both magnitude and phase of the system. The final value of the gains for the controller were chosen based on the production of the quickest response of the system without introducing instability and the realization of a constant magnitude over the operating frequency range of the FTS.

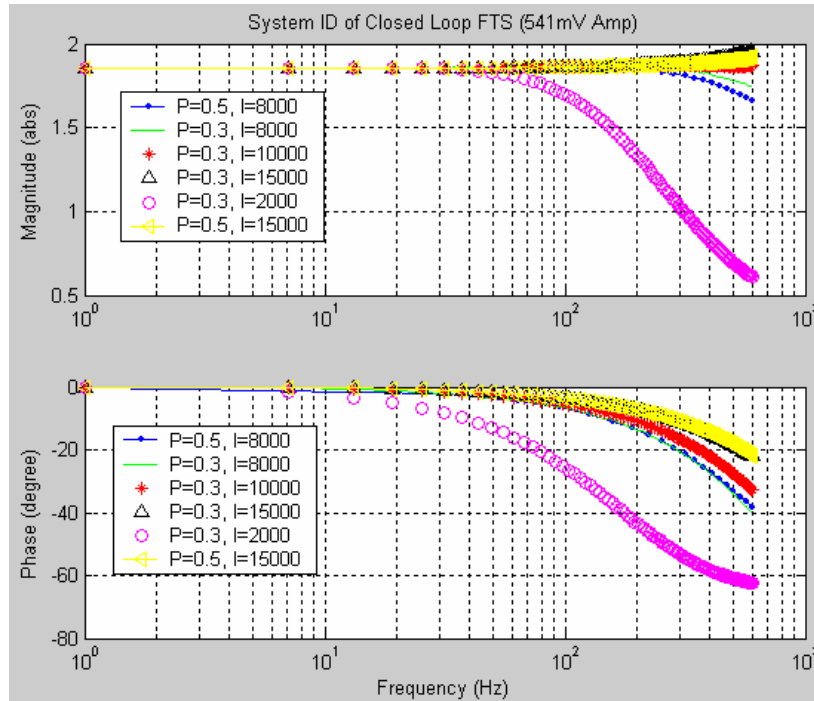


Figure 3-26. Various parameters for the PI gains of the closed loop controller

An integral controller (K_i) reduces rise time, increases overshoot and settling time but eliminates steady-state error. A proportional controller (K_p) will also decrease rise time and increase the amount of overshoot. Since K_p creates similar effects to the system, the proportional gain is reduced when used in conjunction with an integral gain [22]. Figure 3-26 shows the closed loop system response from 1 to 600Hz for a range of proportional (P) and integral (I) gains. A proportional gain of 0.3 is used to produce a constant magnitude with the chosen integral gain. The integral gain controls how quickly the system reaches its given input; a gain of 10,000 has been chosen. Although an integral gain of 15,000 (left-pointed triangle) generated the quickest response and had less phase lag, the magnitude was more constant with the integral gain of 10,000 (asterisk). The amount of phase lag was not a concern since the method of deconvolution (Section 3.3.2) would be used to correct for it.

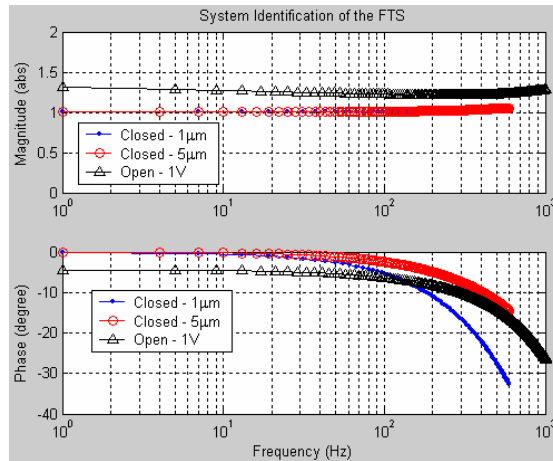


Figure 3-27. Comparison of closed and open loop system identifications up to 600Hz

Figure 3-27 shows the closed loop system response with the optimized PI controller as compared to the open loop response and also demonstrates the change in the transfer function with input amplitude. The “circles” and “dots” in the figure correspond to the closed loop response using two different amplitude inputs, 5µm and 1µm respectively; the “triangles” relate to the open loop response with approximately the same input as the 1µm input of the “dots.” The magnitude remains constant in the operating range of interest in all responses. For the 1µm input, there is less phase lag at low frequency but it becomes larger than the open loop value for frequencies greater than 100Hz. However, for the desired amplitude of 5µm, the phase and magnitude are consistently better than the open loop system.

3.3.2 Deconvolution

Although the system dynamics of the FTS have improved with closed loop control, there is still significant phase error in the system at higher frequencies. Since the FTS will operate at close to 600Hz, deconvolution is applied to the swept sine wave before it is input into the controller. Deconvolution uses the magnitude and phase characteristics of the FTS with the information of the desired wave output to adjust the amplitude, phase

and shape of the command signal. Deconvolution is the complex division of the desired output over the frequency response of the system [19]. Thus, it alters the input to produce an expected output.

The deconvolution algorithm is applied in a series of steps. The first step is to determine the transfer function of the closed loop system. The transfer function was captured via LabView (see Section 7.2 for details of the procedure). A starting and ending frequency (Hz) and number of points for the sweep were specified. The voltage was sent out through LabView to the high voltage amplifier where it was input into the FTS. The closed loop system of the FTS was controlled by dSPACE hardware.

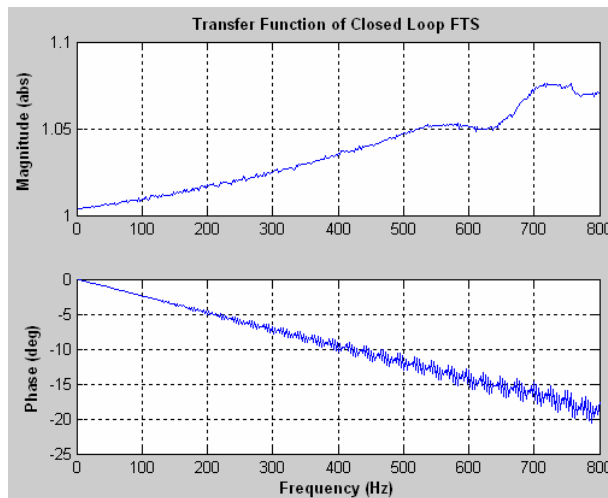


Figure 3-28. Closed loop FTS transfer function up to 800Hz

The transfer function of the closed loop system up to 800Hz is shown in Figure 3-28 with a linear frequency axis. The real and imaginary components (complex values) of the system were captured and converted into magnitude and phase. After the complex values of the system transfer function are captured, they are interpolated to produce the appropriate step size of the frequency output to match the step size of the frequency of

the FFT of the desired swept sine wave. The interpolated complex values are used to find the complex conjugate used in the Fourier transforms.

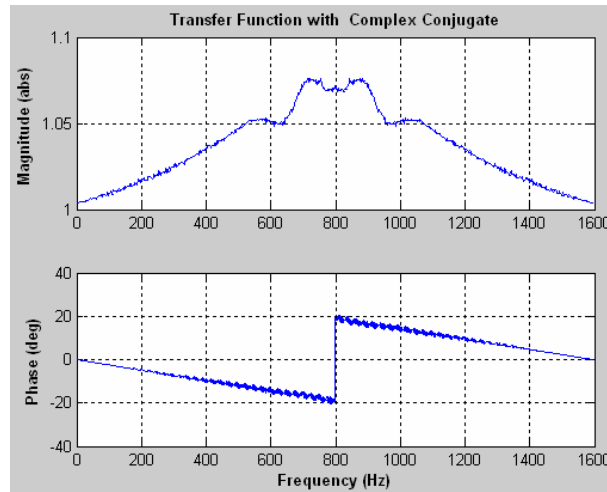


Figure 3-29. FTS transfer function complex values and their conjugate

The complex values with their conjugates (Figure 3-29) were interpolated again to increase the frequency range of the transfer function. The sampling theorem states that “a discrete time sequence obtained by sampling a continuous function contains enough information to reproduce the function exactly, provided that the sampling rate is greater than twice the highest frequency contained in the original signal [19].” When the frequency range is extended, as in Figure 3-30, the response inside the gap between the original response and its conjugate is unknown. The straight line links the separated responses with their last value, creating the correct frequency content. Expanding the range of the system transfer function increases the sample rate to match the sample rate of the input signal [19].

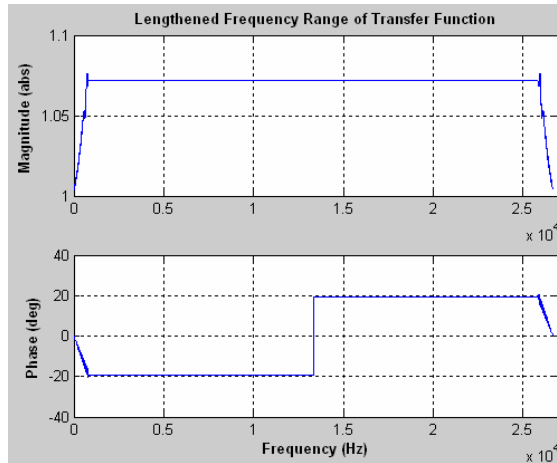


Figure 3-30. Frequency range of transfer function increased

The next step in the deconvolution process is to take an FFT of the desired output signal to convert the time domain signal into the frequency domain with complex values. Recall, deconvolution is division of complex signals in the frequency domain [19]. The FFT of the swept sine wave is divided by the previous interpolated transfer function in Figure 3-30. An inverse FFT is taken of this quantity to convert the signal back into the time domain. The result produces the adjusted input command for the controller. Figure 3-31 demonstrates the adjusted amplitude as the frequency of the wave changes. The dark background is the desired shape and the light color is the input wave that will produce that desired output. Figure 3-32 exhibits the phase lead of the input command signal to compensate for the phase lag of the system, especially at the higher frequencies. The wave with dots (adjusted) is commanded prior to the desired wave as represented by the time of each zero-crossing.

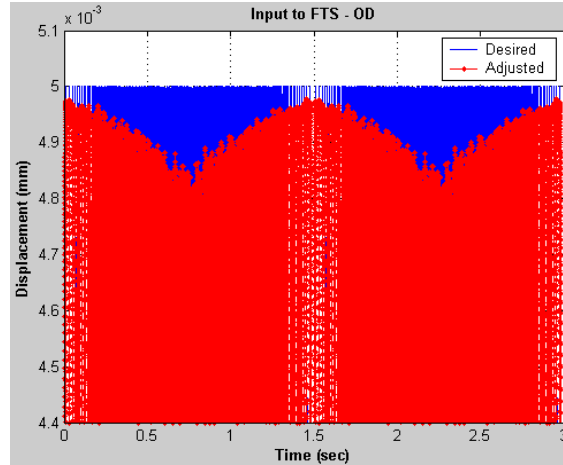


Figure 3-31. Expanded section of adjusted input (dots) to demonstrate altered amplitude;
time relates to spindle speed

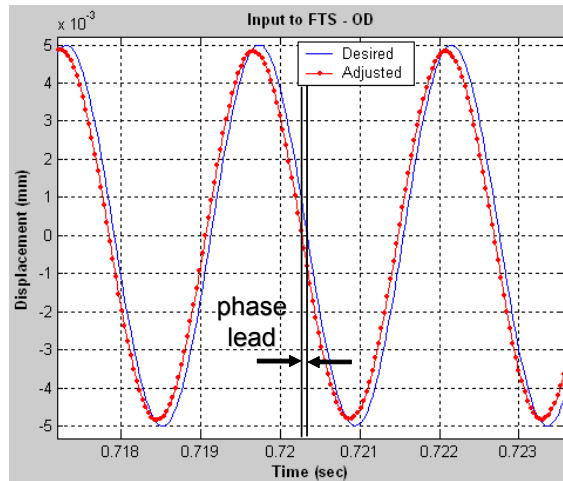


Figure 3-32. Expanded section of adjusted input (dots) to show phase-lead and
amplitude reduction of input signal

Deconvolution in combination with closed loop control greatly decreases the amount of error in the fabrication of the swept sine wave. Much of the error in the closed loop controller alone is due to phase lag (16° at the highest frequency); whereas with the open loop system, the error is a combination of the phase lag and magnitude. Figure 3-33 demonstrates the decrease in error from open loop (left) to closed loop (middle) to closed loop with deconvolution control (right). The top subplots illustrate the system response

as the bottom subplots show the difference between the desired and actual responses or the error. The error has been reduced from $\pm 3\mu\text{m}$ to $\pm 0.3\mu\text{m}$ with deconvolution.

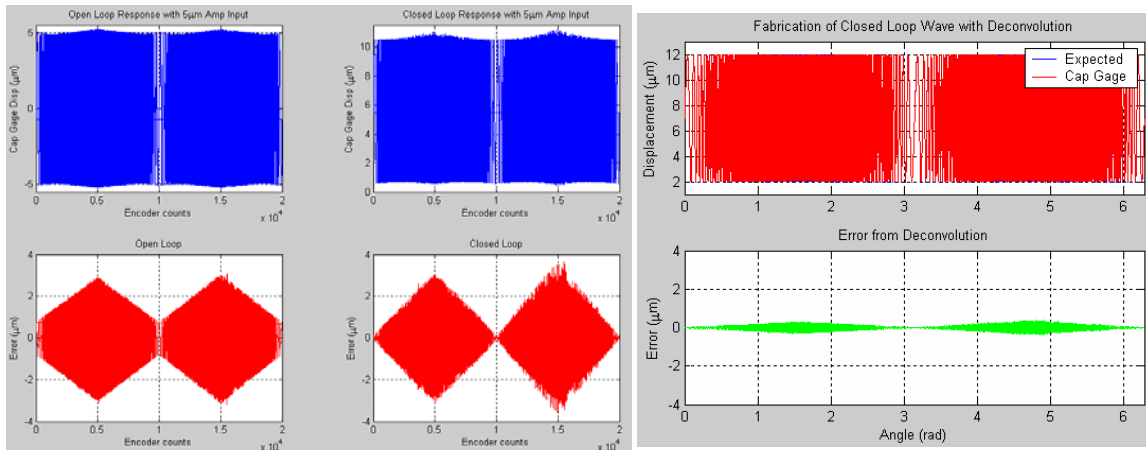


Figure 3-33. Comparison of control methods

3.3.3 Ring Design Modifications

The most significant problem with the overall shape of the ring gauge was due to the mounting technique as described in Section 3.1.1. The aluminum ring was attached to the spacers with 100in-lb of torque applied to each bolt which led to distortion of the ring shape. The obvious conclusion is to apply less torque to the bolts. After calculation, it was determined that approximately 5in-lb would be more appropriate.

Other alterations to the ring gauge design were also made to lessen the distortion influence. Instead of placing counter bores on the opposite sides of one bolt location, the counter bore could be placed on one surface and then the other counter bore applied on the opposite face but rotated 60° . Figure 3-34 illustrates this idea. The modified design inhibits deformation because the compression force of the bolt is applied to a thicker section with the opposite surface resting on the spacers whereas with the first design, the

force is applied to a thin section which responds similar to a cantilever beam due to the double counter bore configuration.

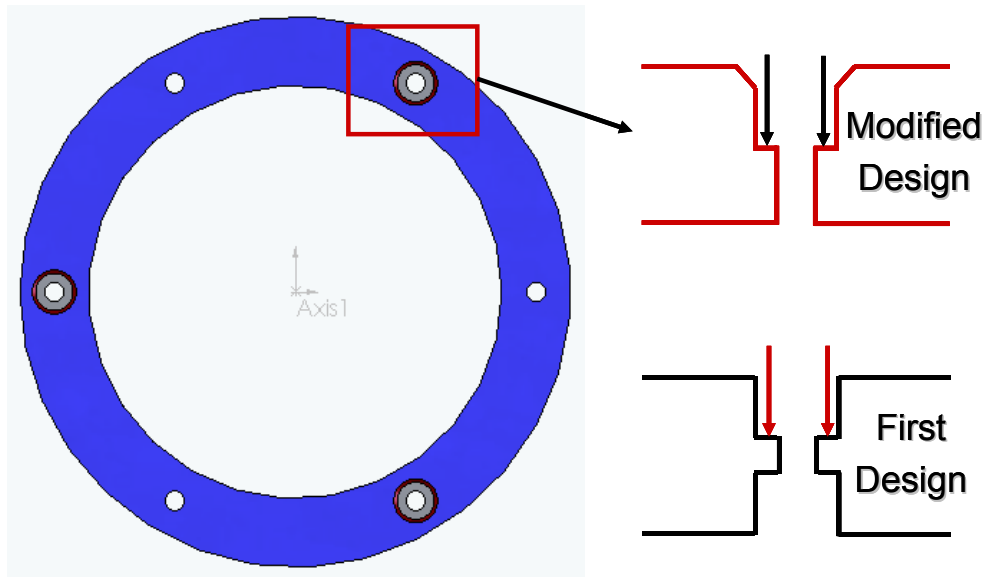


Figure 3-34. New design of the ring gauge artifact

It should also be noted that a 45° chamfer is placed on the edge of the counter bore. The chamfers will be used to support 3 steel balls in the horizontal orientation during CMM measurement.

Another point of significance is the change in material. As mentioned in Section 2.1.1, the trial ring gauge was Al 6061-T6 whereas the final ring gauge will be 17-4PH stainless steel plated with electroless nickel. The steel is stiffer than the aluminum which will also decrease the amount of distortion caused by the bolts.

3.3.4 Ring Tolerances

The revised ring gauge design includes a number of tolerances to ensure quality of the artifact. Those specifications were for concentricity, parallelism, perpendicularity, and total run out. Figure 3-35 shows the specified tolerances before final diamond turning.

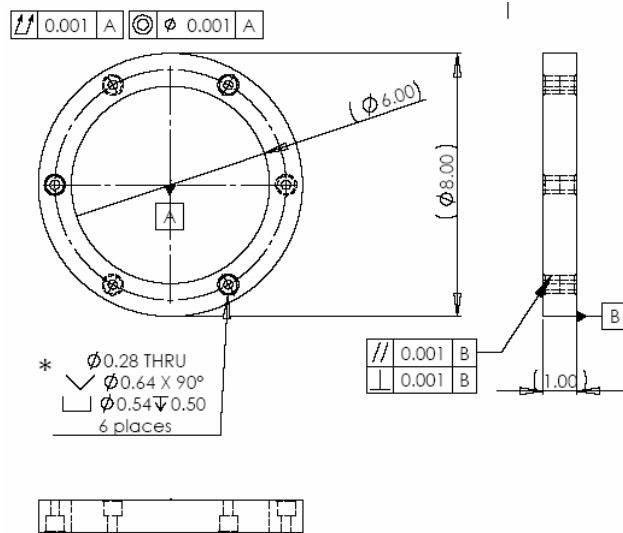


Figure 3-35. Drawing with tolerance specifications of ring gauge

Concentricity defines the relationship between one center and another. By choosing the center of the ID, the center of the OD must lie within a 0.001" diameter zone of the ID's center. Tolerancing the concentricity along with the total run out ensures the uniform thickness of the ring. Total run out is referring to the control of all surface elements around a datum axis. The tolerance uses the datum axis of the ID center. Specifically in terms of the ID and OD, when the surface is rotated 360°, the entire surface must lie within a 0.001" tolerance zone at every position of the placement of the indicator [21].

A parallelism tolerance has been specified to guarantee the hole surface center lies within a 0.001" tolerance zone around the hole center datum axis which is equidistant from the OD and ID of the ring. The perpendicularity tolerance assures that the holes are perpendicular to the top and bottom surfaces of the ring [21]. The 0.001" tolerance value chosen was to ensure that the 0.006" electroless nickel plating layer is sufficient for machining.

3.3.5 Preparation for Fabrication

After the ring gauge was dimensioned and tolerances added, two rings (Ring 1 and Ring 2) were rough and finish machined⁶. The 17-4PH stainless steel was roughed to its general shape, leaving 0.100 inch excess stock on all surfaces. A water jet with garnet particles was used for the rough machining. The rings were solution annealed⁷ to relax internal stresses. They spent 1.5 to 2 hours residence time in an air furnace at 1900°F (1038°C) ± 25°F and then were air cooled. Lastly, the annealed rings were finish machined⁶. The 45° chamfers were added to the counter bores, and both rings were machined to a 64µin CLA surface finish and cleaned with a solvent.

The final heat treatment⁷ of the rings consisted of the following process. The rings were aged in a vacuum furnace for 4 hours at 900 - 940°F (482 - 504°C). They were cooled in a vacuum to below 150°F (65°C). The last step was a cycle stabilization process in a cam-controlled oven. The rings were heated up to 250°F then cooled to -50°F. The successive temperatures in the cycle were 200°F, 0°F, 100°F, and 25°F. The cycle stabilization is intended to give maximum dimensional stability to the artifact.

After the rings had been heat treated, they were plated with electroless nickel⁸. Two of the existing through holes were tapped for 5/16"-24 threads for fixturing of each ring during plating. The final thickness of the electroless nickel is 0.006" or 150µm.

⁶ Weststar in Holly Springs, NC

⁷ East Carolina Metal Treating in Raleigh, NC

The fixturing caused some excess Ni to build up at the two counter bores used. Figure 3-36 depicts the location of the fixturing and clearly illustrates the non-uniformity in the surface of one of the rings.

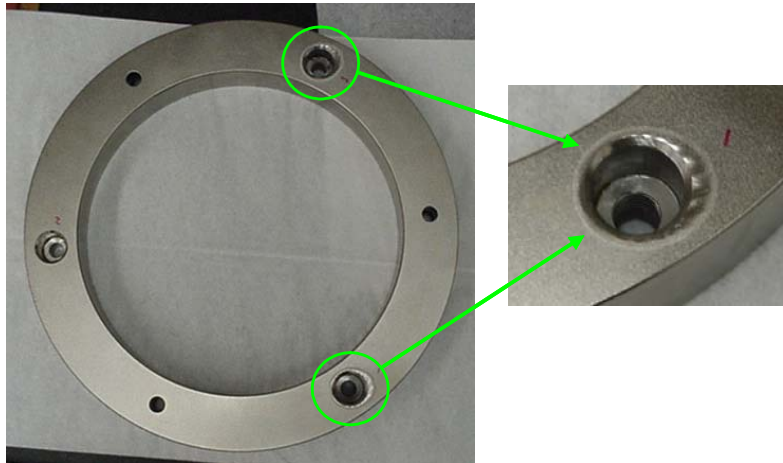


Figure 3-36. Ring 1 after plating with Ni build-up at two counter bores

The excess Ni did not create a problem with the datum surfaces because the two faces of the ring are machined flat during diamond turning. However, the chamfers had to be made uniform in depth and shape. Some excess material also was removed from the through holes to give clearance for the bolts and for the pilot of the valve seat cutter. An adjustable reamer was used for the through holes and a valve seat cutter was used on the chamfers.

⁸ Corning Net Optics in Keene, NH



Figure 3-37. Adjustable reamer (left); valve seat cutter (right)

The setup to finish the counter bores is shown in Figure 3-37. The rings were clamped to the table using the T-slots and the reamer was secured in the drill chuck of a milling machine. This setup assured a 90° alignment with the top surface of the ring. The reamer consists of four blades that will remove material as the tool is rotated clockwise. After each through hole was reamed, a pilot was inserted for the valve seat cutter. The cutter head slides onto the pilot and sits at a 45° angle on the surface. The T-wrench snaps on top of the cutter head and is also rotated clockwise with light pressure. The valve seat cutter head consists of three tungsten carbide seat blades that remove a small amount of material while producing a satin finish.

The excess Ni around two of the counter bores led to chips at the edges of these counter bores after the valve seat cutter was used. Although aesthetically undesirable, it exposed the stainless steel and the Ni plating thickness could be verified before the ring was machined. The Talysurf profilometer was used to traverse into the chipped surfaces of both rings. Figure 3-38 is representative of Ring 1 and indicates that the thickness is approximately 0.006”.

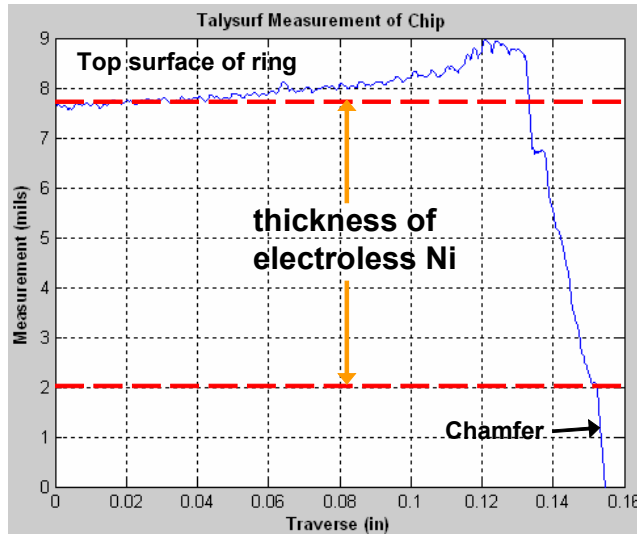


Figure 3-38. Verification of plating thickness for Ring 1

The depths of the chamfers on each side of the rings were also measured with the Talysurf profilometer. The probe tip began on the top surface of the rings and traversed across into the chamfer. The chamfers were specified to be 0.050” in depth.

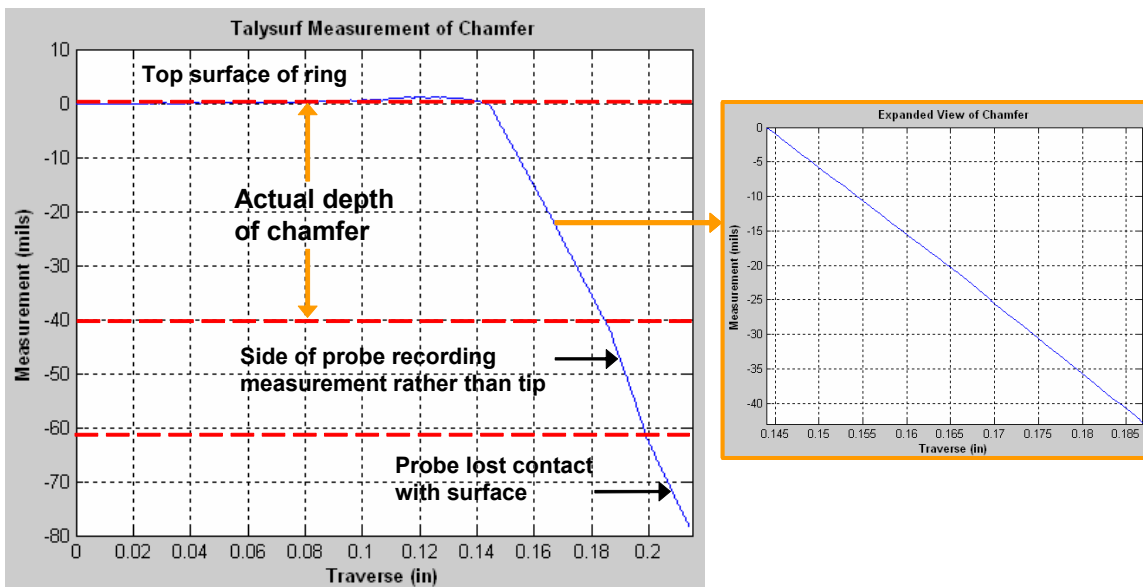


Figure 3-39. Profilometer measurement of a chamfer on Ring 1

The depth of each chamfer varies slightly (Figure 3-39). On side 1 (the side with chipped counter bore edges), the mean depth is about 0.046” with a standard deviation of less than

0.001”. It differs from specification by almost 0.004”. Side 2 has a mean chamfer depth of 0.051” with a standard deviation of 0.0035”. Its error from specification is about 0.001”.

Table 3-3. Individual chamfer depth measurements for Ring 1 (all values in inches)

0.046	Side 1	0.047	Side 2
0.047		0.051	
0.046		0.054	
0.0463	Mean	0.0507	Mean
0.0006	StDev	0.0035	StDev
0.634	Max dim	0.648	Max dim
0.632	Min dim	0.634	Min dim

Although the depth of each chamfer differs from specification, it is imperative that the maximum diameter (“max/min dim” in Table 3-3) at the top of the counter bore be larger than the cord length of the support balls for the ring. To be correctly supported, there should only be one line of contact on the chamfer. The cord length is determined by multiplying the diameter of the ball (7/8”) by the cosine of 45°; it is 0.62”. Each chamfer meets this criteria.

3.3.6 Fabrication

3.3.6.1 Machining of each face

The disk with spacers was mounted to the chuck on the DTM and held by ~20in Hg of vacuum. The bolts attaching the spacers to the disk were tightened before mounting. After the disk was secured on the chuck, it was centered using a lever-type electronic gage. The gage head was brought into contact with the OD of the disk and the spindle was rotated. When the instrument indicated a “low” spot, the top of the disk was tapped with a plastic hammer. This process continued until the disk was centered. Due to the rough machined surface of the disk, it was centered to within approximately 40µm.

The next step was to machine the spacers flat. The FTS was secured on the x-axis and was aligned to be perpendicular to the surface of the spacers. For touch-off, the spindle on the z-axis was moved closer to the tool. When the tool was close to the surface, a microscope was setup to focus on the tool. The z-axis was stepped in slowly while the spindle was rotated counterclockwise. After the first chip was formed on the surface, the relative position of the z-axis was zeroed. The relative position of the x-axis was arbitrarily zeroed off of the inside edge of the spacers; the x-axis was commanded to travel a distance greater than 1" to completely machine the spacers. Figure 3-40 exhibits the touch-off procedure for the z-axis.

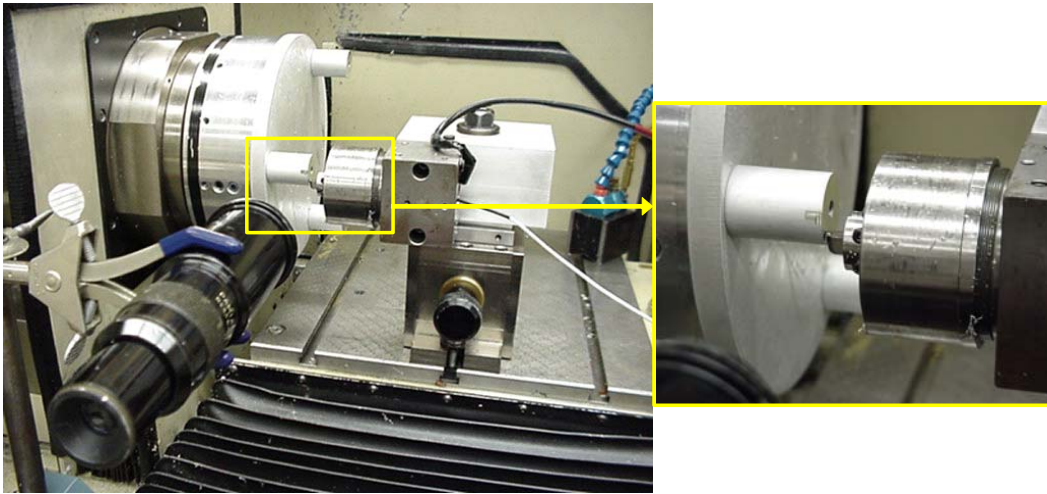


Figure 3-40. z-axis touch-off on the surface of the spacers

A 2.4mm radius diamond tool was used to machine the spacers. The tool traversed across the surface while the spindle was rotating 250RPM counterclockwise. A higher spindle speed with the larger radius tool created oscillation of the tool with the interrupted cut. A total of 15 μ m was removed from the surface in two machining passes.

Ring 1 was mounted to the spacers after they were machined. The spherical washers and the bolts were lubricated with oil before use. The bolts were loosely tightened so that the ring could be centered on the spacers. Once again, the lever-type electronic gage head was brought into contact with the ring and the spindle was slowly rotated. The surface finish of Ring 1 was better than the disk before machining, but there were 3 lobes created by the counter bores. Thus, the ring was centered by creating a uniform peak-to-valley value ($20\mu\text{m}$) of each lobe. After centering, 5in-lb of torque was applied to each bolt.

Another tool post with a smaller radius diamond tool (1mm) was used to machine each ring face. The tool post was attached to the x-axis and the tool was adjusted to be perpendicular to the ring surface. The same touch-off procedure was performed near the edge of the counter bores with the relative positions of the x- and z-axis set. However, after touch-off, the z-axis was backed away from the tool by $10\mu\text{m}$ because of the excess Ni at two of the counter bores. It was difficult to find the highest point on the face at touch-off because of these high regions.

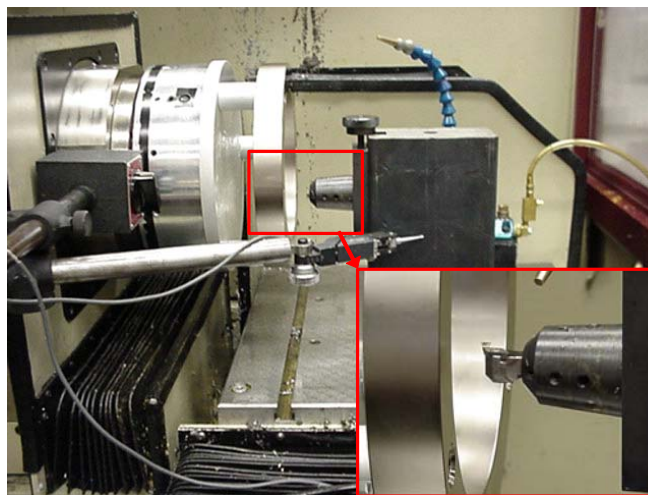


Figure 3-41. Setup to machine each ring face flat

The tool traversed across the surface at a feed rate of 4.47mm/min ($f = 8.8\mu\text{m}/\text{rev}$ with $\text{RMS}_{\text{theo}} = 3\text{nm}$) with a spindle speed of 500RPM counterclockwise. The higher spindle speed reduced the amount of time of the interrupted cut across the counter bores and negated most of the tool oscillation. The first few machining passes took off the excess Ni layer ($\sim 0.001''$ or $25\mu\text{m}$), which made it level with the rest of the face. The remaining passes used a $5\mu\text{m}$ depth of cut and took off a total of $45\mu\text{m}$ of Ni.

After the ring face had been machined flat, it was taken off the spacers and measured with the profilometer. The probe measured 22mm across the surface at locations before and after (see inset in Figure 3-42) the interrupted cut over the counter bores. The surface finish is approximately 19nm RMS while the surface profile measures $0.194\mu\text{m}$ PV, which will be sufficient to be used as a datum surface. Figure 3-42 also demonstrates the uniformity of the tool depth before and after the counter bores, indicating little tool oscillation. The left image exhibits the entire surface profile while the right image displays a small ($\sim 1\text{mm}$) section of the surface which was used for the surface finish calculations. The right image also indicates a long term variation (as compared to individual tool passes) in the surface that may be due to a small oscillation of the spindle during rotation and other machine errors.

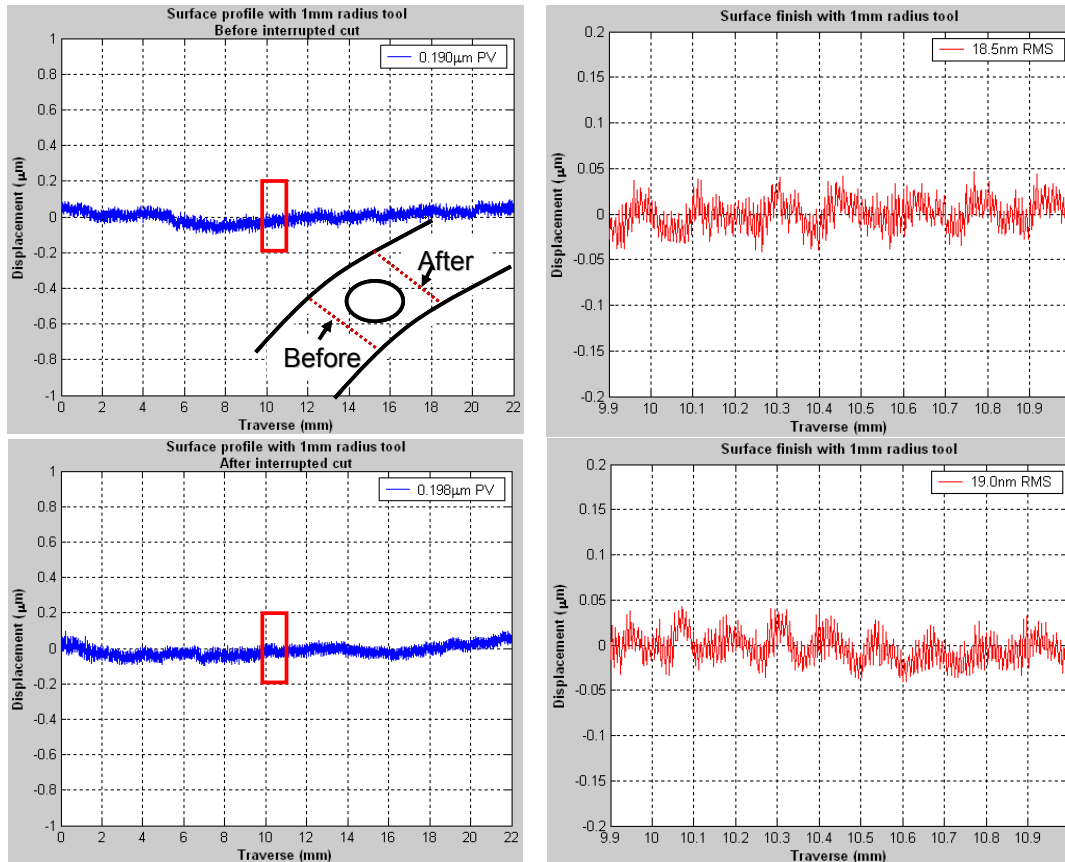


Figure 3-42. Profilometer measurements of first machined face of Ring 1 before (top) and after (bottom) interrupted cut

After the profilometer measurements, Ring 1 was flipped over and re-attached to the spacers. The ring was centered to within $\pm 20\mu\text{m}$ on the OD including the 3 lobes. 5in-lb of torque was applied to each bolt. Touch-off was executed near the ID of the ring and the relative positions of the x- and z-axis were set. The z-axis was backed off $10\mu\text{m}$ after touch-off. The spindle rotated at 500RPM counterclockwise with the 1mm diamond tool traversing across the face at a rate of 4.40mm/min. $33\mu\text{m}$ of material was removed from the Ni surface. The surface of the ring face was measured using the profilometer as described previously. The surface finish averages to $\sim 18.5\text{nm}$ RMS while the surface profile measures $0.170\mu\text{m}$ PV (see Figure 3-43). Again, note the long term variation.

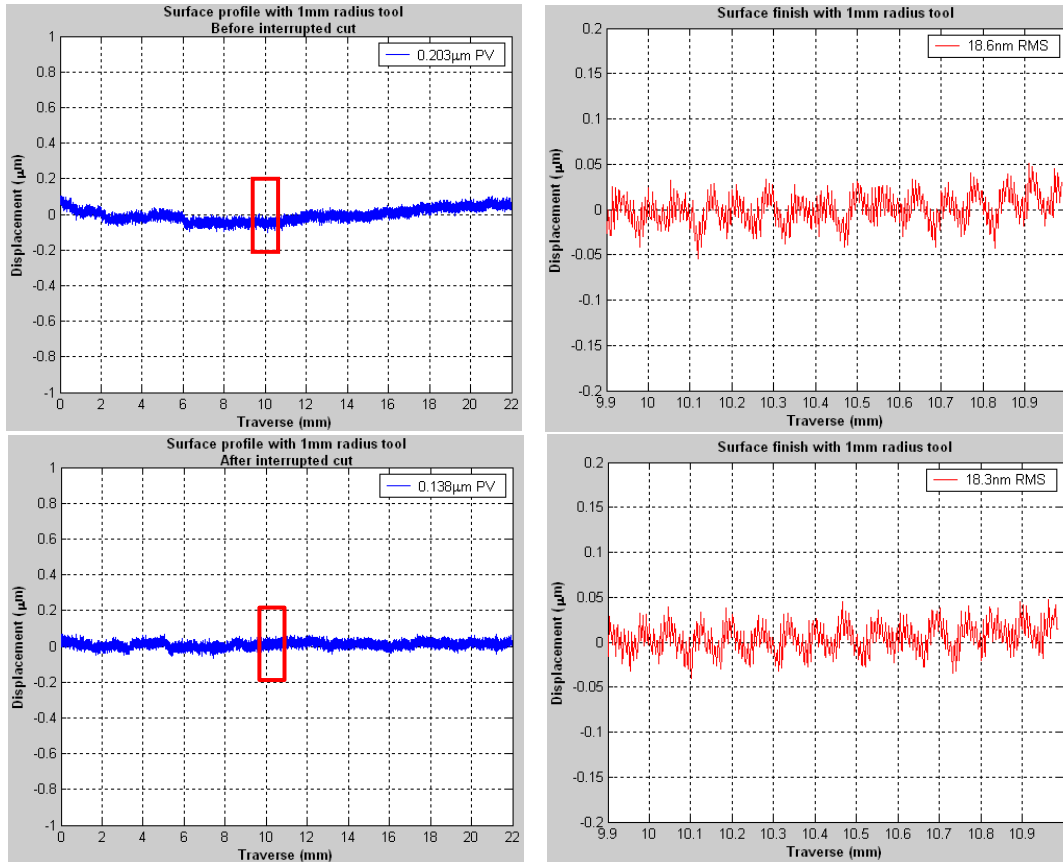


Figure 3-43. Profilometer measurements of second machined face of Ring 1 before (top) and after (bottom) interrupted cut

After the top and bottom faces of Ring 1 had been machined, the top and bottom faces of Ring 2 were machined and measured. The surface finish of side 1 was 15.2nm and side 2 was 14.3nm. As for the surface profile, side 1 measured 0.185µm while side 2 was 0.173µm. The surface finish of Ring 2 is slightly better than Ring 1 but the surface profile is comparable to Ring 1.

3.3.6.2 Preparation to machine ID and OD

The disk and spacers were taken off the vacuum chuck so Ring 1 could be re-attached easier without scratching either of the flat faces. The bolts and spherical washers were lubricated again with oil and placed inside the counter bores. 5in-lb of torque was

applied to each bolt. The entire unit was mounted onto the vacuum chuck. The lever-type electronic gage head was placed under the ring; the disk was tapped when the gage read “low” spots. Figure 3-44 displays the lever-type electronic gage measurement of the OD of the centered ring for one rotation of the spindle. The figure magnifies the 3 lobes with a maximum PV of $30\mu\text{m}$. The mean of the 3 lobes is approximately $1.34\mu\text{m}$ which corresponds to the ring’s centering position on the chuck.

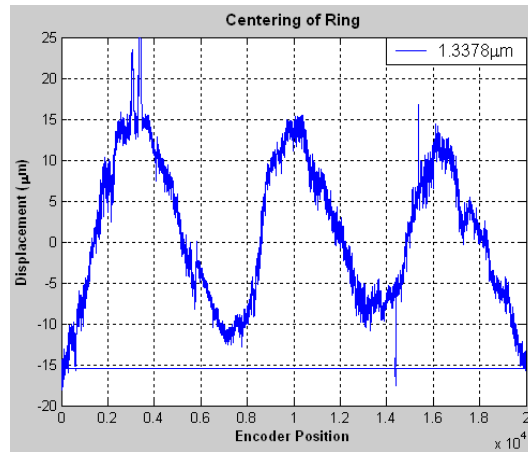


Figure 3-44. Lever-type electronic gage capture of ring centering

The micro height adjuster with the mounting block and FTS was bolted to the x-axis of the DTM. Before the bolts that affix the FTS to the mounting block were tightened, the tilt of the servo in the x-axis had to be checked. The base of the lever-type electronic gage was set on top of the spindle and the gage head rested on top of the FTS. Movement of the x-axis caused the probe to traverse the top of the FTS. The bolts were gradually tightened as the servo was made level. After successive traces over the FTS and minor adjustments, the displacement over 27mm is $12\mu\text{m}$ (0.025° by small angle approximation). It produces an insignificant, sub-nanometer cosine error in tool position during wave fabrication.

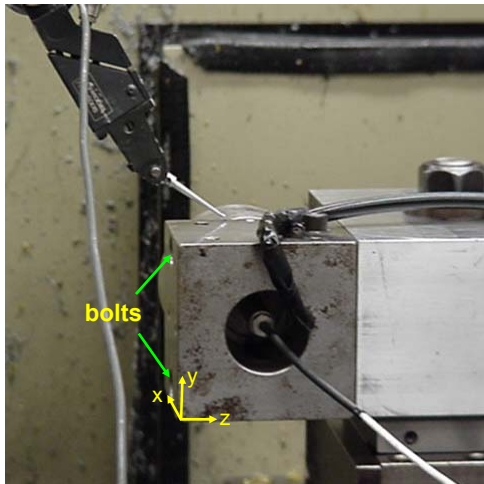


Figure 3-45. Lever-type electronic gage measuring tilt of the FTS

The next step was to verify the height of the tool. The micro height adjuster was lowered to its lowest position and a set of gage blocks were set up to equal 6". The lever-type electronic gage measured the relative height between the tool and the gage blocks. The rake face of the tool was 250 μm above the gage blocks. This is equivalent to 6.00984" above the x-axis surface. Since the nominal height of center is 6.00874", the tool is about 0.0011" (28 μm) above center. The micro height adjuster was at the bottom of its range so the tool was not moved down. On the ID, this may cause a theoretical error of 0.105 μm in the 5 μm amplitude of the wave; on the OD, the error may be 0.079 μm . Figure 3-46 demonstrates the tool height measurement.



Figure 3-46. Measurement of tool height

The ID of Ring 1 was to be cut first. Before touch-off, the mounting block holding the FTS was rotated, and the x-axis was moved as needed to position the servo inside the ring. The lever-type electronic gage head was shifted to the side of the spindle to measure the side of the mounting block. The mounting block was positioned to ensure the tool was perpendicular to the ID surface. Over a traverse of 35mm, the gage head displaced 1 μ m.

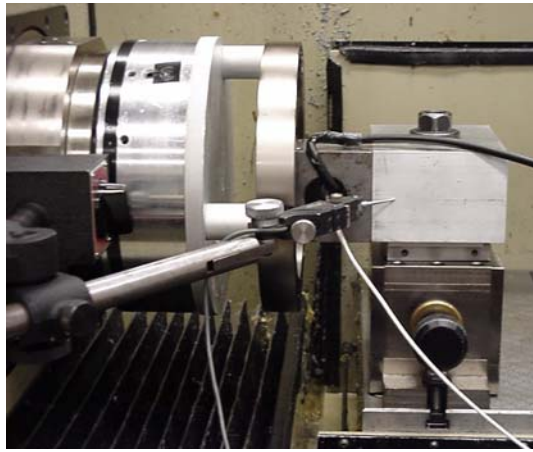


Figure 3-47. Measurement of the squareness of the tool to the ID

The cap gage in the back of the FTS has a range of 20 μ m. Since the swept sine wave measures 10 μ m peak-to-valley, the cap gage had to be positioned in the middle of its range. The cap gage was adjusted until its mid-range was found; the set screw was tightened to hold it in place.

3.3.6.3 Reference Command Generation

An algorithm to linearly interpolate between counts of the encoder (see `closed_ring_cut_interp.mdl` in Section 7.6) was developed to increase the number of counts per wave and the shortest wavelength was lengthened (from 0.32 to 0.51mm) to decrease the maximum operating frequency of the FTS. A lower operational frequency causes improved performance by the FTS (see Figure 3-27 in Section 3.3.1). The

interpolation algorithm uses a counter to monitor how long the encoder remains on the same count. However, due to the slight difference in time between encoder counts, the number of interpolated points between each count varies. Based on the sampling rate of the model, the encoder may remain on the same count from 1 to 6 cycles through the model; the model assumes a maximum of 4 cycles between encoder counts. At each fraction of 4, a new displacement value is assigned to the servo. If the model cycles through more than 4 times before the encoder count changes, the successive counts' value is assigned earlier and remains until the cycles start over upon recording the next count.

3.3.6.4 Machining the ID

The ID was surfaced using an altered closed loop control version of the swept sine wave Simulink model (see faceoff.mdl in Section 7.6). (The PZT gain was changed to 1.365 from 1.5942 due to the smaller percentage of the PZT range used as shown in Figure 3-25; 20,000 values of -0.006mm were imported to the look-up table.) Touch-off was initiated on the ID with a constant 1 μ m input to the FTS. At high spindle speeds, open loop speed control of the DTM is sufficient due to a lower percentage of speed error (see Section 7.3 for further discussion of speed control); the spindle rotated clockwise at 500RPM. A total of 65 μ m was removed from the ID.

The swept sine wave will be machined onto a raised portion on the ID and OD to combat the effect of probe shanking. If the diameter of the probe stylus is not sufficiently smaller than the probe tip or if the stylus is tilted, the stylus will contact the surface without the tip measuring the wave in the horizontal orientation. Thus, the bottom of the wave was changed to 10 μ m higher than the outside portions on the ring ID and OD to alleviate the shanking problem.

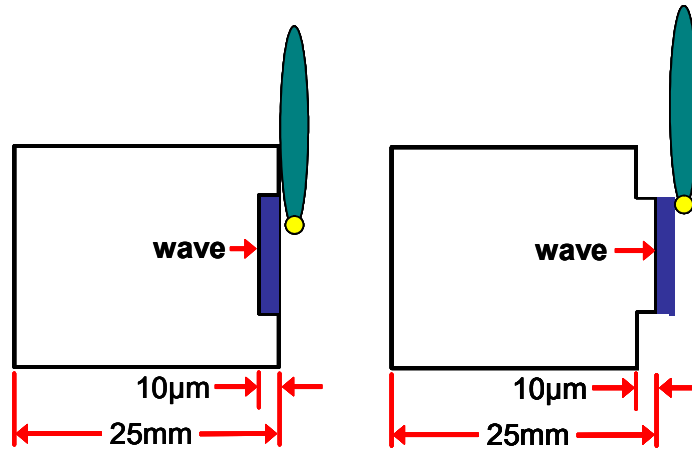


Figure 3-48. Cross section view of probe measurement of wave; left demonstrates shanking problem with stylus

Touch-off was performed again to find the inside lower edge of the ring on the ID; previously, the surface relative to the x-axis was found and an arbitrary position from the edge was set for the z-axis during face off. The x-axis was moved into the surface $1\mu\text{m}$ from the edge. The spindle rotated slowly as the z-axis was moved towards the tool; when a chip was found, the relative z-axis position was set. The tool fed along the z-axis 6.25mm , moved out of and across the surface, stepped back in at 18.25mm and finished machining across to form a 12mm raised section in the middle of the ID width. The raised section on the ID is $20\mu\text{m}$ and was machined using three passes with depths of cut of $10\mu\text{m}$, $9\mu\text{m}$, and $1\mu\text{m}$ due to the hardness of the nickel and to achieve a better surface finish with a $1\mu\text{m}$ finishing pass.

After the raised section was created, the swept sine wave was machined into the section. The DTM spindle rotated 20RPM clockwise with closed loop speed control provided by DSPACE. Two machining passes ($9\mu\text{m}$ and $1\mu\text{m}$) were used with the $1\mu\text{m}$ depth of cut final pass intended to improve the surface finish of the wave. A cap gage measurement

of tool displacement of the FTS demonstrates the slight difference in the shape of the wave from one rotation to the next due to the interpolation. Figure 3-49 shows three measurements during the wave cut; only when expanding a single wave is the difference in the interpolated waves apparent. The effect of this difference will be more apparent with smaller radius probes during measurement of the ring, but the overall shape of each wave has improved by the reduction of the large steps in displacement as the wavelength gets shorter.

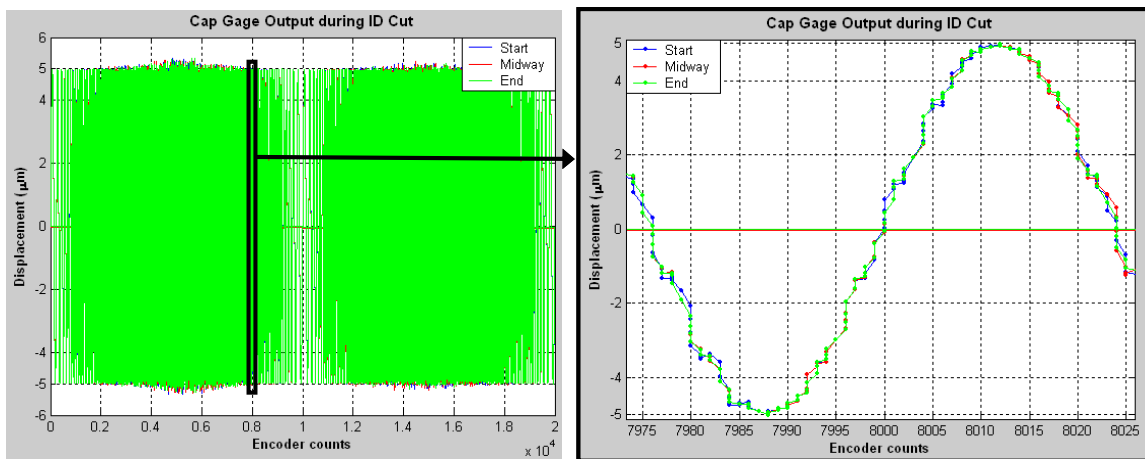


Figure 3-49. Cap gage captures of the swept sine wave cut on the ID of Ring 1

3.3.6.5 Machining the OD

After the swept sine wave was cut on the ID of Ring 1, the mounting block holding the FTS was rotated to prevent the FTS from hitting the ring as the x-axis was used to move the setup to the outside. The mounting block was rotated back into position and the lever-type electronic gage verified its perpendicular relationship to the surface; over a trace of 35mm, the gage head displaced $\sim 0.2\mu\text{m}$. The centering of the ring was also checked with the gage head on the OD; the mean of the three lobes indicated $0.5\mu\text{m}$ off-center.

The OD surface was found via touch-off and the x-axis was moved 10 μ m further away from the surface. The FTS moved closer to the surface with small increments during each machining pass until an observable cut was made on the OD. Each successive depth of cut was 5 μ m, and a total of 50 μ m of material was removed from the OD. Following the surfacing of the OD, the edge of the ring was found as it had been with the ID with the relative z-axis position set. A 20 μ m raised section was formed on the OD using three machining passes with depths of cut of 10 μ m, 9 μ m, and 1 μ m due to the hardness of the nickel and to achieve a better surface finish with a 1 μ m finishing pass.

The swept sine wave was machined onto the raised section at a speed controlled 20RPM in two machining passes (9 μ m and 1 μ m); the final pass used 1 μ m for its depth of cut to improve the surface finish of the wave. The cap gage signal was monitored as it had been with the ID. Figure 3-50 exhibits three measurements captured; the interpolation effect is again noticeable when focusing on a single wave. The error in the amplitude at the highest frequencies on the OD is approximately 10% whereas it was ~5% on the ID because of the higher operational frequency of the FTS on the OD.

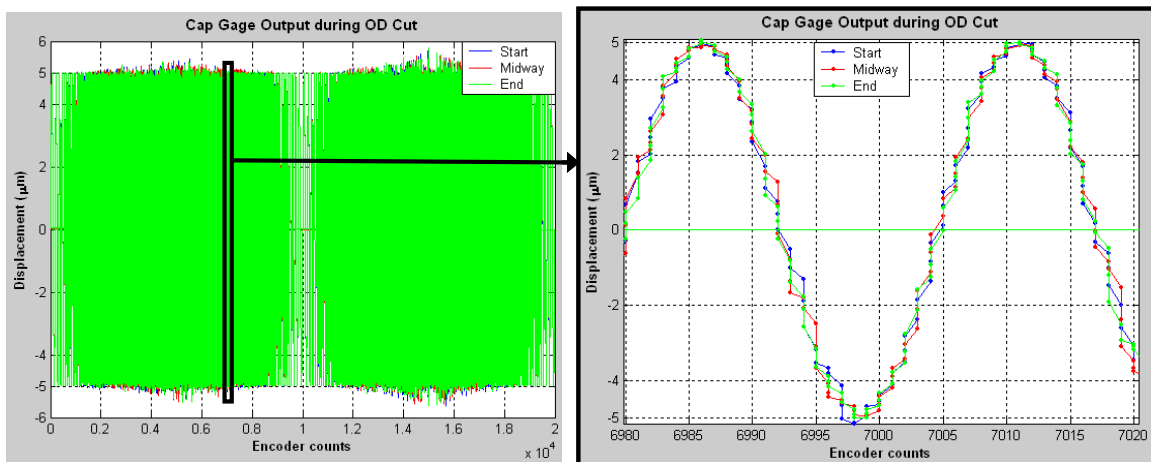


Figure 3-50. Cap gage captures of the swept sine wave cut on the OD of Ring 1

3.3.6.6 Angular Fiducial

To provide a reference position of the swept sine wave on the part, a fiducial was added to the OD. The fiducial is a 4mm wide, cosine wave with a theoretical 1.82mm wavelength based on a 10 μ m depth of cut. The generated cosine wave had an amplitude of 8 μ m (PV = 16 μ m) to fit within the range of the FTS (18 μ m). When the fiducial was cut, the tool was moved away from the surface 6 μ m to achieve the 10 μ m depth.

The cap gage signal was captured along with the expected fiducial values assigned to each encoder count. The sampling rate of the Simulink model (see `closed_ring_cut_fiducial.mdl` in Section 7.6) was 35kHz. With this sampling rate and a spindle speed of 200RPM, 85% of the generated points were used during machining because all the encoder counts were not observed. In Figure 3-51, the symmetric signal is the desired fiducial while the non-symmetric signal is the actual movement of the FTS. The double line of the non-symmetric signal is attributed to 1.5 revolutions of data collected. The difference between the widths may be attributed to delay in the controller command at the start of the wave and to the range and acceleration limits of the FTS.

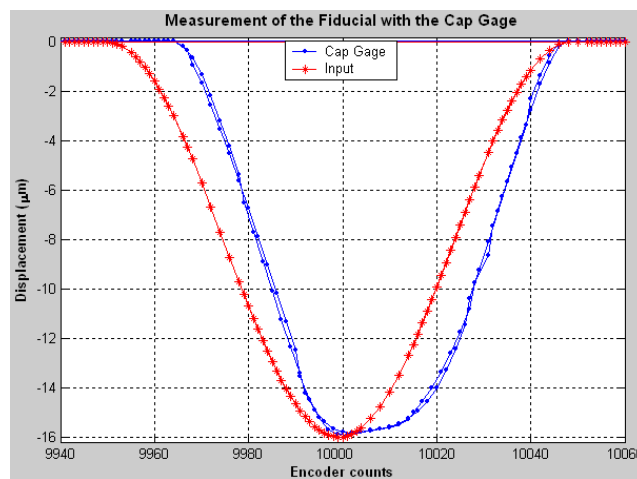


Figure 3-51. Comparison of expected and actual fiducial machined on the surface

3.3.7 Measurement of Top and Bottom Surfaces of Ring 1

The top and bottom flat surfaces of the ring were measured with the GPI interferometer before and after machining of the swept sine wave to check for any distortion of the ring. Figure 3-52 defines the counter bore positions where the measurements were taken on each side of the ring. “CB” stands for counter bore. Side 1 is the surface that began with excess Ni near two of the counter bores (CB1 and CB2) before machining; Side 2 is the uniformly Ni-plated surface.

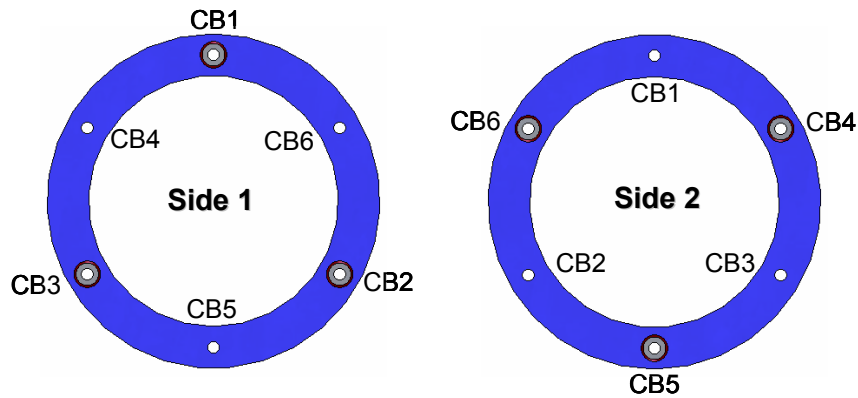


Figure 3-52. Definition of counter bore positions on the ring

Figure 3-53 is representative of surface measurements near the counter bores of Side 1 before machining of the ID and the OD. Figure 3-54 is a measurement taken across from CB1 at one of the small through holes (CB5).

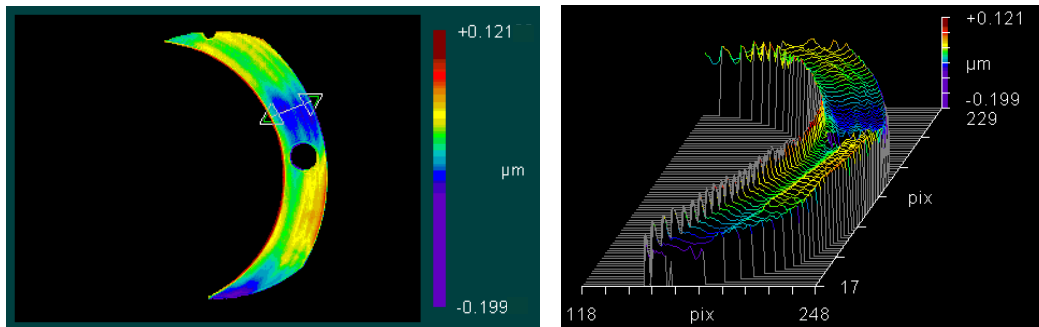


Figure 3-53. Surface map of the ring near CB1 with chips at edge

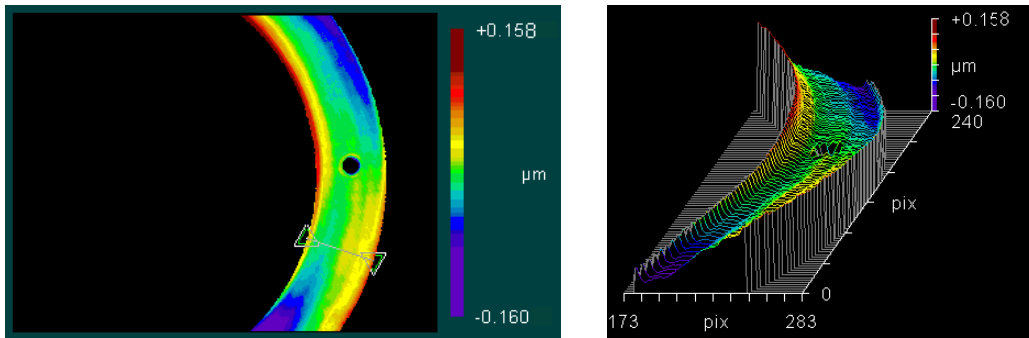


Figure 3-54. Surface map of the ring near one of the through holes (Side 1)

The surface profile measurements are intended to check the uniformity of the datum surfaces of the ring. The interferometric images display approximately 130° of the entire ring. The instrument measures the peak-to-valley (PV) of the surface. A representative cross section of the entire image was also analyzed. Table 3-4 provides a summary of the measurements on Side 1. Each measurement is relatively similar to the others with the exception of CB2 which contributes to the higher standard deviations.

Table 3-4. Summary of interferometer surface measurements of Side 1

<i>Counter bore</i>	<i>Overall PV</i>	<i>Cross section PV</i>
<i>1</i>	0.320µm	0.079µm
<i>2</i>	0.458µm	0.136µm
<i>3</i>	0.375µm	0.075µm
<i>Small hole (CB5)</i>	0.318µm	0.088µm
<i>Average</i>	0.368µm	0.095µm
<i>Standard Deviation</i>	0.066µm	0.028µm

The ring was flipped over to access Side 2. Similar measurements were taken at each counter bore, and another measurement was taken near the through hole of CB2. Figure 3-55 is an image of CB5 that corresponds to the through hole on Side 1 that was previously measured to determine the influence of mounting during fabrication. Figure

3-56 measures the through hole opposite CB2 on Side 1 to attain another example of the effect.

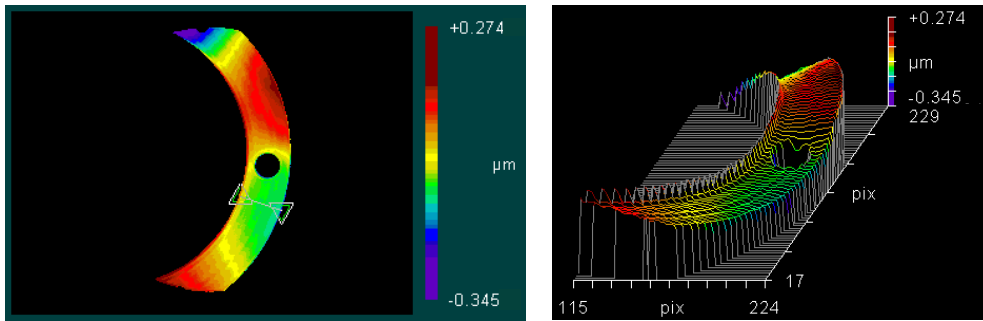


Figure 3-55. Surface map of CB5 on Side 2 opposite through hole on Side 1

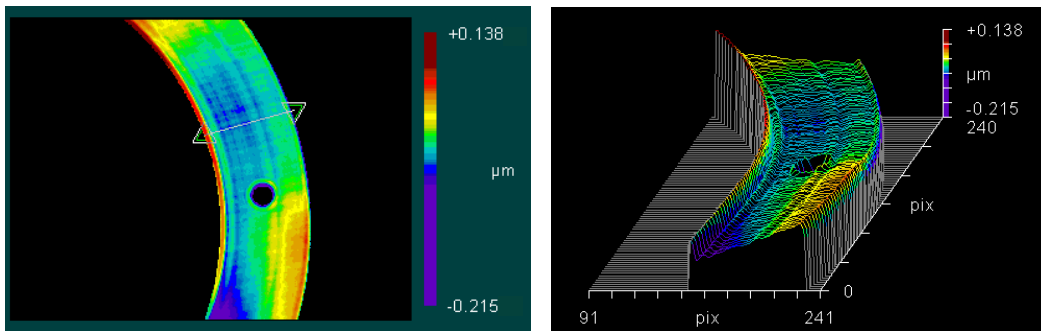


Figure 3-56. Surface map of through hole associated with CB2

Table 3-5 provides a summary of the measurements taken on Side 2 of the ring gauge before final fabrication of the ID and the OD. It also indicates that the surface profile on the side opposite a counter bore is an improvement. On Side1, CB2 had an overall PV of $0.458\mu\text{m}$ while CB5 had an overall PV of $0.318\mu\text{m}$.

Table 3-5. Summary of interferometer surface measurements of Side 2

<i>Counter bore</i>	<i>Overall PV</i>	<i>Cross section PV</i>
4	$0.466\mu\text{m}$	$0.151\mu\text{m}$
5	$0.620\mu\text{m}$	$0.182\mu\text{m}$
6	$0.494\mu\text{m}$	$0.146\mu\text{m}$
<i>Small hole (CB2)</i>	$0.354\mu\text{m}$	$0.125\mu\text{m}$
<i>Average</i>	$0.484\mu\text{m}$	$0.151\mu\text{m}$
<i>Standard Deviation</i>	$0.109\mu\text{m}$	$0.024\mu\text{m}$

The higher PV values near the counter bores may be an indication that the surface is being elastically deformed during mounting and machined flat so that when the mounting force is released, the surface returns to its original state. The measurements near the through holes opposite the counter bores show smaller PV values to substantiate the theory that the surface resting on the spacers is not being deformed nearly as much as the counter bore surface (refer to Figure 3-34 for a cross section of the counter bore).

The ring was re-mounted with Side 2 resting on the spacers in preparation for final machining of the ID and the OD with the swept sine wave. Thus, torque was applied to the bolts in the counter bores on Side 1. After the final fabrication and before the ring was taken off the spacers, the top surface (Side 1) was again measured with the interferometer. Figure 3-57 is a profile of CB2 with 2 cross sections (small lines) analyzed.

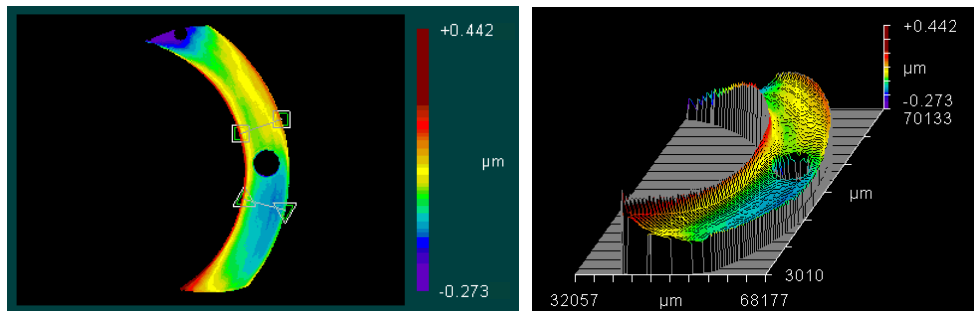


Figure 3-57. Surface map of counter bore 2 with ring attached to spacers

Table 3-6. Side 1 surface measurements with ring attached to disk and spacers

<i>Counter bore</i>	<i>Overall PV</i>	<i>Cross section PV</i>
<i>1</i>	0.540µm	0.128µm
<i>2</i>	0.716µm	0.172µm
<i>3</i>	0.594µm	0.170µm
<i>Small hole (CB5)</i>	0.619µm	0.228µm
<i>Average</i>	0.617µm	0.175µm
<i>Standard Deviation</i>	0.074µm	0.041µm

As before, Table 3-6 indicates the PV value of CB2 is larger than the others. The ring was taken off the spacers, and Side 1 was measured again. Figure 3-58 shows that the outer edges of the ring are higher than the rest of the ring. The same is true for each measurement around the ring because the ID and the OD were machined after the top and bottom of the ring.

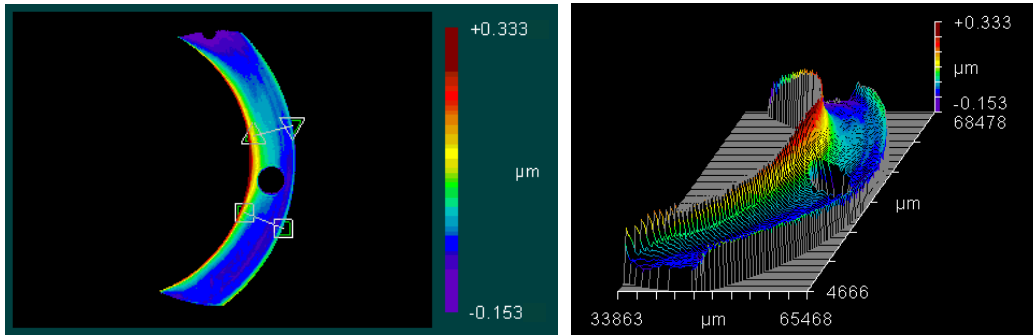


Figure 3-58. Surface map of CB2 with ring taken off mount

Table 3-7. Side 1 surface measurements with ring taken off mount

<i>Counter bore</i>	<i>Overall PV</i>	<i>Cross section PV</i>
<i>1</i>	0.483 μm	0.119 μm
<i>2</i>	0.487 μm	0.259 μm
<i>3</i>	0.587 μm	0.355 μm
<i>Small hole (CB5)</i>	0.627 μm	0.148 μm
<i>Average</i>	0.546 μm	0.220 μm
<i>Standard Deviation</i>	0.072 μm	0.108 μm

Table 3-7 provides the measurement values after the ring was removed from its mount. The average PV before machining of the ID and the OD was 0.368 μm ; after machining, it is 0.546 μm . The increase is due to the higher outer edges, particularly on the ID. The ring was turned over to measure Side 2. Figure 3-59 is a representative measurement of Side 2; it also exhibits higher edges as is consistent with Side 1. The overall PV is 0.522 μm

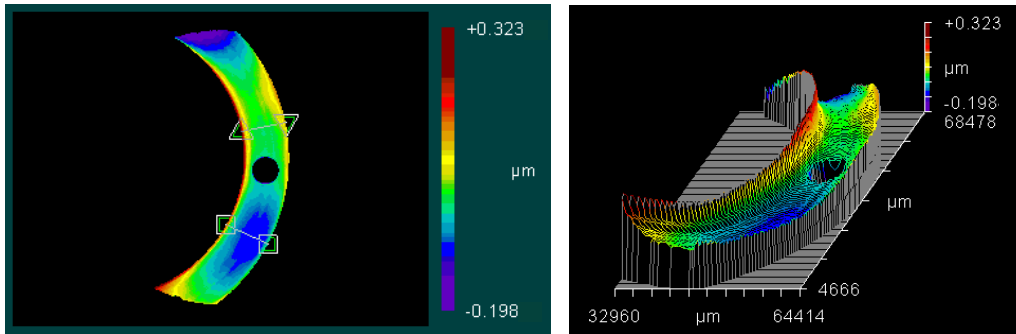


Figure 3-59. Surface map of CB5 on Side 2

The data in Table 3-8 indicates that the average PV value is within 15nm of Side 1 and with less variation over the surface. The increased uniformity of the surface is indicative of how the ring was mounted during the machining of the ID and the OD. Side 2 was resting on the spacers and not subjected to the bolt load as was Side 1.

Table 3-8. Side 2 surface measurements with ring taken off mount

<i>Counter bore</i>	<i>Overall PV</i>	<i>Cross section PV</i>
4	0.578μm	0.262μm
5	0.522μm	0.296μm
6	0.554μm	0.232μm
Small hole (CB2)	0.477μm	0.146μm
Average	0.533μm	0.234μm
Standard Deviation	0.047μm	0.064μm

Additional measurements were taken on Side 2 to look more closely at the deformation around the counter bores and the through holes. The compilation of PV values, shown in Table 3-9, varies more than the previous measurements but are lower with a smaller area captured. Figure 3-60 displays a surface map of CB6 along with a closer view of the counter bore. The expanded view demonstrates the small amount of elastic deformation around the outside of the counter bore.

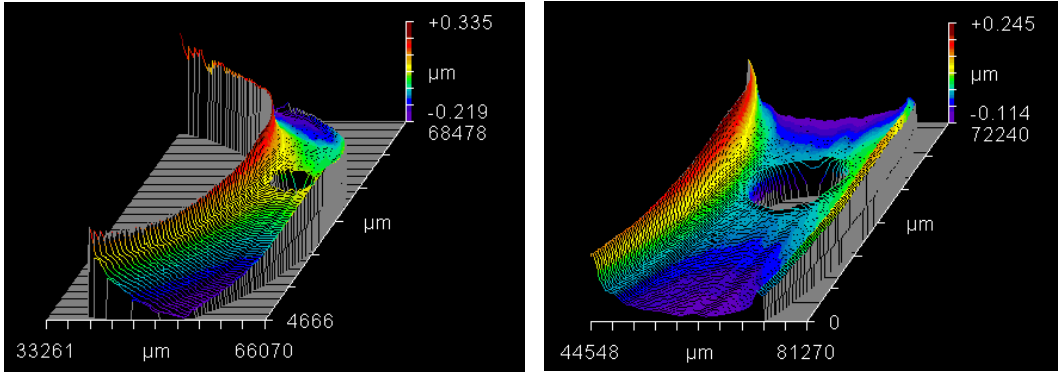


Figure 3-60. Surface map of CB6 on left and zoomed in on right

Table 3-9. Zoomed in sections on Side 2; 2 counter bores, 2 small holes

<i>Counter bore</i>	<i>Overall PV</i>	<i>Cross section PV</i>
<i>4 – zoomed in</i>	0.425 μm	0.262 μm
<i>6 – zoomed in</i>	0.359 μm	0.296 μm
<i>1 – small hole</i>	0.397 μm	0.232 μm
<i>2 – small hole</i>	0.258 μm	0.146 μm
<i>Average</i>	0.360 μm	0.234 μm
<i>Standard Deviation</i>	0.188 μm	0.064 μm

The consistent measurements with high spots at the outer edges prompted measurements with the NewView interferometer. Figure 3-61 is an image of the OD on Side 2 while Figure 3-62 is an image near the ID on Side 1.

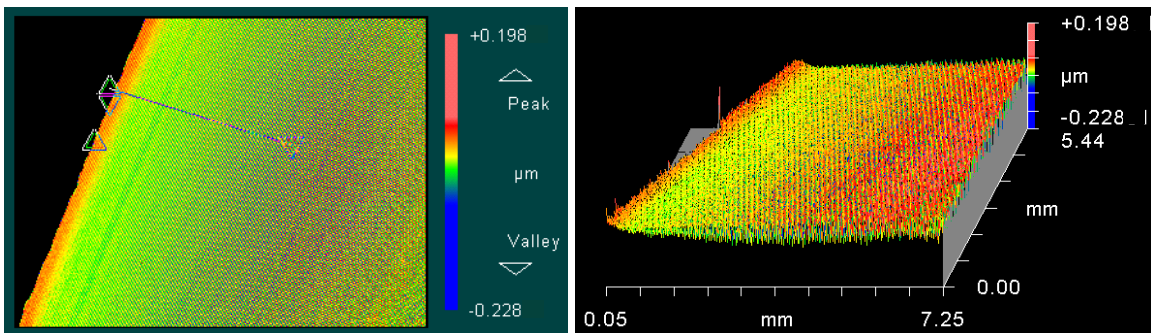


Figure 3-61. OD of the ring on Side 2 as measured by the NewView

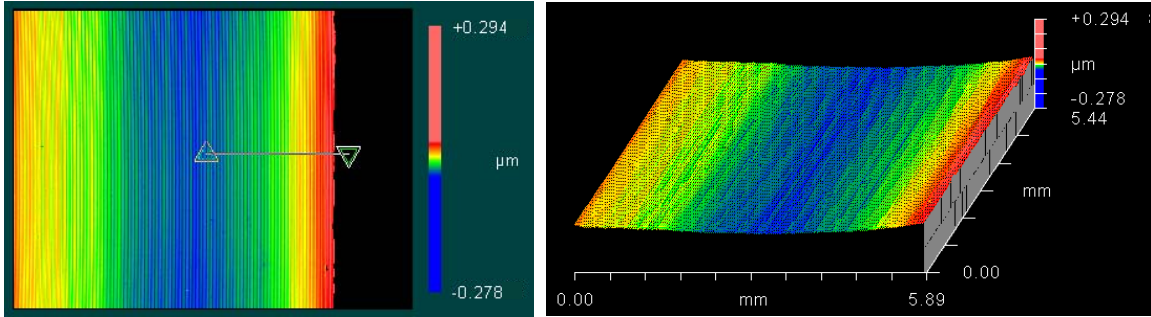


Figure 3-62. ID of the ring on Side 1 as measured by the NewView

The outer edge near the OD of Figure 3-61 is approximately 50nm higher than the rest of Side 2 while the outer edge near the ID of Figure 3-62 is approximately 60nm higher than the rest of the surface on Side 1. The measurements with the GPI indicate a marginally larger displacement around the edges, but the images were taken near the counter bores which have the interrupted pass across the width and the larger deformation. The sloping edges may be attributed to burrs created during the machining process. Disregarding the edges, the surface finish is 37nm RMS as shown in Figure 3-63. The 3D plot displays the tool passes with a damaged 1mm radius tool on the surface of Ring 1.

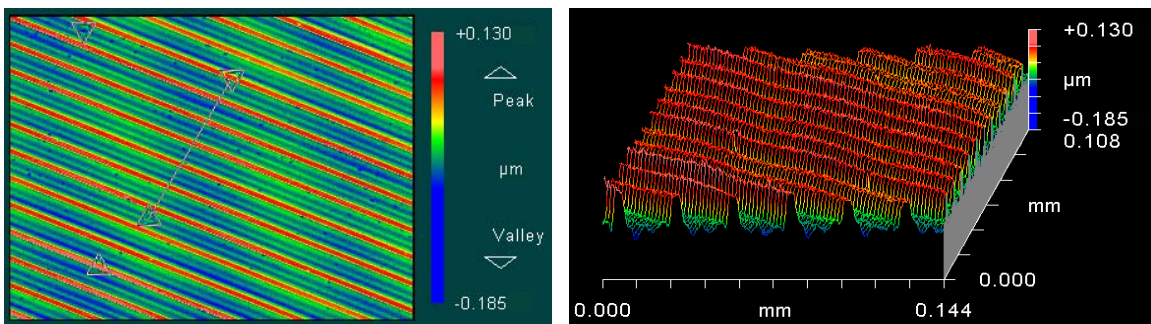


Figure 3-63. Surface finish near through hole of CB5 on Side 1

The average PV value of Side 1 before ID/OD fabrication was 0.368 μm and afterwards was 0.546 μm . The top surface under the bolts is slightly deformed but is still an improvement over the previous mounting scheme. The double counter bores (old) created 38arcsec of figure error while the 60° rotated counter bores (new) create only

4.4arcsec of figure error on the surface. Also, from Table 3-7, the overall surface is flat (standard deviation is 72nm) which will not affect its use as a reference surface during CMM measurement. The same is true for Side 2 (Table 3-8).

Measurements of surface finish for the flat regions on the ID and the OD were not taken with the NewView due to the vertical height of the ring for the OD as well as positioning difficulties of the objective for the ID. Therefore, the profilometer was used to take 4 – 0.5mm measurements on the ID and the OD of Ring 1.

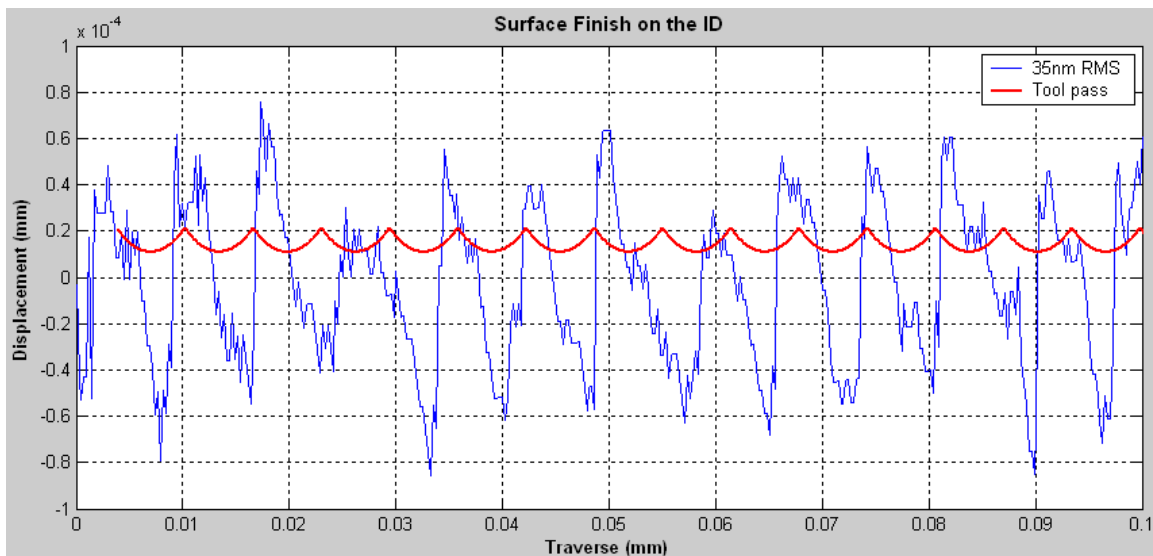


Figure 3-64. Profilometer measurement of surface finish on the ID of Ring 1

Two measurements were taken on each side of the wave at random locations on the non-wavy sections. The four total measurements identified the surface finish to be 32, 36, 38 and 35nm RMS with an average of 35nm RMS. Figure 3-64 illustrates a portion (0.1mm) of one of the measurements on the ID. The symmetrical curves represent the theoretical path of the tool during machining.

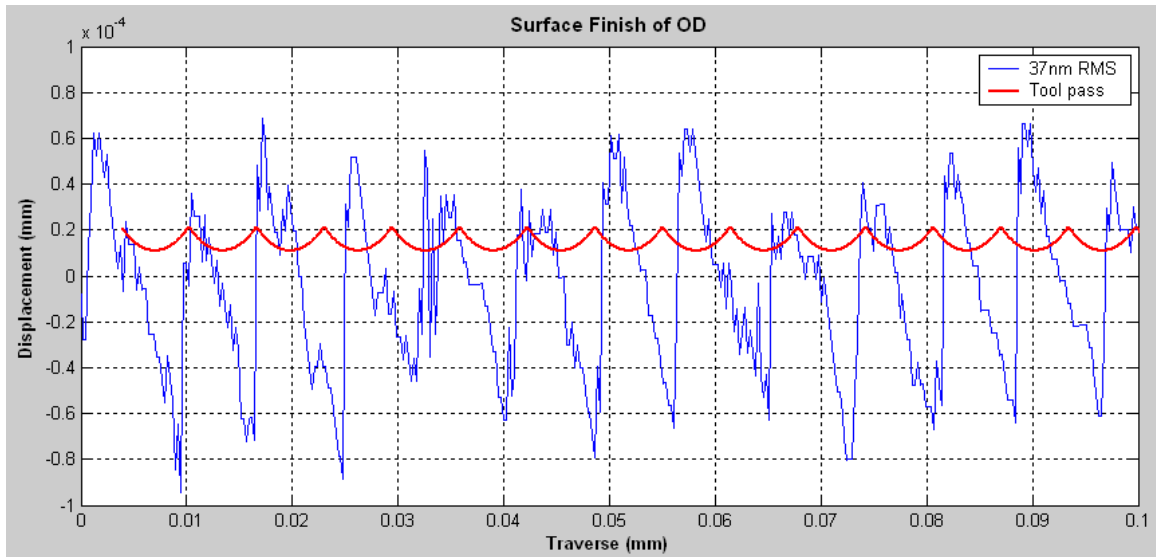


Figure 3-65. Profilometer measurement of surface finish on the OD of Ring 1

On the OD, 2 measurements were also taken at random locations on each non-wavy section. The four measurements determined the surface finish to be 30, 38, 38 and 37nm RMS with an average of 36nm RMS. Figure 3-65 represents part (0.1mm) of one of the measurements. Again, the symmetrical curves represent the theoretical path of the tool during each machining pass.

The theoretical surface finish was 3nm RMS. The actual surface finish is a factor of 10 greater than expected. One reason may be a damaged diamond tool. The large PV of about 120nm and the repeatability of each machining pass would indicate a chip in the tool. Another reason is due to the slightly inconsistent feed rate of the DTM. The commanded feed rate was 3.2mm/min; however, based on the data from Figure 3-65, the feed rate varies at rates above the desired rate when using a spindle speed of 500RPM. Each 50 μ m section of the data consists of ~6 peaks when it should exhibit 7 peaks as is shown by the theoretical tool path. The varying feed rate is a small contributing factor in comparison to the error caused by a damaged tool. Thus, the high RMS is mainly due to

tool damage but a higher feed rate coupled with additional machine error will also cause a higher than expected surface finish on the part.

3.3.8 LVDT Measurement

Following the fabrication of the swept sine wave on the ID and the OD, the wave feature and the fiducial were measured while the ring was still mounted on the DTM. The FTS was removed from the mounting block where it was replaced with a holder for the LVDT⁹. The LVDT slid into the hole of the holder and was held by a set screw. The building air was used as the supply for the air bearing. Figure 3-66 illustrates the LVDT mounting on the DTM.

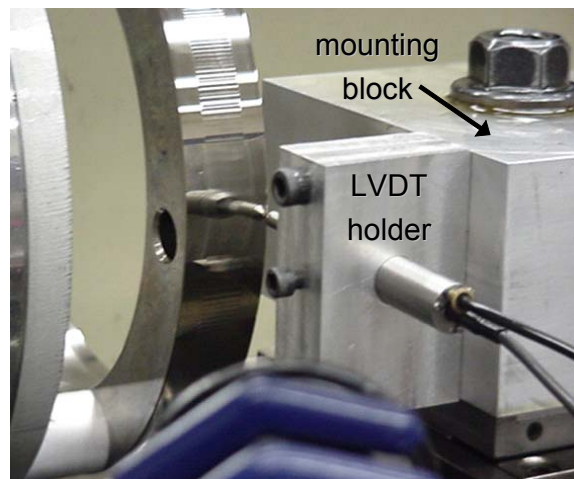


Figure 3-66. Set up for the LVDT measurement of the wave

The LVDT holder provided enough clearance so only the axes were needed to position the LVDT on the ID and the OD without having to rotate the mounting block (see Figure 3-66). By observing the height of the probe next to 6" gage blocks, the height of the probe appears to be slightly lower than the height of the center of the spindle; this will be corrected in the data analysis by shifting the measured position of the wave to align with

⁹ The LVDT used to measure the steel ring is different than the one used for the Al ring

its position at fabrication. The wave is defined by its relationship to encoder counts during fabrication and measurement. For the ID, the LVDT probe is lower by 28 counts while it is lower by 23 counts for the OD.

3.3.8.1 Calibration of LVDT

While the DTM spindle was held stationary, the LVDT was moved to the middle of its range with the probe contacting the flat surface on the OD. The x-axis was commanded to move to various positions within $\pm 12.5\mu\text{m}$. At each location, the actual position, as indicated by the axis' laser interferometer, and the LVDT output voltage were recorded. A line was fit to the data (Figure 3-67) and a conversion factor was determined ($1.201\mu\text{m}/\text{V}$).

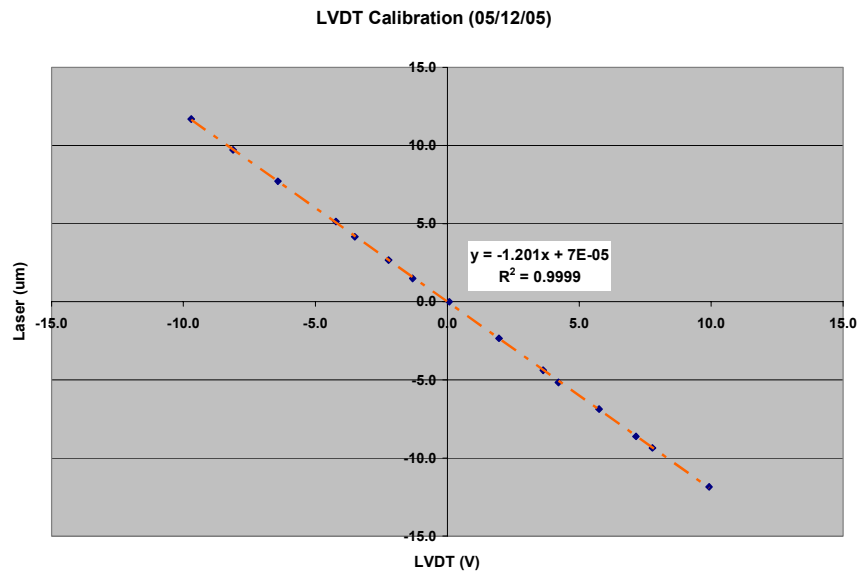


Figure 3-67. Calibration of LVDT with determined conversion factor

3.3.8.2 Swept Sine Wave Measurement

The flat section on the OD of Ring 1 was measured first to determine the ring's position on the spindle so that any off-center and out-of-round characteristic could be removed from the swept sine wave measurement. Thus, the probe was situated near the edge of

the ridge while fully on the wave. The spindle speed was controlled using dSPACE at 0.5RPM counterclockwise. Approximately 2 rotations of the spindle were captured during each measurement of the wave feature. After a measurement was taken, the probe was incremented 1mm, resulting in a total of 12 measurements taken across the OD. An additional 12 were taken across the ID along with a measurement of its flat section. Figure 3-68 demonstrates where each measurement was taken, starting from the free end of the ring and progressing towards the spacers.

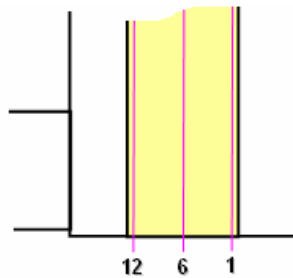


Figure 3-68. Incremental swept sine wave measurement with the LVDT

The measurement data of the flat (non-wave) section was analyzed first. A circle was fit to the data to determine the out-of-round value of the ring. The residuals are plotted in Figure 3-69 with an arbitrary radius on a polar plot to demonstrate the true shape of the OD. The OD is $0.17\mu\text{m}$ out-of-round.

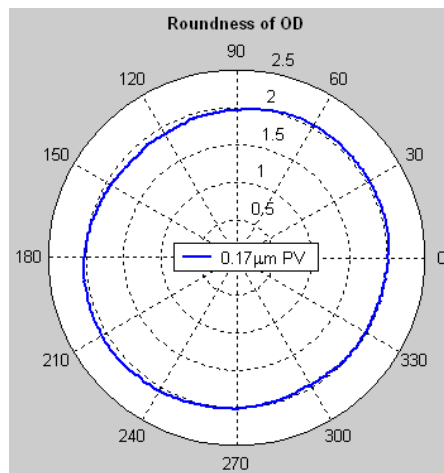


Figure 3-69. Roundness of the ring on the OD

The swept sine wave was machined onto the OD of the ring directly following the machining of the ridge on the OD. However, before the out-of-round fit can be subtracted from the wave measurements, the concentricity between the flat section and the wave section has to be verified. From observation of Figure 3-70, the flat and wave section are concentric.

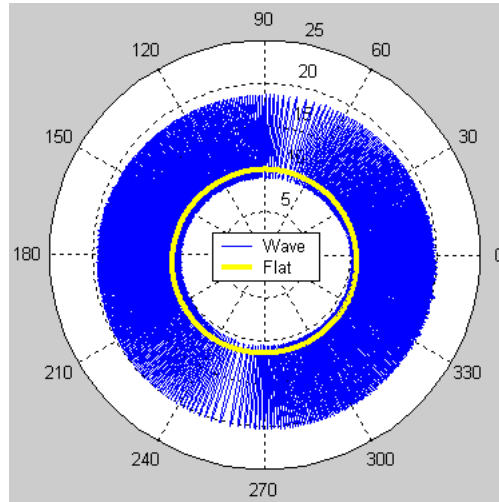


Figure 3-70. Concentricity between the flat and wave sections on the OD of Ring 1

A least squares fit was applied to the data to remove the off-center and out-of-round aspects of the ring. Figure 3-71 illustrates the original measurement around the entire ring as compared to the fitted data. The fitted data ranges from $\pm 40\text{nm}$ rather than $\pm 0.8\mu\text{m}$ as the original.

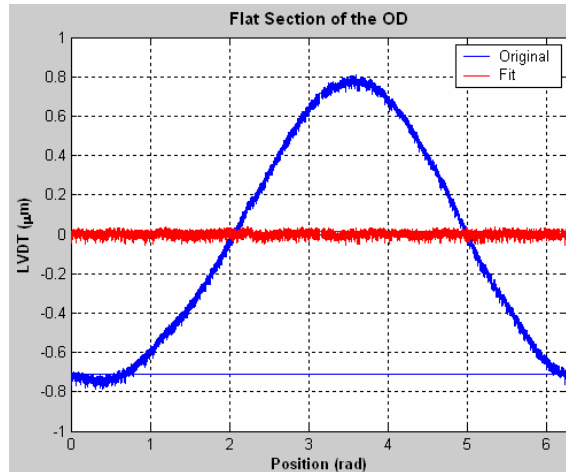


Figure 3-71. Comparison of flat section of OD before and after fit was applied

The equation for the least squares fit data was applied to each successive measurement of the wave. However, before the data was adjusted, all the measurements relating to an individual encoder count were averaged to improve the ability to analyze each wave. Recall that during fabrication, interpolation between encoder counts caused a varying number of points on the wave between each encoder count. The difference in spindle speeds during fabrication and during measurement of the wave adds complexity to matching the interpolated counts. To simplify the analysis, the swept sine wave was measured using the absolute number of counts. Due to the sampling rate of the model and fewer encoder counts, there are multiple measurements at each count; the multiple data points are averaged. Figure 3-72 compares the difference between the averaged and the raw measurement data with an enlarged section of the wave.

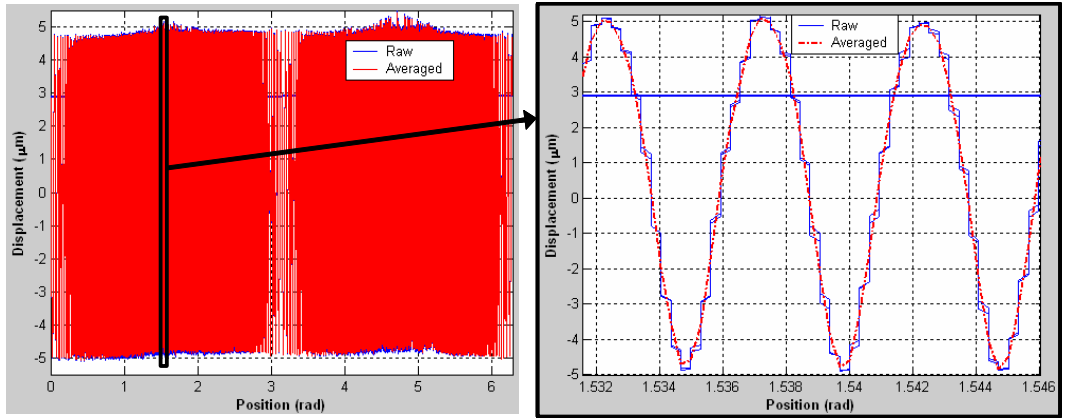


Figure 3-72. Verification of wave with averaged data

All 12 measurements on the OD were averaged to one data point at each encoder count (20,000 total). After the averaging, the least squares fit of the flat section was applied to the data sets. To compensate for the difference in LVDT height from the height of the tool during fabrication, each data set was shifted by 23 counts to cause the longest wavelength to begin at zero. The 23 counts translates to a distance of 0.734mm or 0.0289” below the tool height. Lastly, the mean of each data set was removed from the individual measurements and 0.3µm was added to each to center the wave around zero.

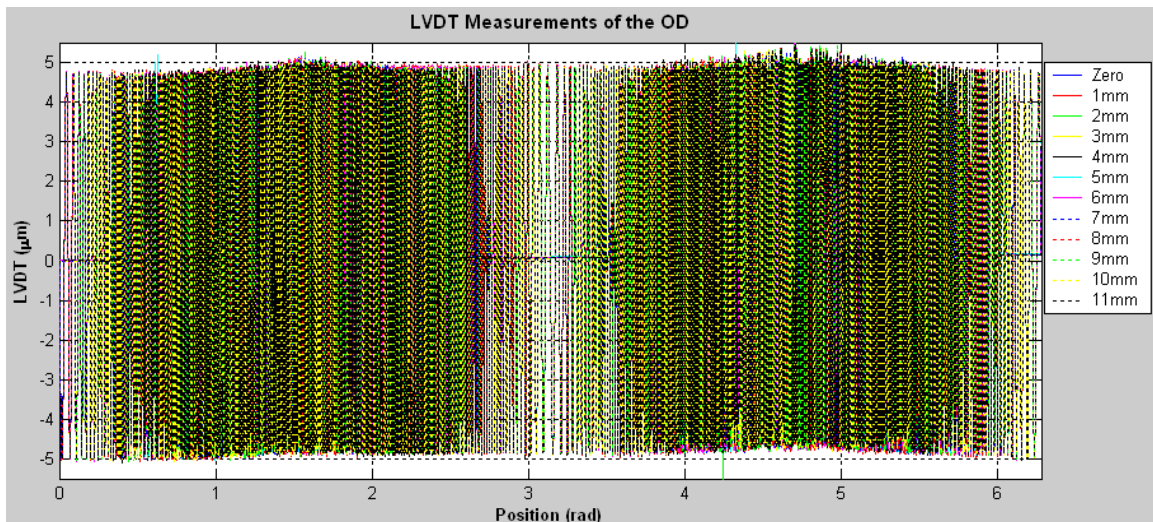


Figure 3-73. All 12 measurements of the wave on the OD of Ring 1

Figure 3-73 shows all 12 measurements. Each measurement was put into an array and an additional average of all 12 measurements was taken. This average was subtracted from each measurement to determine the deviation across the width of the wave.

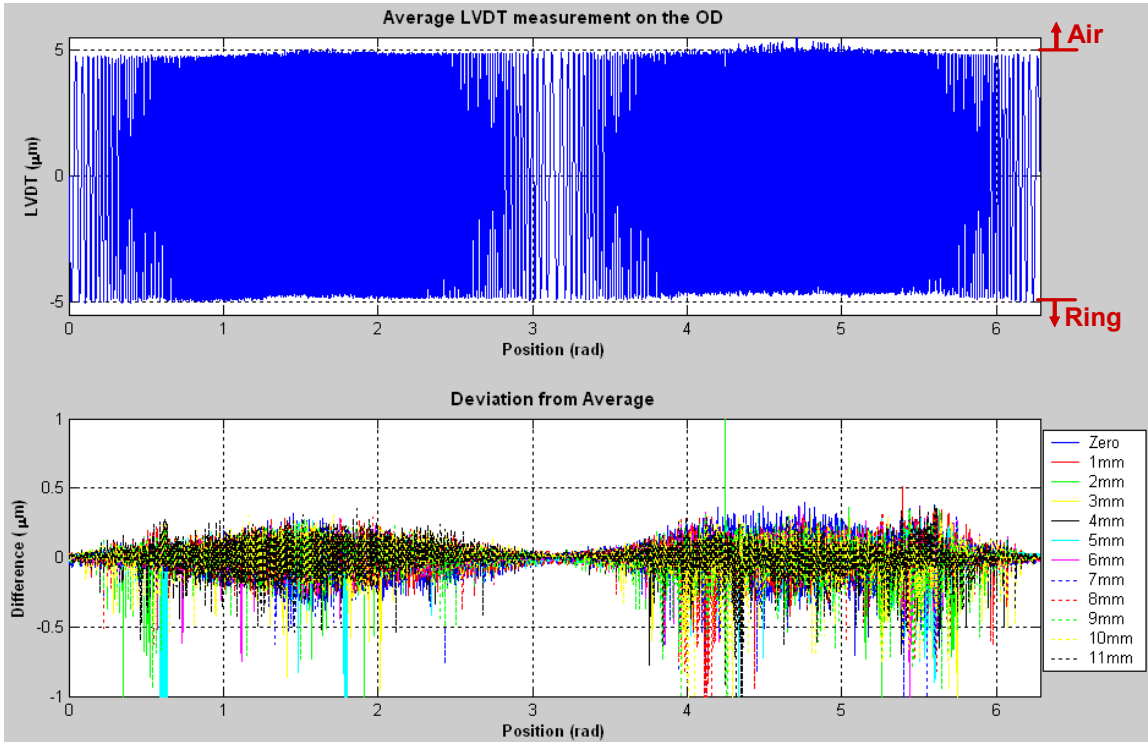


Figure 3-74. Average of measurements along with wave deviation on the OD of Ring 1

Figure 3-74 displays the average measurement in the top subplot and the deviation of each individual measurement from the average in the bottom subplot. The deviation may be attributed to the interpolation of the encoder counts and to possible residual acetone, oil, or chips left on the surface after cleaning. The ring was cleaned with acetone after fabrication. Based on visual inspection, the ring appeared to be clean but any small particle left on the surface will affect the displacement of the LVDT probe. The median difference ranges from less than 1nm to 8nm along the 12 data sets.

Table 3-10. Summary of statistics for all OD measurements (units μm) based on the individual errors from the average measurement value

<i>STAT</i>	<i>1</i>	<i>2</i>	<i>3</i>	<i>4</i>	<i>5</i>	<i>6</i>	<i>7</i>	<i>8</i>	<i>9</i>	<i>10</i>	<i>11</i>	<i>12</i>
Median	0.003	-0.004	0.000	0.003	-0.000	0.008	-0.003	0.004	0.001	0.006	0.006	0.002
Min	-0.79	-0.88	-1.38	-1.18	-0.89	-2.01	-1.14	-1.22	-1.41	-1.36	-1.14	-1.19
Max	0.45	0.51	9.67	0.31	0.28	0.30	0.36	0.31	0.35	0.38	0.31	0.37
Range	1.24	1.39	11.05	1.49	1.17	2.31	1.50	1.53	1.76	1.74	1.46	1.56
St Dev	0.088	0.068	0.165	0.064	0.054	0.102	0.061	0.070	0.081	0.080	0.083	0.082
IQR	0.092	0.065	0.044	0.045	0.040	0.042	0.049	0.043	0.062	0.050	0.059	0.066

Table 3-10 displays some common statistics. IQR refers to the interquartile range. It is a statistical measurement of the difference between the 75th and the 25th percentiles; thus, any data outside these percentiles will not affect the estimate. By ignoring the outliers in the data, the IQR is more representative than the standard deviation as an estimate of the spread of the body of the data. The maximum IQR is 92nm; this value will be used as part of the uncertainty budget for the assessment of a measurement taken from any position along the width of the wave.

After the measurement of the wave on the OD, the LVDT probe was moved to the ID. The flat section was measured first, followed by 12 measurements along the width of the swept sine wave with 1mm increments between each. Figure 3-75 demonstrates the shape of the ID on the flat section. It measures 0.35 μm PV or 2 times the error on the OD.

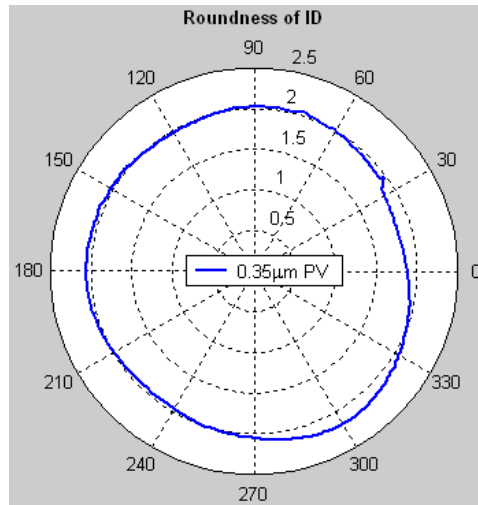


Figure 3-75. Roundness of the ring on the ID of Ring 1

The concentricity of the flat section and wave section on the ID of Ring 1 is also determined. Figure 3-76 demonstrates the shape of the flat section as compared to the mean shape of the wave. Both sections are concentric to each other.

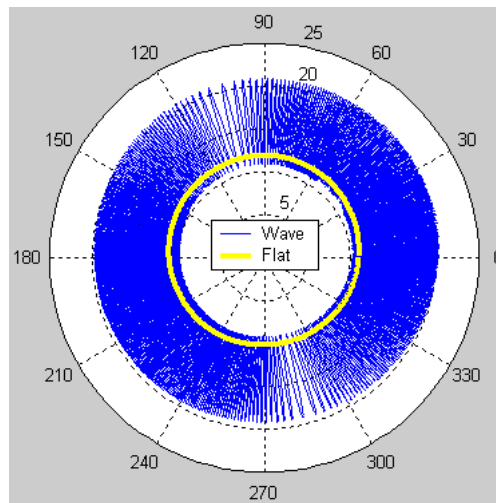


Figure 3-76. Concentricity between the flat and wave sections on the ID

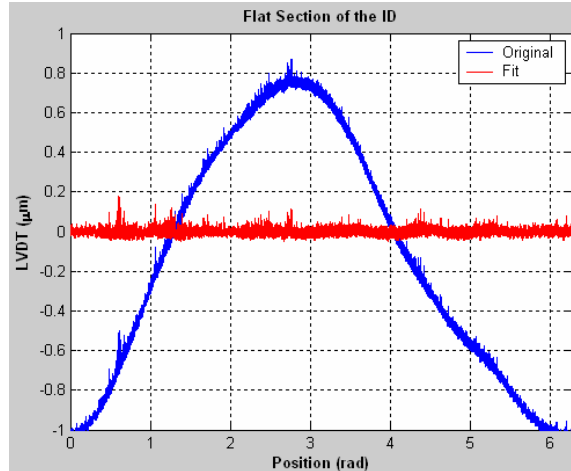


Figure 3-77. Comparison of flat section of ID before and after fit was applied

Figure 3-77 shows the adjustment for the off-center and out-of-round disposition of the ring on the spindle. The fitted data ranges from $\pm 40\text{nm}$, excluding the outliers, rather than $\pm 0.9\mu\text{m}$ as the original. As with the OD, a set of 12 measurements on the ID were measured and averaged to one data point at each encoder count (20,000 total). After the averaging, the least squares fit of the flat section was applied to the data sets. To compensate for the difference in probe height and the height of the tool, each data set was shifted by 28 counts to cause the longest wavelength to begin at zero. The 28 counts translates to a distance of 0.670mm or 0.0264" below the tool height. Lastly, the mean of each data set was removed from the individual measurements and $0.25\mu\text{m}$ was added to each to center the wave around zero.

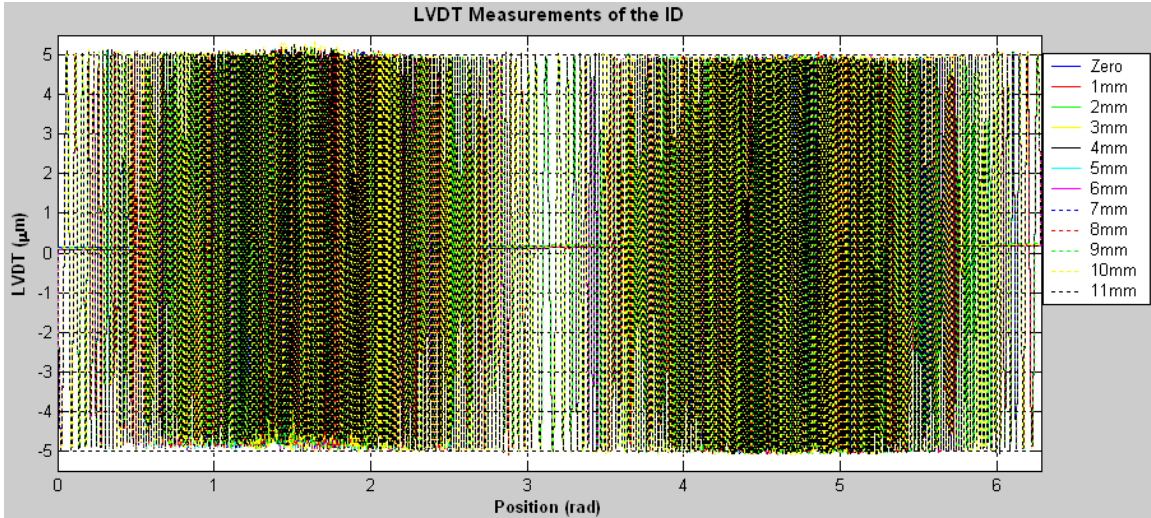


Figure 3-78. All 12 measurements of the wave on the ID of Ring 1

Figure 3-78 shows all 12 measurements. Each measurement was put into an array and an additional average of all 12 measurements was taken. This single average data set was subtracted from each measurement to determine the deviation across the width of the wave.

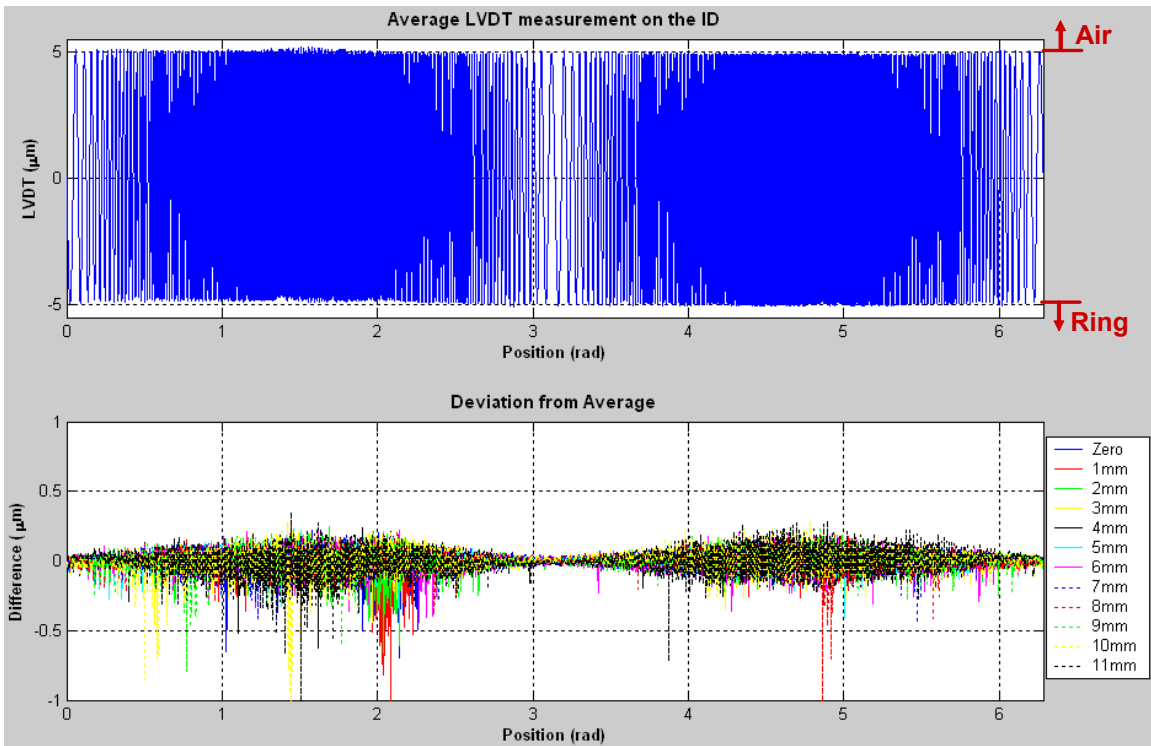


Figure 3-79. Average of measurements along with wave deviation on the ID of Ring 1

Figure 3-79 displays the average measurement in the top subplot and the deviation of each individual measurement from the average in the bottom subplot. Additional statistical analysis was performed on the measurements of the ID. The difference from average (error) data sets were placed into one array where the median, range, standard deviation, and interquartile range were found for each measurement.

Table 3-11. Summary of statistics for all ID measurements (units μm)

<i>STAT</i>	<i>1</i>	<i>2</i>	<i>3</i>	<i>4</i>	<i>5</i>	<i>6</i>	<i>7</i>	<i>8</i>	<i>9</i>	<i>10</i>	<i>11</i>	<i>12</i>
Median	0.001	0.003	-0.000	-0.001	-0.002	0.001	0.003	0.004	0.000	0.002	0.003	0.001
Min	-0.696	-1.05	-0.663	-0.460	-0.623	-0.402	-0.438	-0.454	-1.06	-0.789	-1.61	-1.12
Max	0.219	0.204	0.247	0.276	0.238	0.221	0.224	0.244	0.281	0.245	0.271	0.354
Range	0.915	1.255	0.910	0.737	0.861	0.623	0.662	0.698	1.343	1.033	1.879	1.476
St Dev	0.046	0.050	0.046	0.042	0.041	0.039	0.047	0.040	0.042	0.045	0.067	0.067
IQR	0.040	0.036	0.038	0.046	0.037	0.033	0.046	0.036	0.033	0.038	0.054	0.066

Table 3-11 summarizes the statistical measurements of the ID. Overall, the standard deviations and IQRs agree, meaning that there are few outliers that may be associated with the condition of the surface. The deviations are primarily due to the actual surface features across the width of the wave. Using the highest standard deviation of 67nm and a coverage factor (defined in Section 4.1) of 3, the user may be 99% confident that a measurement of the wave is within 0.2 μm of its true displacement.

3.3.8.3 Comparison to the Desired Wave

Once the actual wave was measured with the LVDT, it could be compared to the desired swept sine wave. For the OD of Ring 1, the minimum wavelength measured 0.383mm while the maximum wavelength is 6.384mm, which differs from the desired wavelength range of 0.447mm to 6.384mm. The longest wavelengths are equivalent but the measured shortest wavelength is 14% shorter than the desired which is partially due to the misaligned encoder. The time difference between counts is magnified at the shorter

wavelengths because the displacement from one count to the next is greater with fewer counts per wave. However, if the probe compensation equations of Section 3.2.1.2 are applied to the desired wave, the measured wave can be compared to the compensated wave. The measured wave matches the compensated wave with the maximum distance between the waves at the shortest wavelength being $7.5\mu\text{m}$. This reduces the error in the shortest wavelength to 1.68% rather than 14%. As for the magnitude, the PV is $9.63\mu\text{m}$ which is a difference of 3.68% from the $10\mu\text{m}$ PV. Figure 3-80 illustrates both waves.

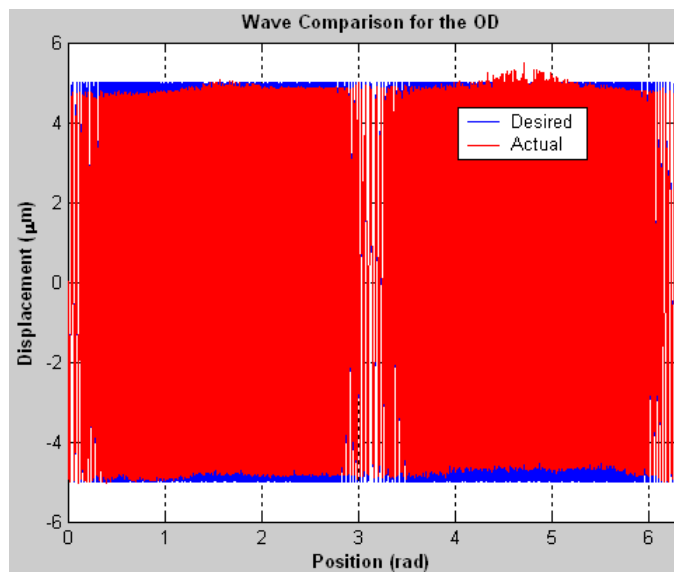


Figure 3-80. Comparison of the desired wave to the actual wave on the OD of Ring 1

If the measured wave is subtracted from the compensated wave, the error attributed to phase can also be determined. In Figure 3-81, the difference reaches $\sim 1.6\mu\text{m}$ which is significant. When the highest frequency region is expanded, it is apparent that the “circles” (actual) do not match their corresponding “stars” (compensated). Also, the distance between the waves at the shortest wavelength is $7.5\mu\text{m}$. The phase shift, rather than difference in magnitude, is the main source of error. The interpolation between encoder counts and averaging of data points may be the contributing factors. The

expanded region also illustrates the shorter than desired wavelength in the associated region.

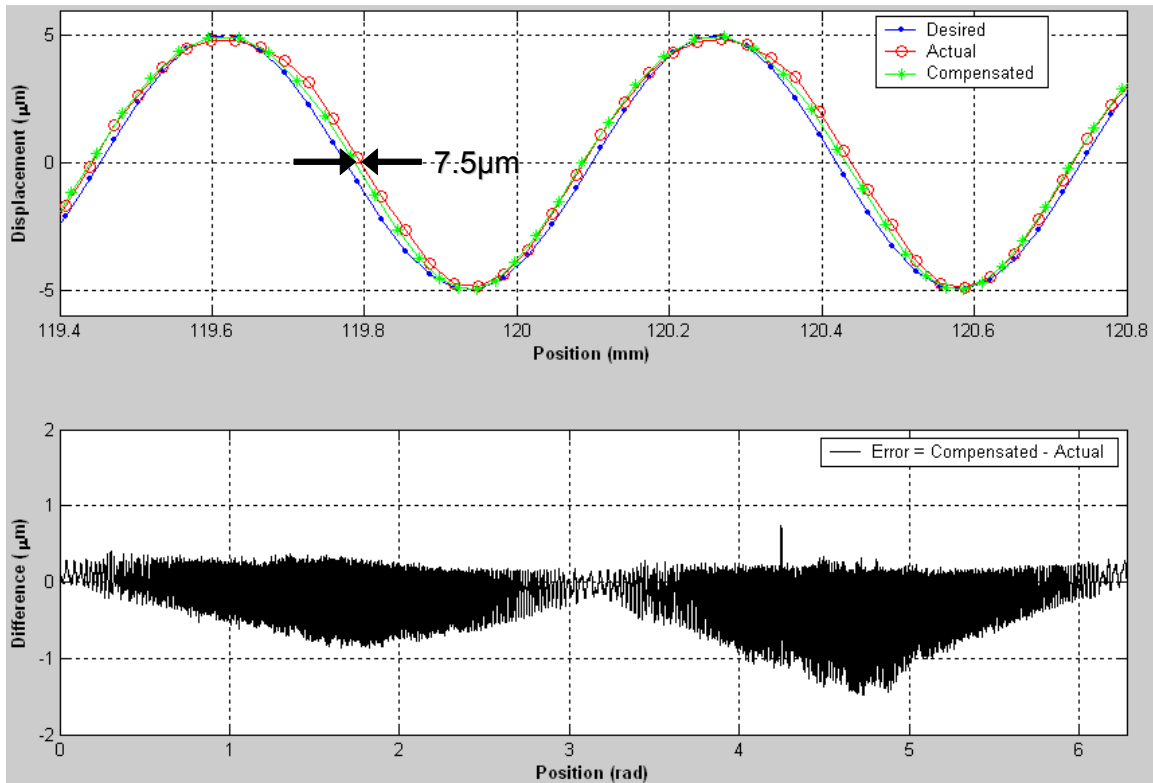


Figure 3-81. The measured wave subtracted from the compensated wave (bottom) with an expanded view at the highest frequency on the OD (top) of Ring 1

For the ID, the minimum wavelength measured 0.383mm while the maximum wavelength is 6.416mm. Again, this differs from the desired wavelength range of 0.479mm to 6.368mm. The longest wavelength is 0.75% longer than desired and the measured shortest wavelength is 20% shorter than the desired. By comparing the measured wave to the probe compensated wave, the error in the shortest wavelength reduces to 3.34%. As for the magnitude, the PV is 9.80 μ m which is a difference of 1.97% from the 10 μ m PV. Figure 3-82 illustrates both waves.

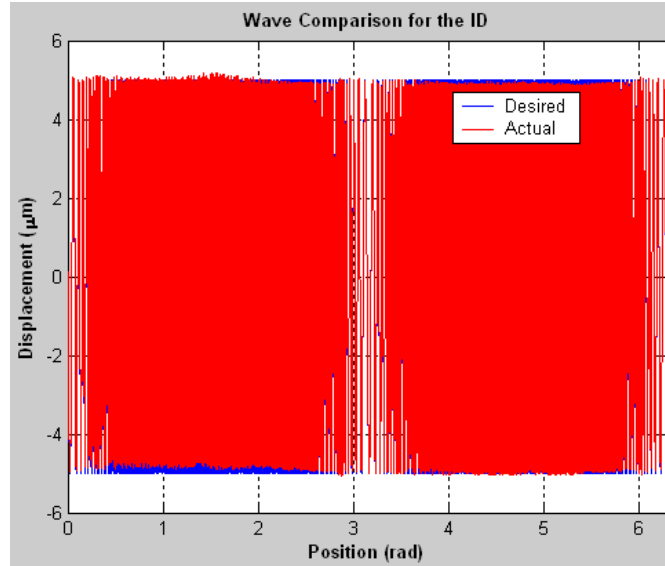


Figure 3-82. Comparison of the desired wave to the actual wave on the ID of Ring 1

In Figure 3-83, the difference reaches $1.6\mu\text{m}$ as it had on the OD. When the highest frequency region is expanded, it is apparent that the “circles” (actual) do not match their corresponding “stars” (data compensated for LVDT probe radius) with more regularity on the rising edge of the wave. The distance between the waves at the shortest wavelength is $16\mu\text{m}$ or equivalent to $\sim 11^\circ$ of phase. The interpolation between encoder counts and averaging of data points may be the contributing factors. Misalignment of the encoder on the spindle also plays a significant role in the error as it relates to the non-symmetric nature in amplitude in the high frequency sections of the wave. The expanded region also illustrates the shorter than desired wavelength in the associated region.

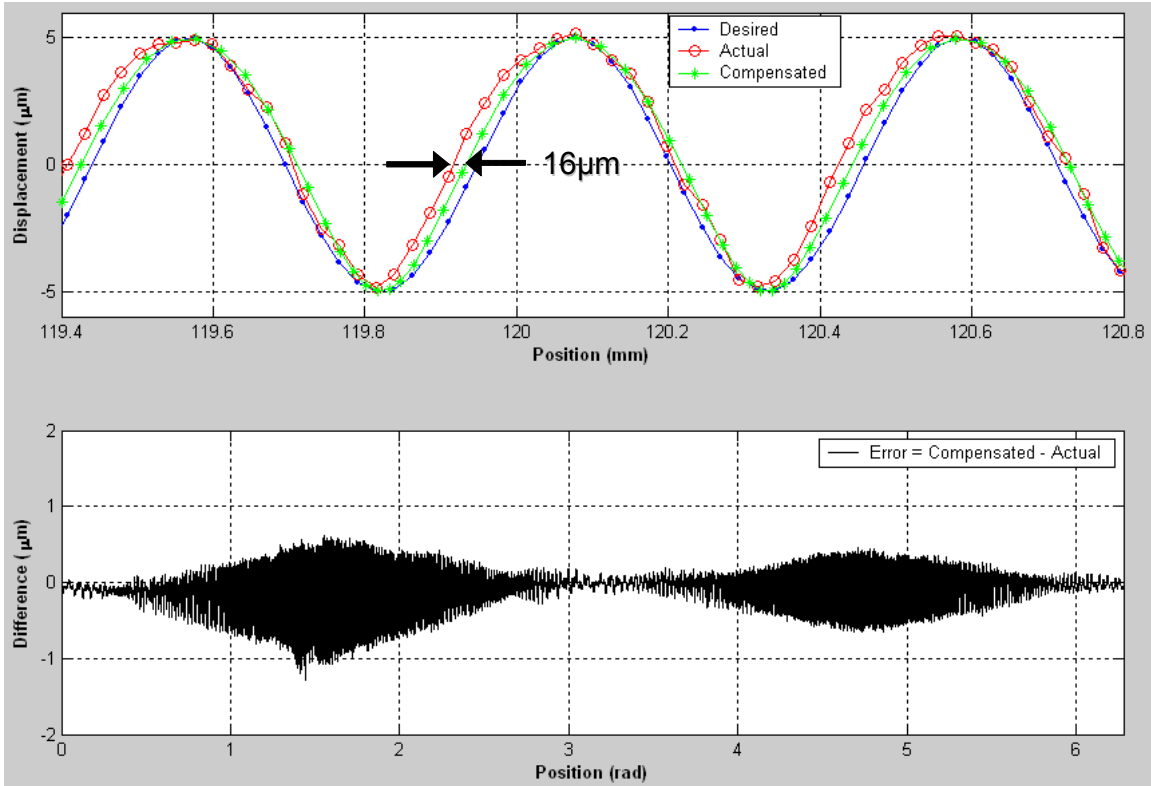


Figure 3-83. The measured wave subtracted from the compensated wave (bottom) with an expanded view at the highest frequency on the ID (top) of Ring 1

3.3.8.4 Fiducial Measurement

The cosine wave fiducial on the OD was also measured with the LVDT. The OD least squares fit was applied to this measurement to discern the true shape of the feature. The measurement contains all data points rather than an average.

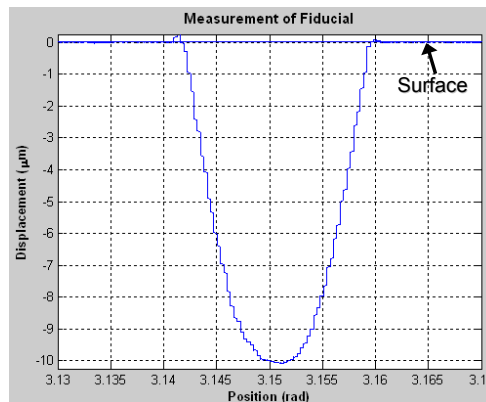


Figure 3-84. LVDT measurement of fiducial on the OD of Ring 1

Figure 3-84 shows the measurement of the fiducial feature. The surface of the ring outside the fiducial lies at $0.01\mu\text{m}$ in the figure. By capturing the points where the feature bisects $0.01\mu\text{m}$, the wavelength of the feature can be determined. The two points were found at 3.1416rad and 3.1595rad . The expected diameter of the outside of the ring is 203.2mm ($8''$); since there are 101.6mm/rad and the difference between the two points is 0.0179rad , the actual wavelength is 1.819mm . The theoretical wavelength was 1.82mm , making the actual within $\sim 1\mu\text{m}$ of the theoretical. The actual depth of the fiducial is $10.08\mu\text{m}$ from the $0.01\mu\text{m}$ reference compared to the $10\mu\text{m}$ desired.

3.3.8.5 Ridge Height Measurement

The swept sine wave was machined onto a surface (ridge) $20\mu\text{m}$ above the flat section on the OD and the ID. Since the PV of the wave is approximately $10\mu\text{m}$, the minimum height of the ridge should be $10\mu\text{m}$. After the swept sine wave measurements were completed, the spindle was secured so that it could not rotate. The LVDT probe was positioned near the fixed end of the ring on the flat section on the ID and the OD. The z-axis traversed 15mm while the probe remained in contact with the surface and measured the height of the ridge where the wave was located. Figure 3-85 illustrates the measurement on the ridge.

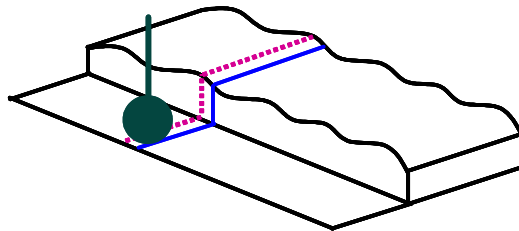


Figure 3-85. Illustration of ridge measurement

The measurement in Figure 3-86 verifies that the wave surface is at least $10\mu\text{m}$ above the flat surfaces on the OD. The spindle was not secured exactly at its zero theta position; thus, the probe is measuring on the side of one of the waves rather than in its valley.

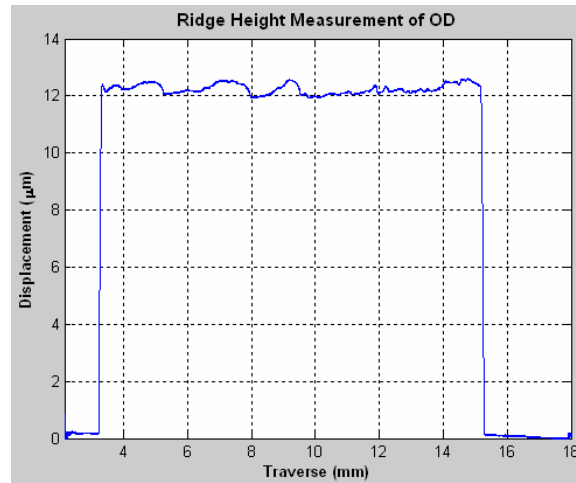


Figure 3-86. Determination of ridge height on the OD of Ring 1

The measurement on the ID (Figure 3-87) also verifies the expectation that the wave surface should be at least $10\mu\text{m}$ above the flat sections.

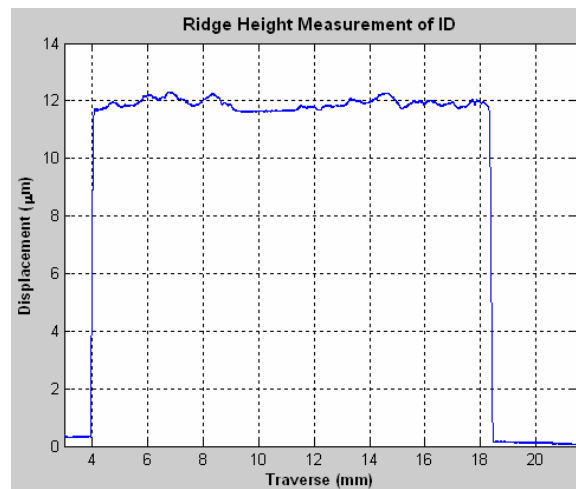


Figure 3-87. Determination of ridge height on the ID of Ring 1

3.3.9 Comparison of Ring 1 and Ring 2

A second stainless steel ring gauge was fabricated with minor improvements to the machining process. The additional fabrication also enabled the repeatability of previous errors to be determined.

3.3.9.1 Surface Finish

The diamond tool was re-lapped before it was used to machine the features on the ID and the OD of the second ring. Following fabrication, a profilometer was used to take 4 – 0.5mm measurements on the ID and the OD of Ring 2 to determine surface finish.

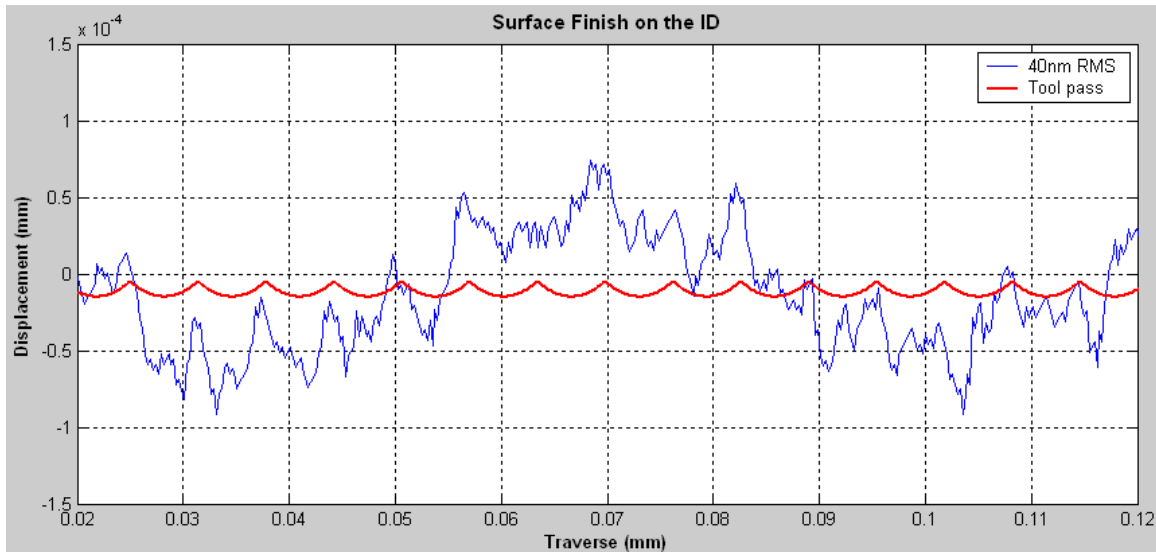


Figure 3-88. Profilometer measurement of surface finish on the ID of Ring 2

Two measurements were taken on each side of the wave at random locations on the non-wavy sections. The four total measurements identified the surface finish to be 27, 44, 22 and 40nm RMS with an average of 33nm RMS. Figure 3-88 illustrates a portion (0.1mm) of one of the measurements on the ID. The symmetrical curves demonstrate the theoretical tool passes during machining.

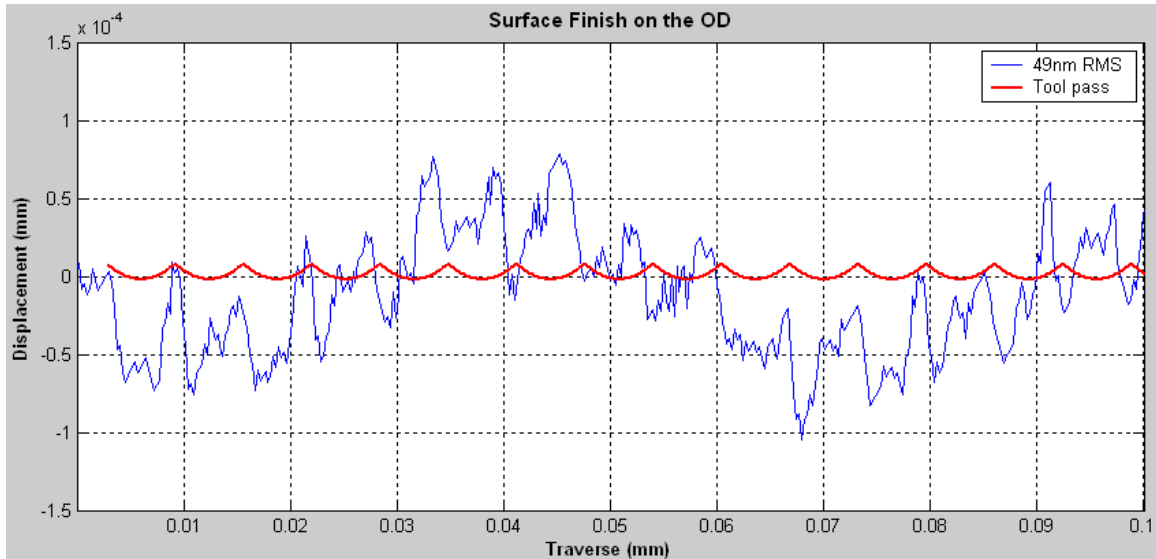


Figure 3-89. Profilometer measurement of surface finish on the OD of Ring 2

On the OD, 2 measurements were also taken at random locations on each non-wavy section. The four measurements determined the surface finish to be 32, 60, 37 and 49nm RMS with an average of 44nm RMS. Figure 3-89 represents part (0.1mm) of one of the measurements. Again, the symmetrical curves show the theoretical path of the tool during machining.

As with Ring 1, the surface finish is higher than the theoretical value of 3nm RMS. The same reasons as before (tool damage, inconsistent feed rate, machine error) are true for Ring 2. For the ID, the PV of each machining pass is approximately 50nm when it was ~ 120 nm for Ring 1. The OD was machined following the ID which leads to a PV of 75nm for each machining pass, indicative of additional tool damage from the fabrication of the ID. However, tool damage is less significant as compared to the machine error. Figure 3-88 and Figure 3-89 illustrate a low frequency sine wave with an amplitude of 50nm over the entire surface. This may be caused by vibration of the FTS, vibration of

the machine axes or a combination of the two. The specific cause will need to be determined if another ring gauge is fabricated.

3.3.9.2 Roundness

The out-of-round characteristic of the ID measured $0.32\mu\text{m}$ for Ring 2 compared to $0.35\mu\text{m}$ for Ring 1. The concentricity between the flat surface and the wave surface was also verified. Figure 3-90 illustrates the roundness and concentricity of the ID on the second ring.

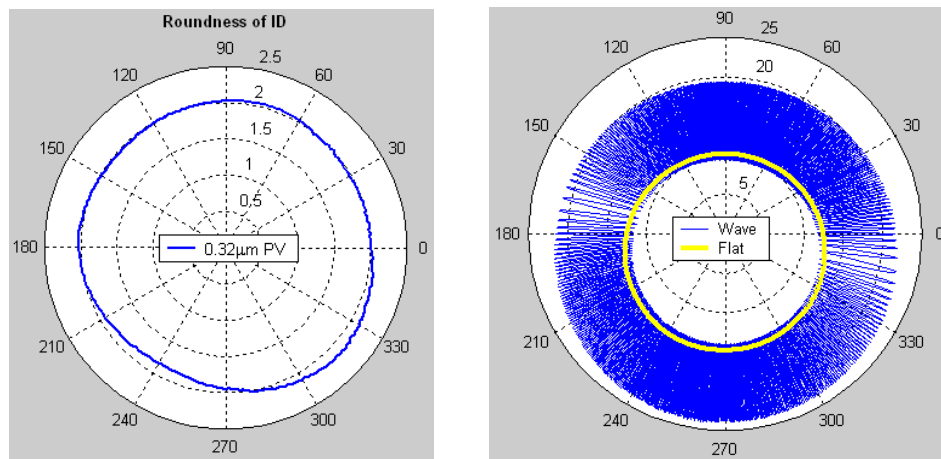


Figure 3-90. Roundness and concentricity of ID of Ring 2

On the OD of Ring 2, the out-of-round value measured $0.12\mu\text{m}$ as compared to $0.17\mu\text{m}$ on the first ring. The flat and wave sections are also concentric. Figure 3-91 shows the polar plots of both measurements.

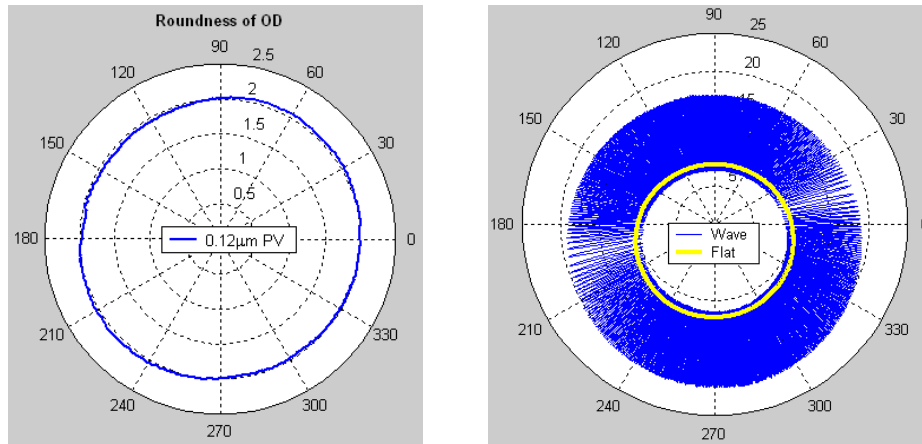


Figure 3-91. Roundness and concentricity of OD of Ring 2

Although the out-of-roundness has improved on Ring 2, it becomes necessary to check the shape of both IDs and ODs of the rings to inspect the consistency of the shape error. Figure 3-92 reflects the shape error on the ID and the OD. The “dotted” line represents Ring 1 while the “solid” line describes Ring 2. On the OD, the errors match almost perfectly. However, the ID comparison delineates a few differences in shape. Nonetheless, it seems that the errors are consistent which makes an argument that the error is due to the error of the DTM spindle. The same fabrication procedure with a re-lapped diamond tool was used on each ring; the measurement and data analysis was also performed in the same way as well.

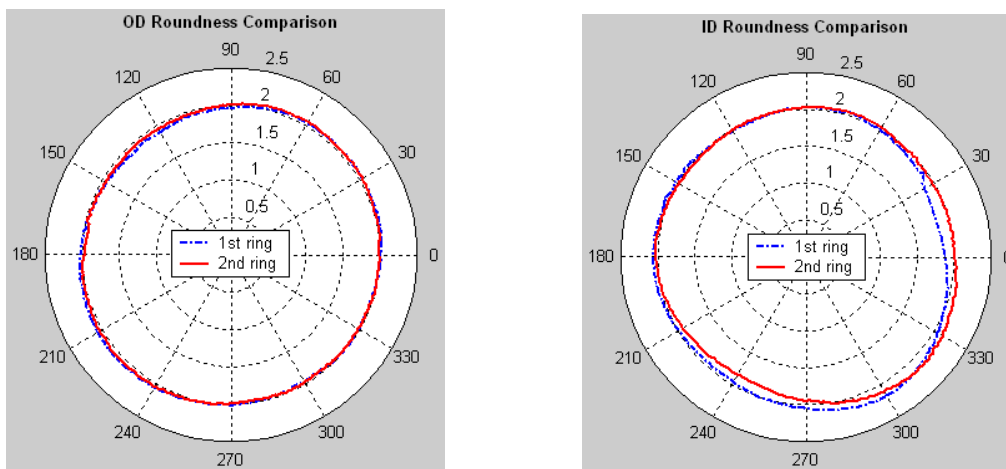


Figure 3-92. Comparison of roundness of both rings

3.3.9.3 Swept Sine Wave Surface

Prior to the second fabrication of the waves, the encoder signal was inspected. The previous fabrication had shown a lack of symmetry in the amount of error in the short wavelength sections of the wave. The signal inspection exposed an inconsistency in the width of one of the wave signals; the width would expand and contract several times per revolution. This inconsistency affects the time between encoder counts which directly affects the command to the FTS. When the encoder was re-aligned, the problem was reduced and the swept sine waves were machined onto their respective surfaces.

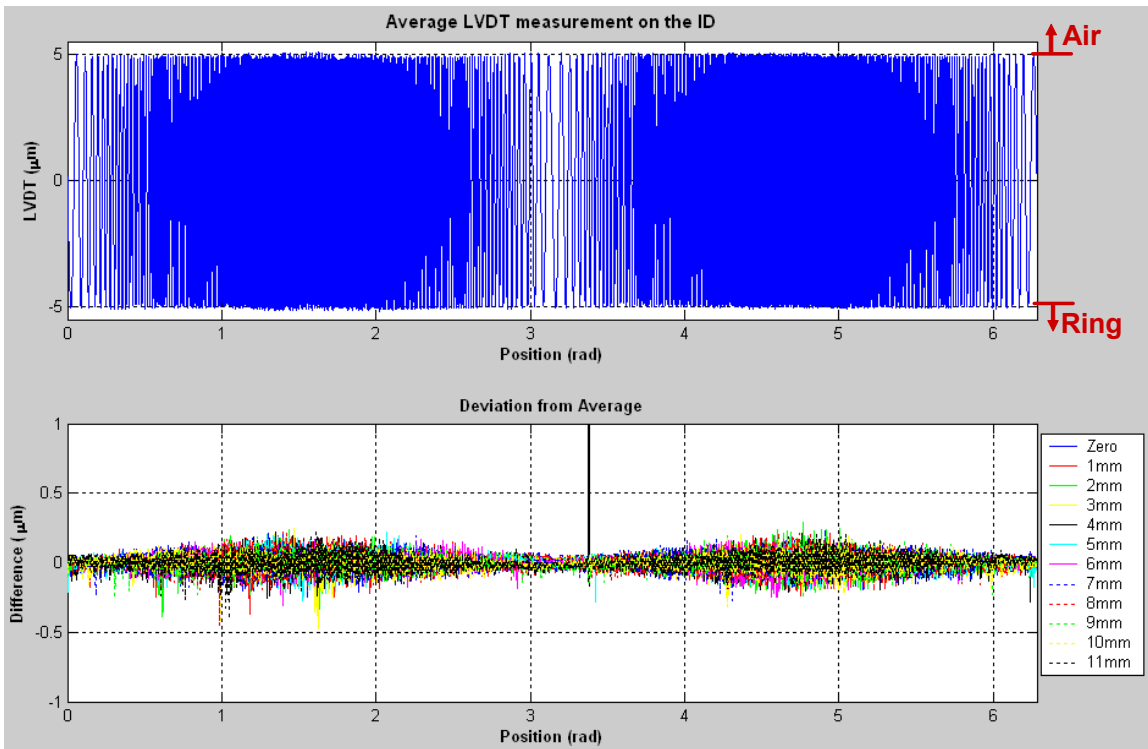


Figure 3-93. Average of measurements along with wave deviation on the ID of Ring 2

Figure 3-93 shows the average of the 12 measurements taken on the ID of Ring 2 with each measurement's difference from the average data set across the width of the wave. To compensate for the difference in LVDT height from the height of the tool during fabrication, each data set was shifted by 66 counts to cause the longest wavelength to

begin at zero. The 66 counts translates to a distance of 1.60 mm or 0.063” below the tool height. Lastly, the mean of each data set was removed from the individual measurements and 0.2 μ m was added to each to center the wave around zero. Statistical analysis was performed on the measurements of the ID as on the first ring. The median difference ranges from less than 1nm to 3nm along the 12 data set which is an improvement from Ring 1.

Table 3-12. Summary of statistics for all ID measurements on Ring 2 (units μ m)

<i>STAT</i>	<i>1</i>	<i>2</i>	<i>3</i>	<i>4</i>	<i>5</i>	<i>6</i>	<i>7</i>	<i>8</i>	<i>9</i>	<i>10</i>	<i>11</i>	<i>12</i>
Median	0.003	0.002	0.002	0.002	0.001	0.002	0.002	0.000	-0.001	-0.000	0.000	-0.000
Min	-0.21	-0.37	-0.39	-0.48	-0.28	-0.28	-0.31	-0.27	-0.45	-0.26	-0.43	-0.41
Max	0.21	0.21	0.29	0.24	1.47	0.22	0.19	0.24	0.22	0.18	0.20	0.22
Range	0.42	0.58	0.68	0.72	1.75	0.50	0.50	0.51	0.67	0.44	0.63	0.63
St Dev	0.044	0.041	0.042	0.038	0.042	0.038	0.038	0.039	0.040	0.036	0.038	0.040
IQR	0.066	0.044	0.038	0.037	0.039	0.037	0.036	0.042	0.042	0.040	0.042	0.046

Table 3-12 displays a summary of the statistics. The standard deviation from the average wave of the individual measurements range from 36nm to 44nm. The IQR consists of a similar range which means that outliers are not a factor in the measurements. Thus, the standard deviation is more representative of the spread of the data. Using a coverage factor of 3 (see Section 4.1 for more explanation) and the maximum standard deviation of 44nm, the user can be 99% confident that the magnitude of the wave is within 0.132 μ m of its true magnitude when a measurement is taken anywhere across its width.

The average wave data set was compared to the desired wave for Ring 2 in Figure 3-94. For the ID, the minimum wavelength measured 0.431mm while the maximum wavelength is 6.368mm. The longest wavelength is equivalent to the desired but the measured shortest wavelength is 10% shorter than the desired wavelength of 0.479mm.

A comparison with the desired wave after the probe compensation equations of Section 3.2.1.2 were applied reduces the error of the shortest wavelength to 1.90%. As for the magnitude, the PV is $9.94\mu\text{m}$ which is a difference of 0.65% from the $10\mu\text{m}$ PV. Overall, the error in the wavelength and magnitude of the wave has improved over Ring 1 which can be attributed to the re-alignment of the encoder on the spindle.

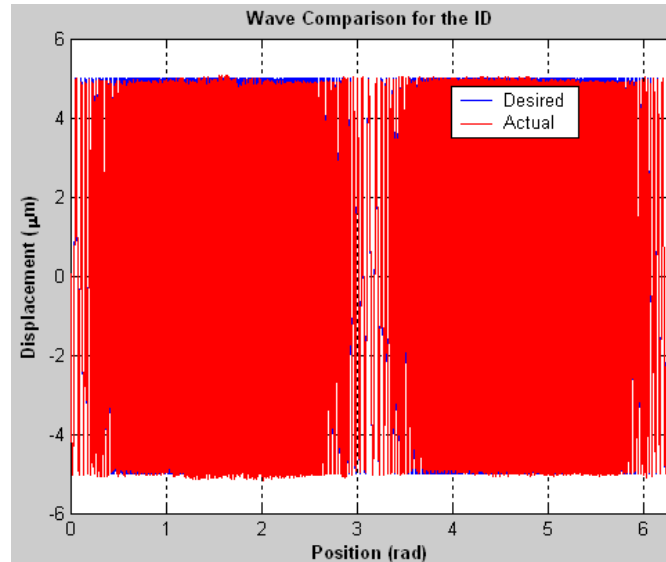


Figure 3-94. Comparison of the desired wave to the actual wave on the ID (Ring 2)

If the measured wave is subtracted from the compensated wave, the error corresponding to phase can also be determined. In Figure 3-95, the difference reaches $\sim 1\mu\text{m}$ which is less than the $1.6\mu\text{m}$ of Ring 1. However, when the highest frequency region is expanded, it is still apparent that the “circles” (actual) do not match their corresponding “stars” (compensated). The distance between the waves at the shortest wavelength is $9.1\mu\text{m}$ which is almost half as much as Ring 1. The difference in the time between encoder counts due to an imperfect alignment is exemplified by the non-symmetric waves. The expanded region also illustrates the shorter than desired wavelength in the associated region. Nonetheless, it is an improvement over Ring 1.

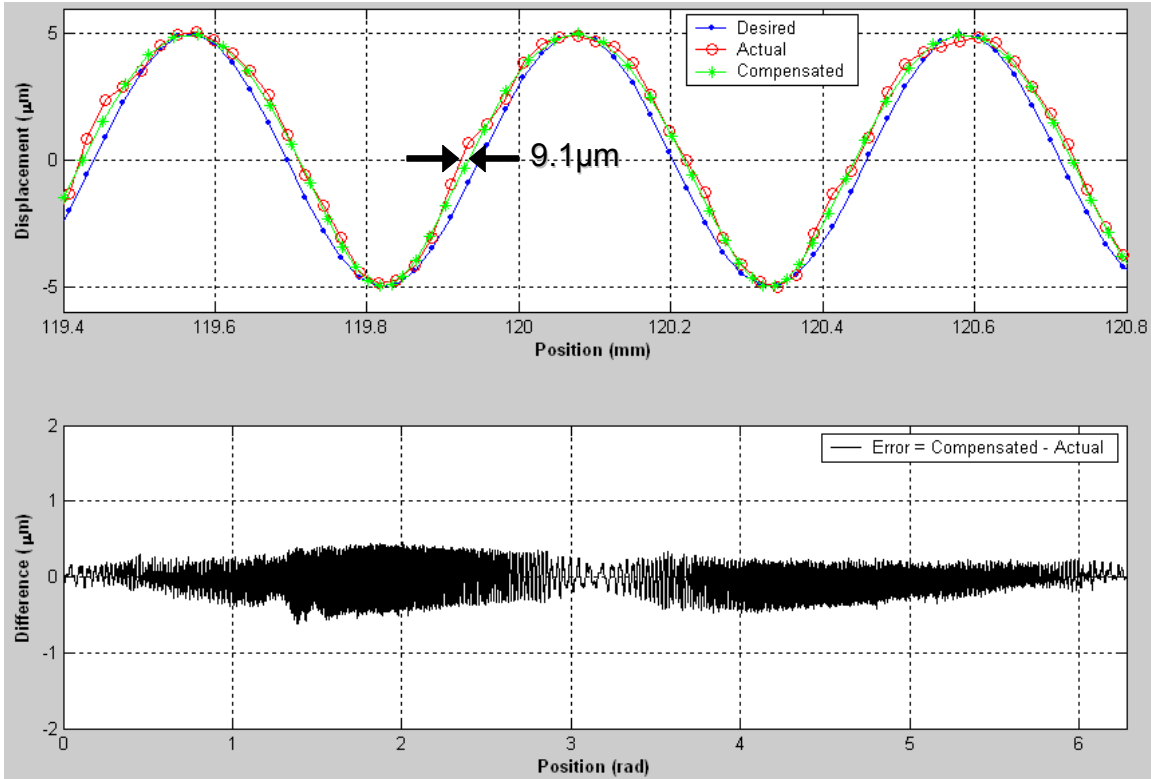


Figure 3-95. The measured wave subtracted from the compensated wave with an expanded view at the highest frequency on the ID on Ring 2

The LVDT also measured the wave on the OD of Ring 2. Figure 3-96 shows the average of the 12 measurements taken on the OD of the ring with each measurement's difference from the average data set across the width of the wave. To compensate for the difference in LVDT probe height from the height of the tool during fabrication, each data set was shifted by 49 counts to cause the longest wavelength to begin at zero. The 49 counts translates to a distance of 1.56 mm or 0.062" below the tool height. Lastly, the mean of each data set was removed from the individual measurements and 0.205µm was added to each to center the wave around zero.

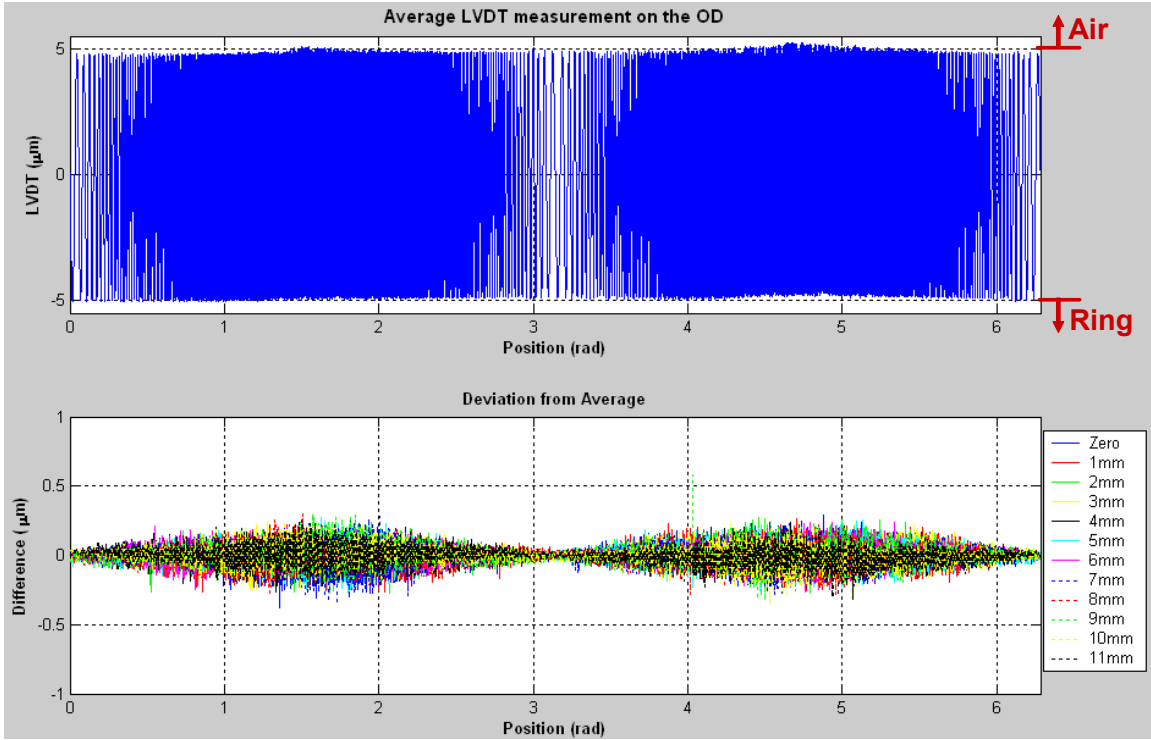


Figure 3-96. Average of measurements along with wave deviation on the OD of Ring 2

Statistical analysis was performed on the measurements of the OD on Ring 2. The median difference ranges from less than 1nm to 3nm along the 12 data set which is an improvement over Ring 1. Table 3-13 displays the rest of the results. Overall, the wave deviates a maximum of 53nm across its width.

Table 3-13. Summary of statistics for all OD measurements on Ring 2 (units µm)

<i>STAT</i>	<i>1</i>	<i>2</i>	<i>3</i>	<i>4</i>	<i>5</i>	<i>6</i>	<i>7</i>	<i>8</i>	<i>9</i>	<i>10</i>	<i>11</i>	<i>12</i>
Median	-0.003	-0.002	-0.002	-0.001	0.001	-0.000	0.002	0.003	0.001	-0.001	0.002	0.003
Min	-0.38	-0.27	-0.27	-0.25	-0.31	-0.27	-0.27	-0.35	-0.29	-0.32	-0.36	-0.30
Max	0.29	0.26	0.27	0.24	0.25	0.27	0.24	0.28	0.30	0.58	0.27	0.24
Range	0.67	0.53	0.54	0.49	0.56	0.54	0.51	0.63	0.59	0.90	0.63	0.54
St Dev	0.053	0.050	0.050	0.050	0.040	0.049	0.044	0.048	0.046	0.047	0.047	0.046
IQR	0.057	0.052	0.059	0.062	0.037	0.050	0.039	0.044	0.047	0.047	0.049	0.047

For the OD, the minimum wavelength measured 0.383mm while the maximum wavelength is 6.384mm. Again, the minimum wavelength differs from the desired wavelength of 0.447mm. The maximum wavelengths are equivalent and the measured

shortest wavelength is 14% shorter than the desired. By comparing the measured wave to the probe compensated wave, the error in the shortest wavelength reduces to 1.83%. As for the magnitude, the PV is $9.75\mu\text{m}$ which is a difference of 2.52% from the $10\mu\text{m}$ PV. The measured wavelengths are almost the same as Ring 1 and the magnitude has improved.

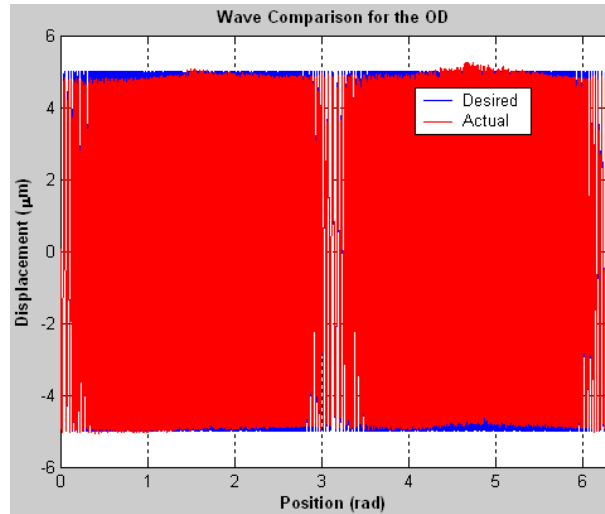


Figure 3-97. Comparison of the desired wave to the actual wave on the OD (Ring 2)

The difference in the actual wave compared to the compensated wave is approximately $1.75\mu\text{m}$. The error has increased from the ID to the OD due to the higher frequencies of the wave during fabrication with the FTS. However, the error is more symmetric than Ring 1. Figure 3-98 shows an expanded view of the short wavelength section of the swept sine wave. As with the other comparable figures, the phase of the actual wave closely matches the compensated wave on the rising edge of the wave but increases at the falling edge. The maximum distance between the waves at the shortest wavelength is $8.2\mu\text{m}$. The interpolation between encoder counts and averaging of data points may still be the contributing factors as well as the dynamics of the LVDT (Figure 4-5).

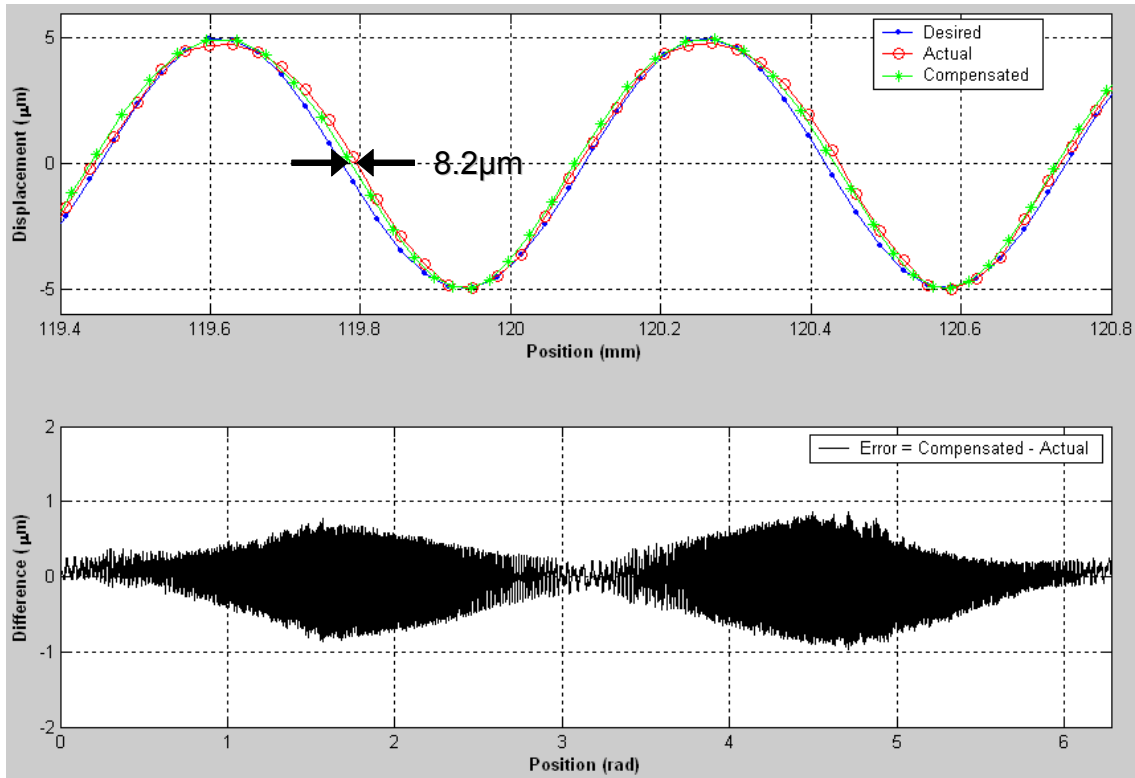


Figure 3-98. The measured wave subtracted from the compensated wave with an expanded view at the highest frequency on the OD on Ring 2

4 APPLICATION OF ARTIFACT TO CMM CALIBRATION

The ring gauge artifact will be used to calibrate a CMM and determine the machine’s dynamic and static characteristics. However, a specific procedure for implementation must be defined to facilitate interpretation of measurement results.

4.1 UNCERTAINTY

All measurements exhibit uncertainty. The *International Vocabulary of Basic and General Terms in Metrology* (VIM) and the *U.S. Guide to the Expression of Uncertainty in Measurement* (GUM) describe uncertainty as a “parameter, associated with the result of a measurement, that characterizes the dispersion of the values that could reasonably be attributed to the measurand [24].” The measurand is the description of the quantity to be

measured. It consists of defined physical states and conditions such as room temperature, humidity, barometric pressure, measurement force, and support of the artifact. If the measurand is Y , then

$$Y = f(X_1, X_2, \dots, X_N) \quad (8)$$

where X_i is an input quantity upon which Y depends. X_i may also be dependant on other quantities, so f is described as a function that comprises all quantities that will add significant components of uncertainty to the measurement. The set of input quantities can be designated as quantities with values and uncertainties which are directly determined from the measurement or brought in from an external source [24]. An external source may be data from a calibrated artifact such as the ring gauge, reference data from handbooks, or certified reference materials.

The values for the input quantities may be obtained using Type A evaluation of standard uncertainty. Type A evaluation of uncertainty is defined as the “method of evaluation of uncertainty by the statistical analysis of series of observations [2.3.2 of 24].” Thus, the estimated variance of an uncertainty component from a Type A evaluation is found with a series of experimental observations. The square root of the variance is referred to as the estimated standard deviation or Type A standard uncertainty. The degrees of freedom ($n-1$) should be given based on the n observations with the average and standard deviation. Section 4.2.8 of the GUM [24] indicates that the components of uncertainty may be obtained through a nested sequence of measurements of the measurand, often referred to as an analysis of variance.

Before an uncertainty analysis can be performed, it is important to distinguish between error and uncertainty. There are two components to error: random effects and systematic effects.

- Random error consists of unpredictable variations in a measurement. These variations cannot be compensated but reduced with an increased number of observations. The experimental standard deviation from the arithmetic mean of the observations is not the random error but rather the uncertainty of the mean from random effects [3.2.2 from 24].
- Systematic error occurs when a recognizable effect influences an input quantity of the measurand. This error can be quantified and reduced if deemed too large; a correction would be applied to the measurement to compensate for the effect based on the measurement of the recognizable effect. The uncertainty of the correction to compensate for systematic effects is not the systematic error; rather, it is the measure of the uncertainty of the result due to not fully knowing the required value of the correction of the systematic effect [3.2.3 from 24].

After each uncertainty has been defined, all need to be combined into one uncertainty value. In the case of the ring gauge, some of the input quantities such as the diameter of the probe and the measurement speed, are correlated (interdependent). For correlated input quantities, the combined variance, $u_c^2(y)$, is:

$$u_c^2(y) = \sum_{i=1}^N \left(\frac{\partial f}{\partial x_i} \right)^2 u^2(x_i) + 2 \sum_{i=1}^{N-1} \sum_{j=i+1}^N \frac{\partial f}{\partial x_i} \frac{\partial f}{\partial x_j} u(x_i, x_j) \quad (9)$$

$u(x_i, x_j)$ is the estimated covariance of the estimated input quantities x_i and x_j . If all of the input estimates are correlated, Equation (9) reduces to

$$u_c^2(y) = \left(\sum_{i=1}^N \frac{\partial f}{\partial x_i} u(x_i) \right)^2 \quad (10)$$

This implies that the combined uncertainty is the linear sum of the standard uncertainties of each input estimate x_i [24].

In some applications, it may be necessary to report an expanded uncertainty, U , that creates a larger distribution interval of possible values around the measurement result. The expanded uncertainty is found by multiplying the combined standard uncertainty by a coverage factor, k . The coverage factor is a numerical factor intended to expand the uncertainty to encompass a larger fraction of the distribution of values in the measurand.

$$U = k u_c(y) \quad (11)$$

The choice of the coverage factor is dependant upon the desired level of confidence [24].

4.2 DEFINITION OF MEASURAND

As discussed in Section 4.1, the measurand has to be defined before any measurements may be taken. The requirements for measurement are listed below:

- 1) Measured at a room temperature of 20°C.
- 2) Measure only the ID or only the OD; each exhibits differing frequencies.
- 3) All measurements are to be taken in the same orientation.
- 4) Use the same probe for all measurements.
- 5) Measure the swept sine wave with at least 3 different speeds with 3 measurements at each speed.

The input quantities of the measurand include only temperature and measurement speed since the probe and orientation are not changing. (If multiple orientations or probes were used, additional uncertainty components would be added to the equation.) Both quantities will affect the measurement results and may be considered to be correlated because they cannot be separated independently from one another during a single experiment. Thus, the combined uncertainty will be a composite of the temperature uncertainty, the pooled uncertainty of the various speeds, and the uncertainty associated with the accepted calibration data taken at the Precision Engineering Center (PEC).

4.3 UNCERTAINTY OF CALIBRATED ARTIFACT

The ring gauge was measured in a temperature-controlled laboratory at the PEC; the temperature was $20^{\circ}\text{C} \pm 0.05^{\circ}\text{C}$. All measurements were taken in the vertical orientation.

The uncertainty associated to changes in temperature is

$$\Delta l = l * \alpha * \Delta T \quad (12)$$

where Δl is the change in the cross-sectional length = $0.254\mu\text{m}$

l is the cross-sectional length = 25.4mm

α is the coefficient of thermal expansion = $10.8 * 10^{-6}/^{\circ}\text{C}$

ΔT is change in temperature = 0.1°F or 0.056°C

The standard deviation of the wave along the width of Ring 1 on the OD is 92nm (from Table 3-10); the standard deviation along the width of the ID is 67nm (from Table 3-11). Using Equation (10) and the result of Equation (12), the combined uncertainty of the OD is 346nm while it is 321nm for the ID. For Ring 2, the standard deviation of the OD is 53nm (Table 3-13) and 44nm for the ID (Table 3-12). The combined uncertainty is 307nm for the OD and 298nm for the ID.

4.4 DEMONSTRATION OF USE

The definition of the measurand in Section 4.2 leads into the demonstration of the artifact. The procedure may be authenticated via measurements with a LVDT. The LVDT at the PEC has dynamics that are unknown and finding them may prove to be beneficial for the future use of the instrument. Measurements were taken with the LVDT on the second ring gauge following fabrication. The ring remained mounted on the DTM spindle in the vertical orientation. The diameter of the probe tip was 1mm. Three measurements were taken on the OD at random locations on the swept sine wave while the spindle rotated at 1RPM. The process was repeated with spindle speeds of 2RPM and 3RPM. The same spindle speeds were also used for the measurements on the ID. Each measurement data set contained vectors of time, encoder counts, and LVDT output in Volts. The sampling rate of each measurement was also recorded.

Following the measurements, the data was analyzed in a series of steps. The sampling rate and the multiple revolutions (at least 1 revolution per data set) of data capture created several displacement values of the wave at a single encoder count. As described in the analysis of the swept sine wave measurement of Section 3.3.8.2, each measurement data set was averaged to produce a total of 20,000 points on the wave and a least squares fit was applied to the data to remove the off-center and out-of-round aspects of the ring. The three measurements at one spindle speed were combined and averaged to produce one representative measurement at the specific speed. From a single measurement at the spindle speed, the true elapsed time of one revolution was determined. The time frame provided bounds for the interpolation of both the “accepted” swept sine wave data set

(from Figure 3-93 for the ID and from Figure 3-96 for the OD of Ring 2) and the representative data set to a higher sampling rate of 20kHz in the time domain; more points on the waves improves the ability to determine the transfer function of the instrument without changing the frequency content of the swept sine wave measurement.

The higher measurement speeds created an automatic phase shift in the measurement from the “accepted” data set. Thus, the measured wave did not begin with zero displacement at the start of the wave. To facilitate the correct calculation of the transfer function, both waves were shifted to maintain the same spacing while originating the measured wave at zero. The first point of the “accepted” data set was set to equal the first point of the measurement for continuity of the FFT calculation. Also, only a quarter of the swept sine wave was necessary to determine the system dynamics; the complete wave tends to cancel values out and creates confusion in the interpretation of the transfer function. As with the first point, the last point of the quarter wave of each data set was set to equal the other so that the first point begins where the last point left off due to the assumption of infinite repetition of the signals by the FFT algorithm. After the manipulation of the data sets, the transfer function of the instrument was found.

Each wave is filtered through a moving average algorithm in Matlab to smooth out the wave to make the shape more uniform; the amplitude and phase are not affected but rather the shape. The “xfer” function (see Section 7.4.5 for code) finds the transfer function between the two data sets. “Xfer” calculates the FFT of each signal, divides the two and calculates the magnitude and phase in the frequency domain. The moving

average is again applied to the magnitude and phase components following “xfer” due to remaining noise and imperfections in the signals. The overall shape of the transfer function is found by smoothing the data.

The transfer function of the LVDT found using 1RPM, 2RPM and 3RPM differ from each other slightly. The transfer functions are shown in Figure 4-1 using the measurements from the ID of Ring 2. All three figures contain the same frequency range on the horizontal axis. The magnitude plots demonstrate that the measurement of the amplitude of the wave remains constant until around 10Hz where it begins to increase until the LVDT’s natural frequency is reached where the magnitude is twice as large. The lower frequencies in the 3RPM plot of the magnitude are not as stable due to the higher starting frequency of the wave during the measurement; however, the higher frequencies are more accurate with 3RPM than with 1RPM for the same reason. Also, the phase plot in each figure remains steady until 10Hz where it gradually increases until the natural frequency is reached. The phase quickly decreases before increasing again where it finally decreases around 1000Hz.

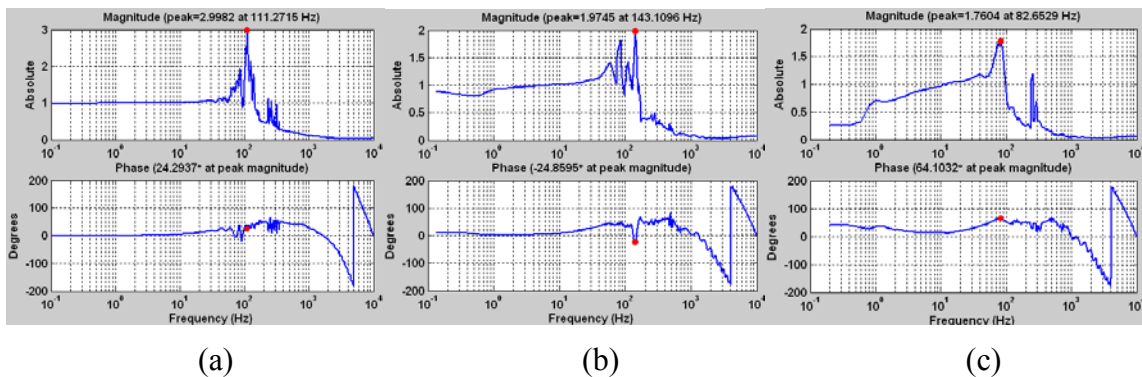


Figure 4-1. Transfer function of the LVDT on ID of Ring 2 at (a) 1RPM, (b) 2RPM, (c) 3RPM

For the OD of Ring 2, the transfer function of the LVDT found using 1RPM, 2RPM and 3RPM also differs from each other slightly but is more consistent than the ID. The magnitude remains constant until 10Hz and increases to an average of 2 near the natural frequency before decreasing to nearly zero. The characteristics of the phase plot for the OD mimics the characteristics as shown for the ID; the phase remains constant until 10Hz where it increases before rapidly decreasing at the natural frequency. Figure 4-2 illustrates the characteristics of the transfer function of the LVDT using the measurements on the OD.

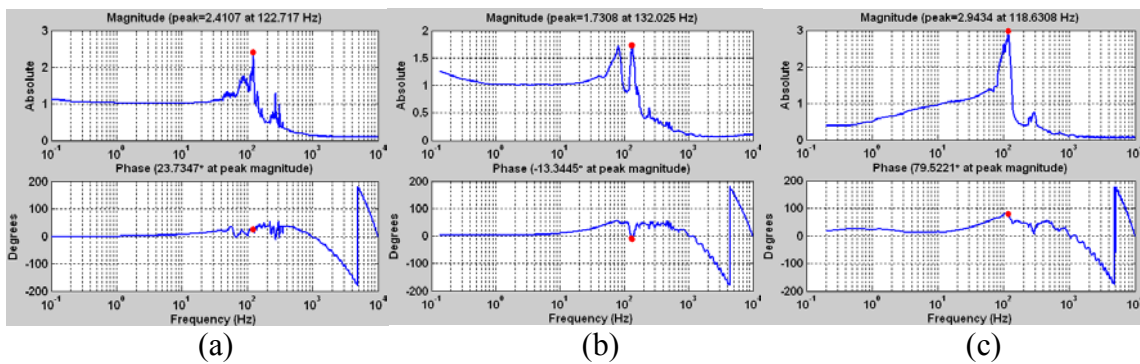


Figure 4-2. Transfer function of the LVDT on OD of Ring 2 at (a) 1RPM, (b) 2RPM, (c) 3RPM

The natural frequency of the LVDT appears to be between 120 and 130Hz. The imperfect fabrication of the swept sine wave with a slightly misaligned encoder creates problems in the final application of the ring and analysis of measurement data. The values for the magnitude and phase are more accurate in the lower frequency range with the 1RPM measurements, more accurate in the mid-frequency range with the 2RPM measurements and more accurate in the high frequency range with the 3RPM measurements due to the frequency content of each measurement. For this reason, the location of the natural frequency seems to be more distinct using the 2RPM data sets.

Another reason for inconsistency in the transfer function plots between speeds is due to the different response of the LVDT across the sections of the swept sine wave during measurement. Figure 4-3 illustrates the three measurements with the “accepted” data set. The 3RPM measurement depicts the differing responses more readily. The first quadrant of data of each measurement was used in the calculation of the transfer function. There is more discrepancy between measurements on the ID in the first quadrant than on the OD.

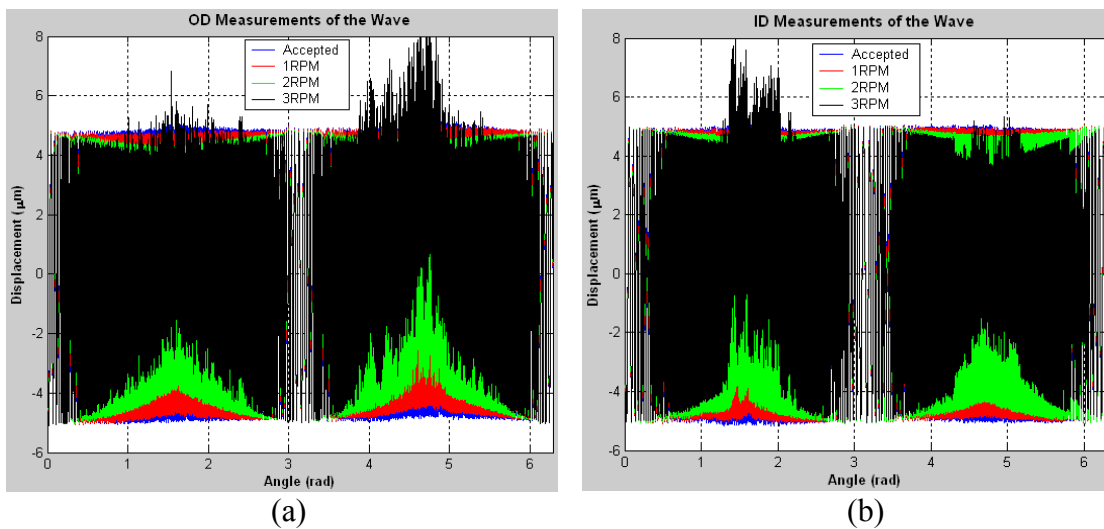


Figure 4-3. Measurement of the swept sine wave on Ring 2 with different speeds on the
(a) OD and (b) ID

4.4.1 Verification of LVDT Dynamics

The transfer function of the LVDT was found using the FTS, a function generator and an oscilloscope. The FTS was mounted to an optical table along with the LVDT; the tip of the LVDT pressed against the FTS tool holder. Single frequency sine waves were sent to

the FTS using a function generator. Figure 4-4 illustrates the setup to find the transfer function of the LVDT¹⁰.

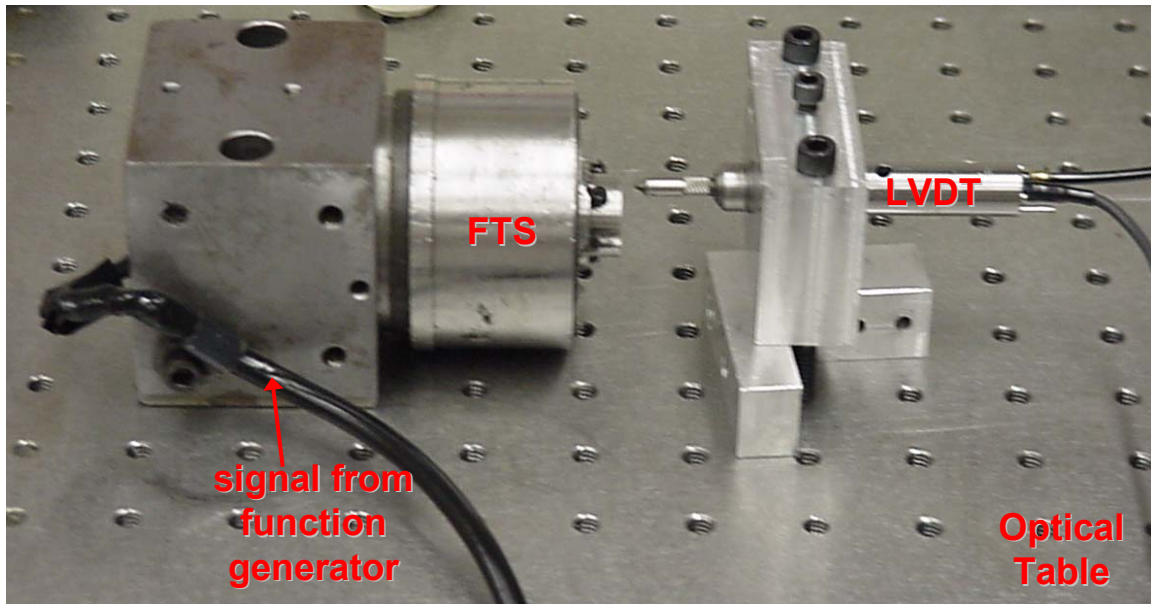


Figure 4-4. Setup to determine dynamics of LVDT

The oscilloscope captured the signal from the function generator and the output of the LVDT in Volts. The oscilloscope also recorded the phase between the two signals, the amplitude of the LVDT output and the frequency of the generated sine wave. The amplitude of the LVDT output was converted to an absolute magnitude by dividing each value by the first amplitude. Figure 4-5 displays the results of the magnitude and phase of the LVDT. The natural frequency where the phase crosses -90° is approximately 85Hz. The magnitude decreases to zero around 300Hz. However, it never increases prior to the natural frequency (due to the filtering of the electronics) which is a characteristic of a second order system.

¹⁰ Dynamics of the FTS may not be completely separated from the LVDT dynamics since the probe tip is not directly attached to the servo.

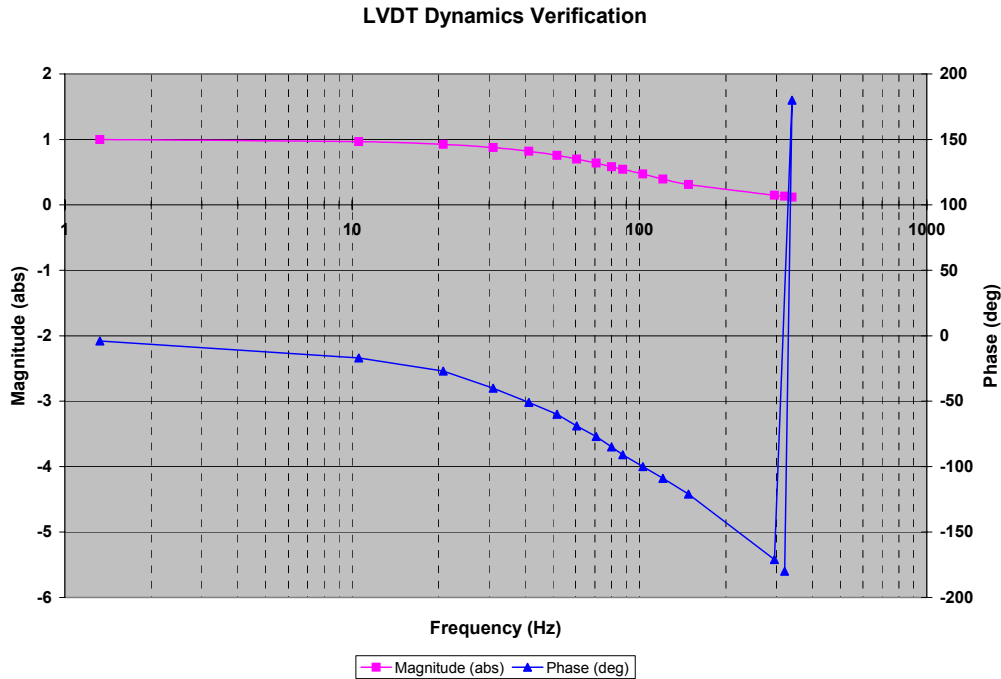


Figure 4-5. Transfer function of the LVDT

The transfer functions found in Figure 4-1 and Figure 4-2 differ from the actual dynamics of the LVDT. However, if the first peak on the magnitude plot is used, the natural frequency is within the 80Hz range. The phase also approaches 90° at this frequency. Discrepancies between the transfer functions can be attributed to an imperfect swept sine wave.

4.4.2 Dynamic Implications

The identification of the dynamics of the LVDT highlights some concerns with the analysis of ring gauges 1 and 2. The “accepted” data set of the swept sine wave measurement was taken using a spindle speed of 0.5RPM. On the OD of Ring 2, the highest frequency measured is approximately 11Hz. Figure 4-5 indicates that there is a 5% decrease in magnitude and ~20° of phase associated with 11Hz. This may account for a portion of the error identified in the swept sine wave. To get a final accurate

account of the ring gauge, the dynamics of the LVDT would need to be taken into consideration during the measurement. The ring would need to be either measured at a slower speed or using a different LVDT that had a higher natural frequency. With the current measurement setup, the former can only marginally be improved. A higher natural frequency LVDT may be the better option but the dynamics would still need to be considered and most likely, compensated.

5 CONCLUSIONS AND FUTURE WORK

1) A calibration artifact has been developed. Some of the highlights include:

- Stainless steel ring gauge with a 6” ID, 8” OD and a 1” square cross section. The shape of the ring gauge is appropriate for static measurements.
- Swept sine wave feature on the ID and the OD with an amplitude of approximately 5 μ m to simulate small scale features on a part.
- Variable wavelengths of the swept sine wave are for dynamic analyses.
- It can be used to measure the static and dynamic performance of a CMM.

2) The ring gauge artifact was also fabricated. The fabrication technique is as follows:

- Material: A trial artifact was made with aluminum with the final artifact fabricated out of 17-4PH stainless steel and plated with electroless nickel.
- Diamond turning: Each surface of the final ring gauge was diamond turned to produce a flat surface. A 0.5mm radius diamond tool was used on the final artifact on the ID and the OD.

- FTS: The FTS machined the swept sine wave on the ID and OD surfaces of the ring. It was also used for the machining of the ID and the OD surfaces prior to wave fabrication.
- Deconvolution: The method of deconvolution compensated for the dynamics of the FTS prior to fabrication of the swept sine wave and decreased the total fabrication error.

3) Various features of the ring gauge artifact were measured. The resulting measurements were:

- Roundness: The ID of Ring 1 was $0.35\mu\text{m}$ PV. For the OD of Ring 1, it was $0.17\mu\text{m}$ PV. There was slight improvement with Ring 2 with roundness measured on the OD to be $0.12\mu\text{m}$ PV and $0.32\mu\text{m}$ PV on the ID.
- Surface Finish: The surface finish on the top and bottom surfaces of the ring were approximately 37nm RMS which is also true for the ID and the OD. The high surface finish value from a theoretical RMS of 3nm is attributed to machine error and tool damage.
- Wavelength: The desired wavelengths of the OD ranged from 0.447mm to 6.384mm with the ID ranging from 0.479mm to 6.368mm . The actual wavelengths on Ring 1 ranged from 0.439mm to 6.384mm on the OD; the ID had wavelengths from 0.463mm to 6.416mm . For Ring 2, the OD wavelengths were 0.439mm to 6.384mm and the ID was 0.470mm to 6.368mm . The difference is due to the misalignment of the encoder and lack of compensation for LVDT dynamics.

- Amplitude: The desired amplitude of the swept sine wave was $5\mu\text{m}$ or $10\mu\text{m}$ PV. For Ring 1, the PV is $9.63\mu\text{m}$ (3.68% difference) on the OD and $9.80\mu\text{m}$ (1.97% difference) on the ID. For Ring 2, the PV is $9.75\mu\text{m}$ (2.52% difference) on the OD and $9.94\mu\text{m}$ (0.65% difference) on the ID.

4) A measurand was defined in terms of the ring gauge. The uncertainty associated with the “accepted” ring gauge measurement was described.

- The combined uncertainty of the OD is 346nm while it is 321nm for the ID for Ring 1. For Ring 2, the combined uncertainty is 307nm for the OD and 298nm for the ID. These values are constant and in addition to the uncertainty of another measurement.

5) The ring gauge artifact was used to find the dynamics of an LVDT to demonstrate the procedure for determining the dynamics of a CMM.

- The natural frequency occurred $\sim 85\text{Hz}$. 85Hz is where the phase crosses -90° and may be attributed to the filter dynamics of the LVDT. However, the imperfect swept sine wave created errors in finding the actual dynamics.
- The uncompensated dynamics of the LVDT affected the measurement results of the swept sine wave. The wave may be better or worse than described.

For future work, the closed loop controller can be further refined. There is an increase in the expected amplitude at the shortest wavelengths as well as lower amplitude across the rest of the wave. The error in amplitude in the shortest wavelength section is attributed to

higher operating frequencies of the FTS as well as fewer points to define the shape of the wave at the shorter wavelengths. Additional points through increased interpolation or a higher resolution encoder may be necessary to improve the wave. Also, a correctly aligned encoder is imperative for a symmetric swept sine wave.

The algorithm to determine the transfer function of a CMM has a few limiting factors, the primary one being that it is only applicable for one measurement strategy of a CMM. The measurement of the swept sine wave on the ring gauge is performed in one orientation with one particular probe. The errors and their uncertainties will change as the measurement conditions change. The uncertainty analysis of the ring gauge would also be expanded with the addition of more input quantities. One universal transfer function that synthesizes multiple probes and orientations for a particular CMM may be beneficial.

Multiple measurements with different instruments of the fabricated swept sine wave are necessary to accurately define the characteristics of the wave. It is important to understand the dynamics and attributes of an instrument before conclusions are made about a specific measurement.

6 REFERENCES

1. Morse, E. P., *Coordinate Measuring Machines*, ASPE Tutorial, Oct. 24, 2004. Orlando, FL.
2. Lim, C. K., Burdekin, M., *Rapid volumetric calibration of coordinate measuring machines using a hole bar artefact*. Proc. Instn Mech. Engrs, Part B, Journal of Engineering Manufacture, 2002, 216 (B8), p. 1083-93.
3. Chan, F. M. M., Davis, E. J., King, T. G., Stout, K. J., *Some performance characteristics of a multi-axis touch trigger probe*. Meas. Sci. Technol., 1997, 8 (8), p. 837-48.
4. Destefani, J. D., *CMMs make contact*. Manufacturing Engineering, 2001, 127 (3), p. 100-5.
5. Cauchick-Miguel, P. A., King, T. G., *Factors which influence CMM touch trigger probe performance*. Int. J. Mach. Tools Manufact., 1998, 38 (4), p. 363-74.
6. Marino, E. A., *Three-Dimensional Measurement Probe*. Master's Thesis, NC State University, 1999.
7. EMD Sceptre System Proportional Displacement Probe Data Sheet, <http://www.emdsceptre.com/pdprobe.htm>.
8. Bosch, J. A. (ed.), *Coordinate Measuring Machines and Systems*. New York: Marcel Dekker, Inc. 1995.
9. Wong, A., Folkert, K., and Dow, T. A., *Metrology Artifact Development*. Precision Engineering Center Interim Report. October 2003.
10. Weekers, W. G., Schellekens, P. H. J., *Compensation for dynamic errors of coordinate measuring machines*. Measurement, 1997, 20 (3), p. 197-209.
11. Bal-tec The 1216 Ball Plate Data Sheet, <http://www.precisionballs.com/CMM/CMM-28.htm>.
12. Cauchick-Miguel, P., King, T., Davis, J., *CMM verification: a survey*. Measurement, 1996, 17 (1), p. 1-16.

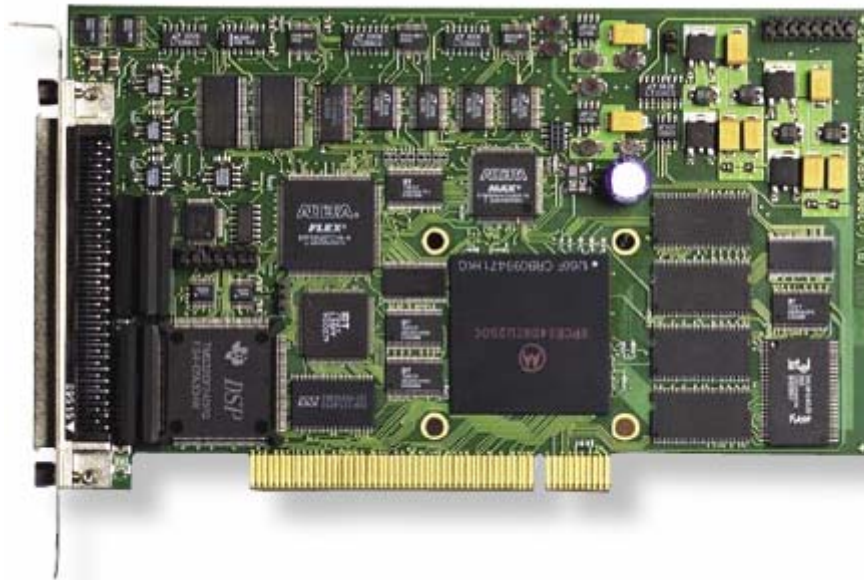
13. Bal-tec Adjustable Ball Bars Data Sheet,
<http://www.precisionballs.com/CMM/CMM-10Page1.htm>.
14. Bal-tec The Geostep 3400-10 Data Sheet,
<http://www.precisionballs.com/CMM/CMM-26Page1.htm>.
15. Lee, E. S., Burdekin, M., *A hole-plate artifact design for the volumetric error calibration of CMM*. Int. J. Adv. Manuf. Technol., 2001, 17 (7), p. 508-515.
16. Silva, J. B. A., Burdekin, M., *A modular space frame for assessing the performance of co-ordinate measuring machines (CMMs)*. Precision Engineering, 2002, 26 (1), p. 37-48.
17. Savio, E., De Chiffre, L., *An artefact for traceable freeform measurements on coordinate measuring machines*. Precision Engineering, 2002, 26 (1), p. 58-68.
18. Jusko, O., Ludicke, F. *Novel Multi-Wave Standards for the Calibration of Form Measuring Instruments*.
19. Panusittikorn, W., *Error Compensation using Inverse Actuator Dynamics*. PhD Dissertation, NC State University, August 2004.
20. Balkey, M.M., Day, R.D., Batha, S.H., Elliot, N.E., Pierce, T., Sandoval, D.L., Garrard, K.P., and Sohn, A., *Production and Metrology of Cylindrical Inertial Confinement Fusion Targets with Sinusoidal Perturbations*. Fusion Science and Technology, Vol 45, No 2, p. 107-112, (2004).
21. ANSI Y14.5M – 1982, *Dimensioning and Tolerancing*. ASME, 1983, New York.
22. Control Tutorials for Matlab,
<http://www.engin.umich.edu/group/ctm/examples/motor/PID2.html>
23. El Wakil, S. D., *Processes and Design for Manufacturing*. New Jersey: Prentice-Hall, Inc. 1989, p. 278.
24. ANSI / NCSL Z540-2-1997 (R2002), *U.S. Guide to the Expression of Uncertainty in Measurement*. NCSL International, 1997, Boulder, CO.
25. Heidenhain Technical Data, *Rotary Encoders and Angle Encoders*.
<http://www.auto-met.com/heidenhain/techdata/phaise2/posmdtm.html>

26. ERO 1300 Rotary Encoders, http://www.auto-met.com/heidenhain/rotary_encoders/rotaryencoders/ERO/ERO1300.htm
27. Heidenhain Technical Data, *Output Signals, TTL*. <http://www.auto-met.com/heidenhain/techdata/phaise2/incos3.html>
28. *DS1104 R&D Controller Board Installation and Configuration Guide*. Germany: dSPACE GmbH, 2003.
29. Macro Sensors, *LVDTs: Tutorial*. http://www.macrosensors.com/ms-lvdt_faq-tutorial.html#howitworks
30. Lion Precision, *Capacitance Gaging Theory*. <http://www.lionprecision.com/theory/index.html>

7 APPENDICES

7.1 APPENDIX A – EQUIPMENT SPECIFICATIONS

7.1.1 dSPACE 1104 R&D Controller Board



Technical Details

Processor	PowerPC Type	<input type="checkbox"/> PPC603e
	CPU clock	<input type="checkbox"/> 250 MHz
	Cache	<input type="checkbox"/> 2 x 16 KB
Memory	Global memory	<input type="checkbox"/> 32 MB SDRAM
	Flash memory	<input type="checkbox"/> 8 MB
Timer	4 general-purpose timers	<input type="checkbox"/> 32-bit down counter <input type="checkbox"/> Reload by software <input type="checkbox"/> 80-ns resolution
	1 sampling rate timer (decrementer)	<input type="checkbox"/> 32-bit down counter <input type="checkbox"/> Reload by software <input type="checkbox"/> 40-ns resolution
	1 time base counter	<input type="checkbox"/> 64-bit down counter <input type="checkbox"/> 40-ns resolution
Interrupt controller		<input type="checkbox"/> 5 timer interrupts <input type="checkbox"/> 2 incremental encoder index line interrupts <input type="checkbox"/> 1 UART interrupt <input type="checkbox"/> 1 slave DSP interrupt <input type="checkbox"/> 1 slave DSP PWM interrupts <input type="checkbox"/> 5 A/D converters (end of conversion interrupts) <input type="checkbox"/> 1 host interrupt <input type="checkbox"/> 4 external interrupts (user interrupts)
A/D converter	Channels	<input type="checkbox"/> 4 multiplexed channels equipped with one 16-bit sample & hold A/D converter <input type="checkbox"/> 4 parallel channels each equipped with one 12-bit sample & hold A/D converter
	Resolution	<input type="checkbox"/> Multiplexed channels: 16 bit <input type="checkbox"/> Parallel channels: 12 bit
	Input voltage range	<input type="checkbox"/> ± 10 V
	Conversion time	<input type="checkbox"/> Multiplexed channels: 2 μ s <input type="checkbox"/> Parallel channels: 800 ns
	Offset error	<input type="checkbox"/> ± 5 mV
	Gain error	<input type="checkbox"/> Multiplexed channels: $\pm 0.25\%$ <input type="checkbox"/> Parallel channels: $\pm 0.5\%$
	Offset drift	<input type="checkbox"/> 4 ppm/K
	Gain drift	<input type="checkbox"/> 25 ppm/K
	Signal-to-noise-ratio	<input type="checkbox"/> Multiplexed channels: > 80 dB

D/A converter	Channels Resolution Output range Settling time Offset error Gain error Offset drift Gain drift Signal-to-noise-ratio I _{max} C _{lmax}	<input type="checkbox"/> Parallel channels: >65 dB <input type="checkbox"/> 8 channels <input type="checkbox"/> 16-bit <input type="checkbox"/> ±10 V <input type="checkbox"/> Max. 10 µs (full-scale) <input type="checkbox"/> ±1 mV <input type="checkbox"/> ±0.1% <input type="checkbox"/> 13 ppm/K <input type="checkbox"/> 25 ppm/K <input type="checkbox"/> >80 dB <input type="checkbox"/> ±5 mA <input type="checkbox"/> 10 nF
Digital I/O	Channels Voltage range I _{outmax}	<input type="checkbox"/> 20-bit parallel I/O <input type="checkbox"/> Single bit selectable for input or output <input type="checkbox"/> TTL input/output levels <input type="checkbox"/> ±10 mA
Digital Incremental encoder interface	Channels Position counters	<input type="checkbox"/> 2 independent channels <input type="checkbox"/> Single-ended (TTL) or differential (RS422) input (software programmable for each channel) <input type="checkbox"/> 24-bit resolution <input type="checkbox"/> Max. 1.65 MHz input frequency, i.e., fourfold pulse counts up to 6.6 MHz <input type="checkbox"/> Counter reset or reload via software
Serial interface	Encoder supply voltage Configuration Baud rate	<input type="checkbox"/> 5 V/0.5 A <input type="checkbox"/> Single UART (universal asynchronous receiver and transmitter) with FIFO <input type="checkbox"/> RS232/RS422/RS485 compatibility <input type="checkbox"/> Up to 115.2 Kbaud (RS232) <input type="checkbox"/> Up to 1 Mbaud (RS422/RS485)
Slave DSP	Type Clock rate Memory I/O channels Input voltage range Output current	<input type="checkbox"/> Texas Instruments TMS320F240 DSP <input type="checkbox"/> 20 MHz <input type="checkbox"/> 64Kx16 external code memory <input type="checkbox"/> 28Kx16 external data memory <input type="checkbox"/> 4Kx16 dual-port memory for communication <input type="checkbox"/> 32 KB flash memory <input type="checkbox"/> 16 A/D converter inputs <input type="checkbox"/> 10 PWM outputs <input type="checkbox"/> 4 capture inputs <input type="checkbox"/> 2 serial ports <input type="checkbox"/> TTL input/output level <input type="checkbox"/> A/D converter inputs: 0 ... 5 V <input type="checkbox"/> Max. ±13 mA
Host interface Physical characteristics	Physical size Ambient temperature Cooling Power consumption Power supply	<input type="checkbox"/> Requires one 33 MHz / 32-bit 5-V PCI slot <input type="checkbox"/> 178 x 107 mm (7.0 x 4.2 in) <input type="checkbox"/> 0 ... 55 °C (32 ... 131 °F) <input type="checkbox"/> Active cooling by fan <input type="checkbox"/> 18.5 W <input type="checkbox"/> +5 V ±5%, 2.5 A <input type="checkbox"/> +12 V ±5%, 0.3 A <input type="checkbox"/> -12 V ±5%, 0.2 A



Connector panel.



Connector/LED combi panel.

7.1.2 Rotary Encoder

The current encoder on the DTM is a Heidenhain ERO 1324, 5000 line rotary encoder. It consists of a graduated disk with hub and a scanning unit. The scanning unit is mounted from the side to permit installation on a through shaft (Figure 7-1).

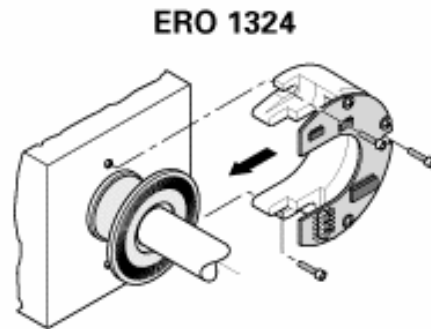


Figure 7-1. Side mounting of rotary encoder [25]

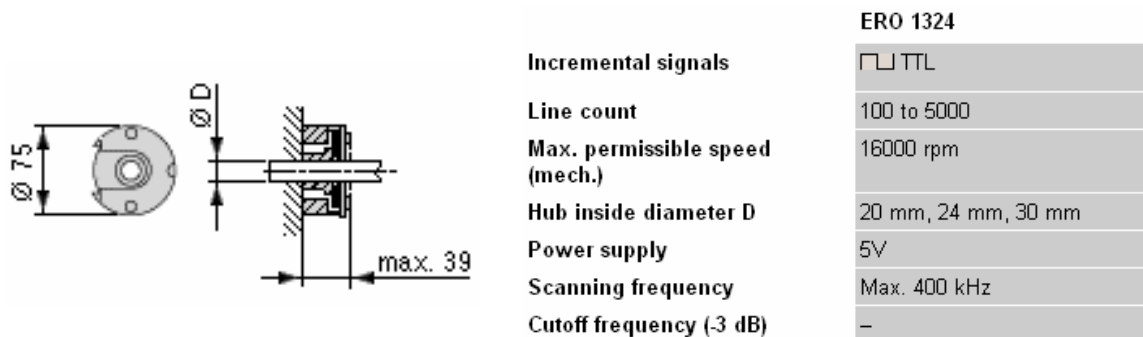


Figure 7-2. Schematic and specifications of rotary encoder [26]

The TTL output signal is a combination of two sinusoidal scanning signals digitized into two square waves (or pulse trains), phase shifted by 90° , and a reference pulse. The reference pulse is gated with the incremental signals. It resets the line count of the encoder. The inverse of each signal of all square wave pulse trains is also generated. The distance between two successive edges of the combined pulse trains is one measuring step [27].

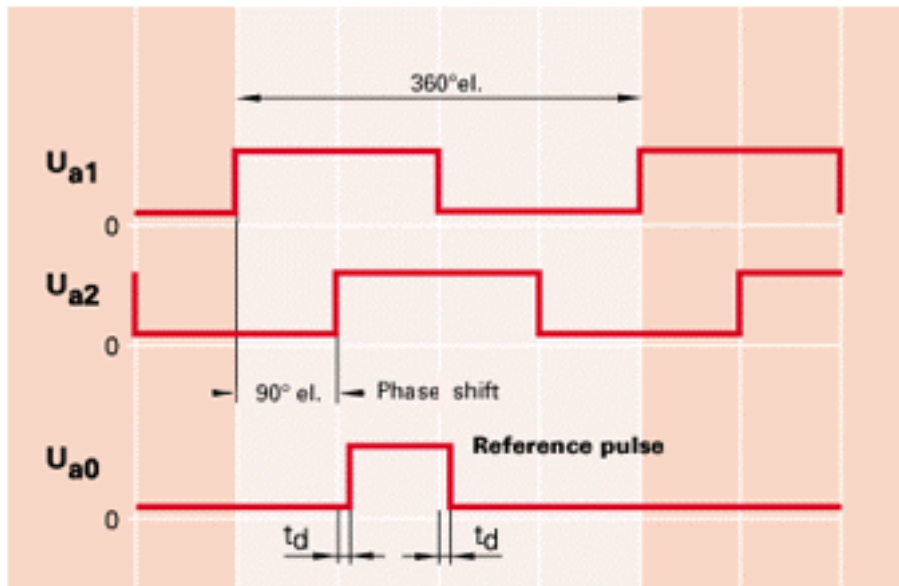


Figure 7-3. TTL incremental signals [27]

One line count corresponds to four edges between the two waves. With a 5,000 line count rotary encoder, there are 20,000 individual counts or divisions. Each of these counts is assigned a value in the look-up table for the fabrication of the swept sine wave. dSPACE provides the 5V power supply and records the individual counts and the reference pulse, or index reset. The incremental encoder interface connector indicates signals assigned to each pin.

Connector (CP19, CP20)	Pin	Signal	Pin	Signal
	1	VCC (+5 V)	9	VCC (+5 V)
	2	PHI0(x)	10	GND
	3	/PHI0(x)	11	GND
	4	PHI90(x)	12	GND
	5	/PHI90(x)	13	GND
	6	IDX(x)	14	GND
	7	/IDX(x)	15	GND
	8	GND		

Figure 7-4. 15-pin, female Sub-D connectors located on the front of the controller panel

[28].

Pins 2 and 3 correspond with one pulse train and its inverse. Pins 4 and 5 are the other pulse train and its inverse shifted 90° from the first wave. Pins 6 and 7 correlate to the reference pulse and its inverse.

7.1.3 Capacitance Gage

A capacitance (cap) gage is used to measure displacement by registering the change in capacitance between two parallel conductive plates. An electric charge is stored on each plate; when a voltage is applied to one of them, an electrical field is formed as a result of the difference between these charges. When using a cap gage, the sensor surface is the plate where voltage is applied, while the object to be measured (the target) is the other plate. The voltage on the sensor surface is constantly being changed by its electronics; the amount of current to cause the change indicates the amount of capacitance between the sensor and the target [30].

The amount of capacitance (C) is determined by the area of the plates, the distance between the plates (gap), and the dielectric material. Equation (1) defines the relationship between these factors [30].

$$C = \frac{\text{Area} * \text{Dielectric}}{\text{Gap}} \quad (1)$$

The dielectric material is usually air with the size of the sensor and the size of the target remaining constant during measurement. Since the gap distance is the only variable, Equation (1) can be reduced to Equation (2) [30].

$$C = \frac{1}{\text{Gap}} \quad (2)$$

The manufacturer calibrates the cap gage to assign an output voltage for each corresponding change in capacitance. This voltage is directly related to the variation in gap distance. The change in output voltage relative to gap distance indicates the

sensitivity of the sensor [30]. For the cap gage used in the FTS, the sensitivity factor is 1 V/ μm .

The construction of the cap gage probe affects the accuracy of the displacement measurement. There are multiple electrical fields created when a voltage is applied to a conductor. For the sensor to record an accurate reading, the probe must be shielded or guarded to focus the electrical field [30]. Figure 7-5 illustrates the construction.

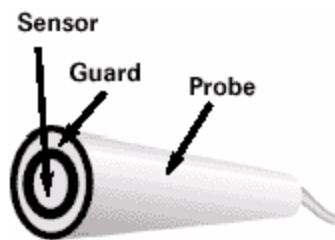


Figure 7-5. Construction of a capacitance gage probe [30]

Measurement accuracy is also affected by target size, target shape, surface finish of the target, parallelism, and the environment. The target material is not a concern as long as it is conductive [30].

Target Size: By focusing the electrical field with the guard, the projected field on the target may grow up to 30%, depending on the size and shape of the guard. Therefore, the target size must be at least 30% larger than the sensor size to prevent any wrapping of the electrical field onto the sides of the target and to decrease the probe's sensitivity to location relative to the target [30].

Target Shape: The cap gage is calibrated using a flat target surface. Since the probe averages the gap distance, the displacement reading at zero volts will change from the calibrated gap with any target surface whose shape is not flat. The electrical field will also act differently [30].

Surface Finish: The system averages the gap over the surface covered by the spot size of the sensor. A rough surface or non-uniform surface finish will cause various readings as the sensor is moved across the target surface[30].

Parallelism: Any tilt in the surface of the target elongates the spot size of the sensor. The spot size alteration changes how the field between the plates interacts [30]. However, if the cap gage was tilted during calibration and then is used with the same tilt, the measurement will be repeatable but with a smaller available measurement range.

Environment: The cap gage system used with the FTS was designed to compensate for temperatures ranging from 22°C - 35°C (72°F - 95°F). This translates to errors of less than 0.5% of full scale. The target and measurement fixture materials will expand and contract within this temperature range which will cause a change in the gap. Humidity will also affect the dielectric constant. It is important that temperature and humidity be controlled during measurement [30].

Figure 7-6 provides dimensions and an image of the actual probe used in the FTS. Figure 7-7 furnishes the calibration certificate from Lion Precision with specifications.

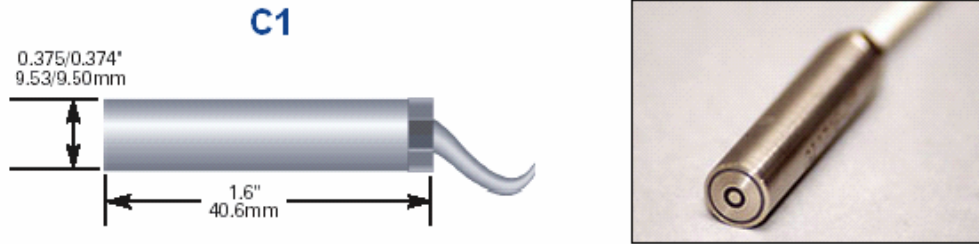


Figure 7-6. Cap gage probe with dimensions

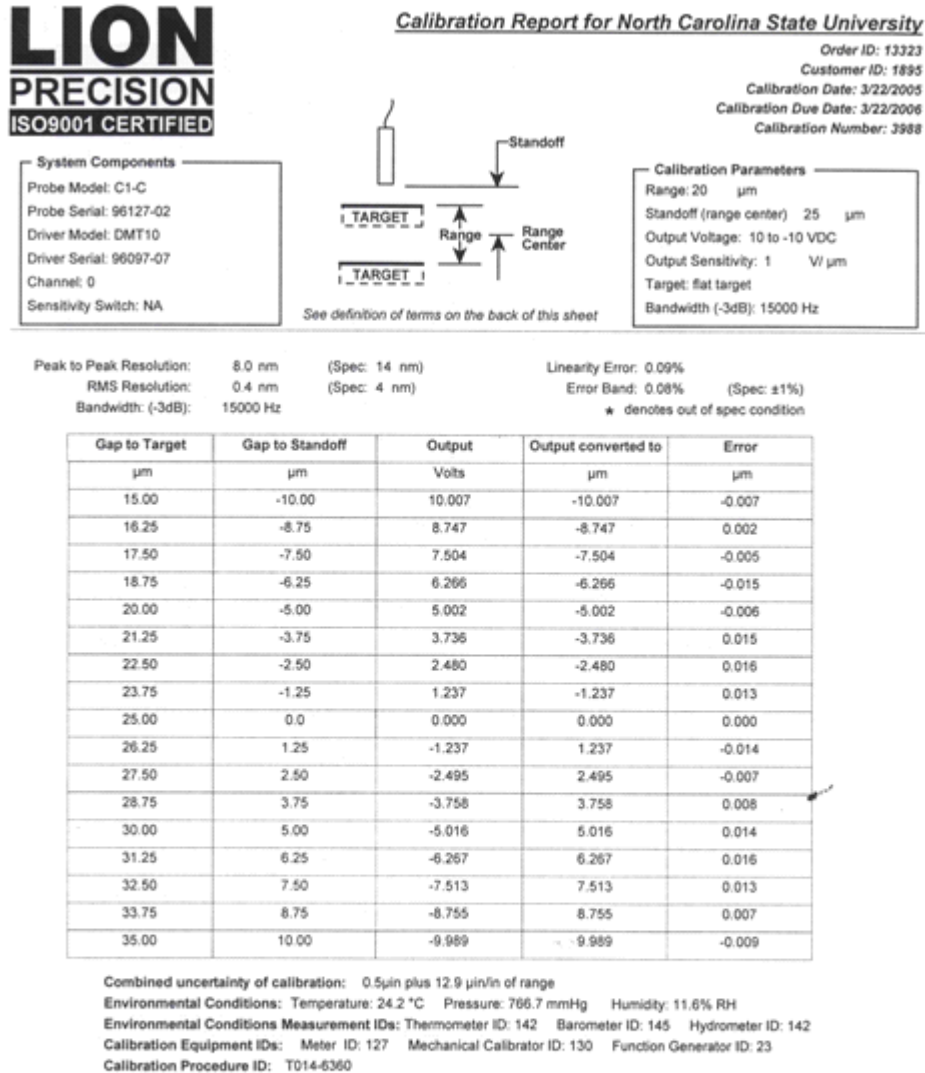


Figure 7-7. Cap gage calibration certificate

7.1.4 Fast Tool Servo

An 18 mm long, hollow cylindrical piezoelectric actuator (25 mm OD and 12 mm ID) drives the device to a maximum displacement of 18 μm . A capacitance gage provides feedback on the position of the tool holder by observing the movement of the base plate through the hollow actuator. A commanded position is turned into a positive input voltage and sent to a high voltage amplifier where it is amplified by 100 before being sent to the FTS.

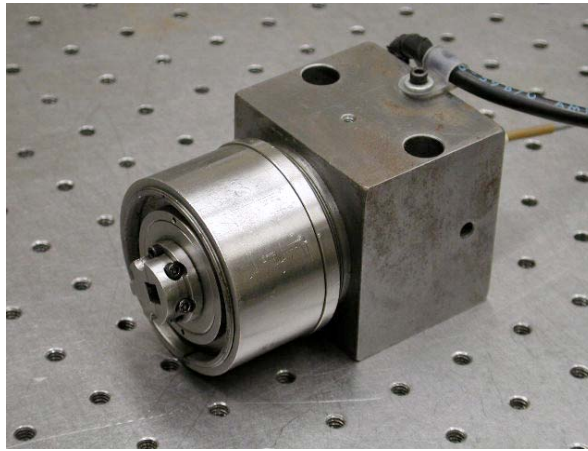


Figure 7-8. The fast tool servo without the tool shown

FTS

Fast Tool Servo

Application: Forming low-amplitude, high frequency features, on optical surfaces.

Range: 25 μm or 40 μm (25 mm or 40 mm Piezo stack)

Bandwidth: 1 kHz

Feedback: Capacitance Gauge (ADE MicroSense v3401 or Lion Precision DMT 10)

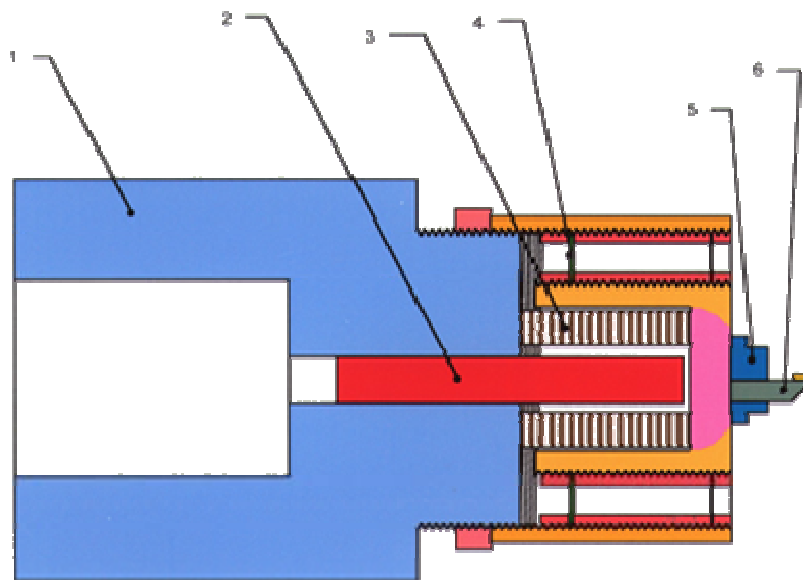
Controller: Real-time feedback 10 kHz custom-built DSP Controller using TI TMS 320

Stiffness: 400 N/ μm

Resolution: 5 nm (25mm Piezo)

12 nm (40mm Piezo)

Surface Finish: 5nm rms (OFHC Copper with a 10 Hz sine wave)



1. Mounting Body 2. Capacitance Gauge 3. Piezo Stack 4. Preload Flexure
5. Tool Holder 6. Tool.

Figure 7-9. Cross section of the FTS with specifications

7.1.5 Linear Variable Differential Transformer (LVDT)

The LVDT is a common form of a variable inductance transducer that converts linear motion into an output voltage. It consists of three coils – one primary winding centered between two identically wound secondary windings. The core moves freely within the hollow bore and is mechanically coupled to the object being measured via an air bearing [29].

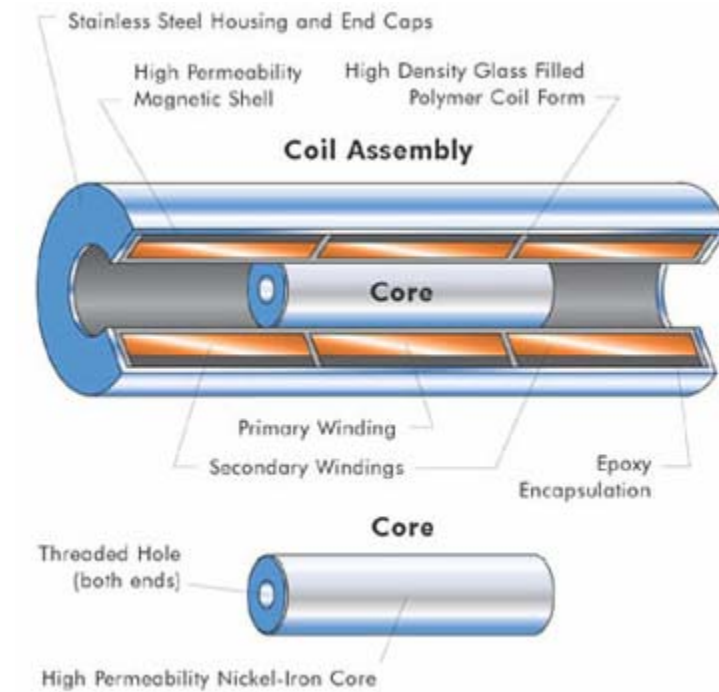


Figure 7-10. Coil assembly of a LVDT [29]

The primary winding (P) is energized by an external AC power source, referred to as the primary excitation. Its output signal is the differential AC voltage between the secondary windings (S1 and S2) and varies with the position of the core. The magnetic flux created by the primary excitation couples the core with the secondary windings. More flux is coupled to one secondary winding than the other as the core is moved closer to it. When the core is in its null position, the flux is equal, creating an essentially zero output

voltage. The top diagrams of Figure 7-11 show how the output magnitude changes with the position of the core.

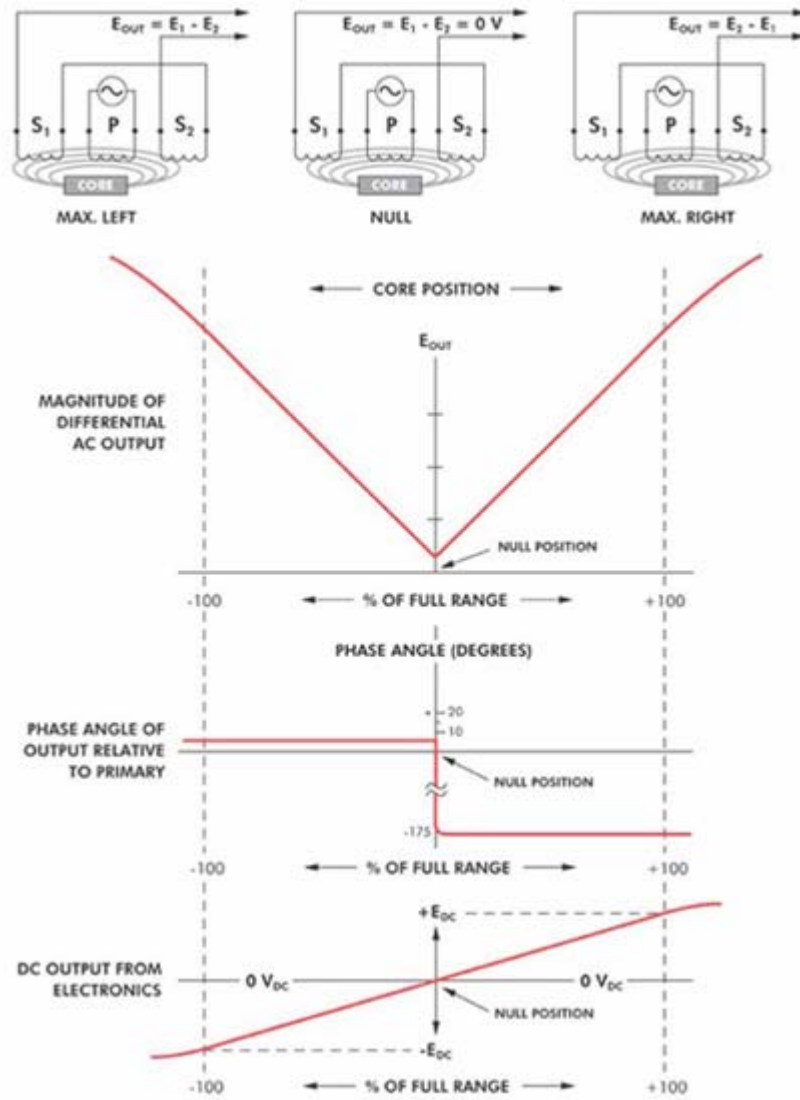


Figure 7-11. LVDT output based on the position of the core [29]

The phase angle of the excitation voltage quickly changes by 180° as the center of the core passes through the null position. The change in phase angle determines the direction of the core and thus will translate to a (+) or (-) DC output voltage. Also note that the LVDT can operate above its full range, but its response is no longer linear [29].

7.1.6 Torque Wrench¹¹

Torque, a measure of turning or twisting force, is calculated by multiplying force by distance. To get the best performance from the torque tool, it should be held by the handle grip and pulled slowly and evenly.

Selecting the Correct Torque Range - For the most accurate performance, the maximum torque applied should fall near the middle of the tool's torque range. For example, if applying 50 ft.-lbs. of torque, it would be better to choose a wrench with a range of 5 to 100 ft.-lbs., rather than a range of 5 to 50 ft.-lbs.

Accuracy - Accuracy is usually given for 20-100% of a tool's torque range. For example, if the torque range is 20 to 120in-lbs, the accuracy statement is true for measurements between 40 and 120in-lbs. Below 20% of the torque range, the tool's accuracy often drops off significantly.

A dial torque wrench with a dual scale has been selected. The body is steel and the handle has a cushion grip. Its overall length is 11 ½” with a ¼” square drive. The wrench torques clockwise and counterclockwise; accuracy in both directions is ±4% of torque reading for 20-100% of torque range. The torque range is 0 to 15in-lbs (0 to 1.8Nm) with 0.25in-lb (0.05Nm) graduations.

¹¹ Information provided by McMaster-Carr at <http://www.mcmaster.com>



Dual Scale

Figure 7-12. Dual scale torque wrench from CDI

CDI TORQUE PRODUCTS

Certificate of Calibration

Model no.	151LDIN	Serial Number	0804816449
Type	Dial Wrench	Calibration equipment	CDI Multitest P0077A-BI
Range	3.00 in-lb - 15.00 in-lb	Accuracy of calibration	±0.25%
Manufacturer	CDI		

Set Torque [in-lb]	Readings [in-lb]		
Clockwise torque (Tolerance: ± 3.0%)			
3.00	2.99 -0.3%	2.94 -2.0%	2.94 -2.0%
9.00	8.98 -0.2%	8.88 -1.3%	8.94 -0.7%
15.00	15.18 1.2%	15.05 0.3%	15.12 0.8%
Counterclockwise torque (Tolerance: ± 3.0%)			
3.00	2.97 -1.0%	2.95 -1.7%	2.99 -0.3%
9.00	8.85 -1.7%	8.89 -1.2%	8.86 -1.6%
15.00	14.92 -0.5%	14.82 -1.2%	14.95 -0.3%

Result: Measured values are within tolerance according to :ASME B107.14M-1994

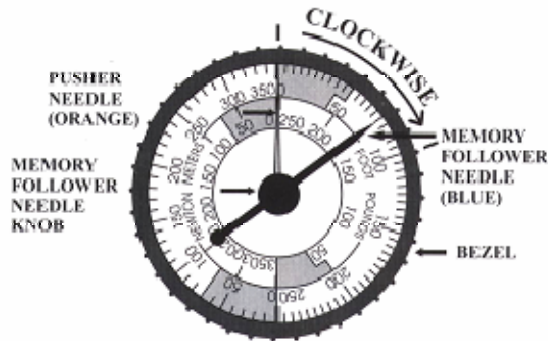
Date: **OCT 13 2004** Operator: Jose De Horta Supervisor: Ricardo Sevilla

Calibration is performed by comparison with reference standards which have been calibrated by a recognized NIST-laboratory and are therefore traceable to the National Institute of Standards and Technology. The issuer of this certificate bears sole responsibility for calibration and documentation thereof. Duplication of this certificate or parts hereof is prohibited. The manufacturer recommends that the calibration be checked at the earlier of 6 months or 5,000 cycles, after the date the torque wrench is put in service.

DATE WRENCH PUT IN SERVICE: _____

Figure 7-13. Dial torque wrench calibration certificate

SETTING MEMORY FOLLOWER NEEDLE ON DUAL SCALE MODELS



Follower Needle Dial

Before using all models of dial torque wrenches, it is strongly suggested to cycle/operate them 3 times at full scale in the torque direction in which they will be used. *Dial torque wrenches must always be zeroed before use.*

To set orange pusher & blue follower needle for right-hand (C W) torquing:

To set orange pusher & blue follower needle for right-hand (C W) torquing:

1. Turn bezel in left-hand (CCW) direction until, blue memory follower needle contacts orange pusher needle.
2. Continue to turn bezel left-hand (CCW) until blue memory follower needle is lined up with *zero* (0) of outer graduation on portion of dial for IN.LB., FT.LB., METRIC readings.
3. Apply force on the wrench handle until blue follower needle reaches desired torque. When force is released orange pusher needle will return to *zero* and blue memory follower needle will remain at torque applied.
4. For repetitive torque operations (once the *zero* has been set as instructed above), the blue memory follower needle can be returned to *zero* by use of the follower needle knob. It is ready for the next operation.
5. IMPORTANT - When using the memory feature always make sure that the blue follower memory needle is on *zero* before torquing.

Figure 7-14. Instructions on use from CDI Operation Manual

7.2 APPENDIX B – LABVIEW CAPTURE OF TRANSFER FUNCTION¹²

The closed loop transfer function of the FTS was found using a LabView program to sweep through frequencies. The voltage output was sent through dSPACE to record the response of the closed loop system.

The equipment used to connect LabView to dSPACE is as follows:

- 1 Computer with LabView including an installed Data Acquisition Board (National Instruments E Series PCI-6052E)
- 1 SCB-68 connector block (Figure 7-15)
- 1 Shielded National Instruments 184749-01 cable
 - Joins SCB-68 to the Data Acquisition Board
- 2 Cables with a BNC on one end and stripped on the other end
 - On the stripped end, the cable separates into 2 separate entities: a thick bundle of wires and a thin bundle of wires

¹² Thanks to Anthony Wong for his LabView expertise and his development of a usable procedure to capture the transfer function of the FTS

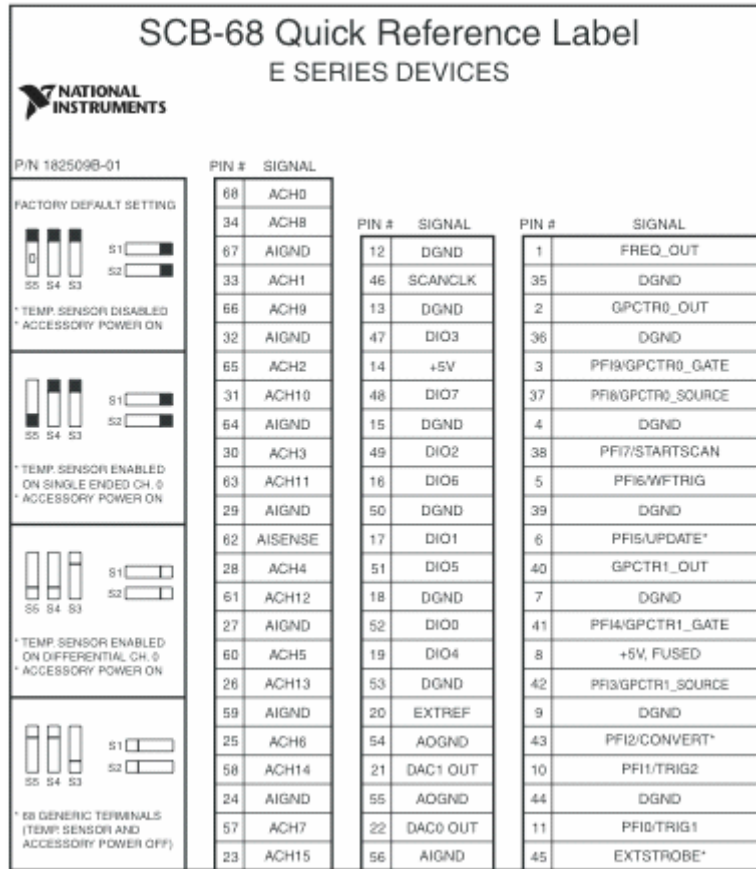


Figure 7-15. Pinout of the SCB-68 connector block

Wires and cables are interfaced to the SCB-68 connector block:

- Red-taped cable:
 - thin → pin 67 (AIGND)
 - thick → pin 33 (ACH1)
 - BNC → Cap gage output port on dSPACE (ADC #5)
- Yellow-taped cable:
 - thin → pin 54 (AOGND)
 - thick → pin 22 (DAC0 OUT)
 - BNC → FTS input port on dSPACE (DAC #2)
- Solid wire:
 - pin 22 (DAC0 OUT) → pin 68 (ACH0)
- Solid wire:
 - pin 55 (AOGND) → pin 24 (AIGND)

Once the SCB-68 connector block has been configured, the LabView program “System_ID_v2.vi” is opened. The front panel, or graphical interface, controls the program inputs (Figure 7-16). The user specifies the amplitude of the wave, the sampling frequency of the program in Hz, the starting frequency of the sweep, the ending frequency of the sweep, the number of steps between the starting and ending frequency, and the DC offset. The value of the DC offset is larger than the amplitude to create an entirely positive wave because the HV amplifier and the FTS cannot handle a negative voltage. While the program runs, the user can view the signal in either the time domain or the frequency domain by selecting the corresponding tab.

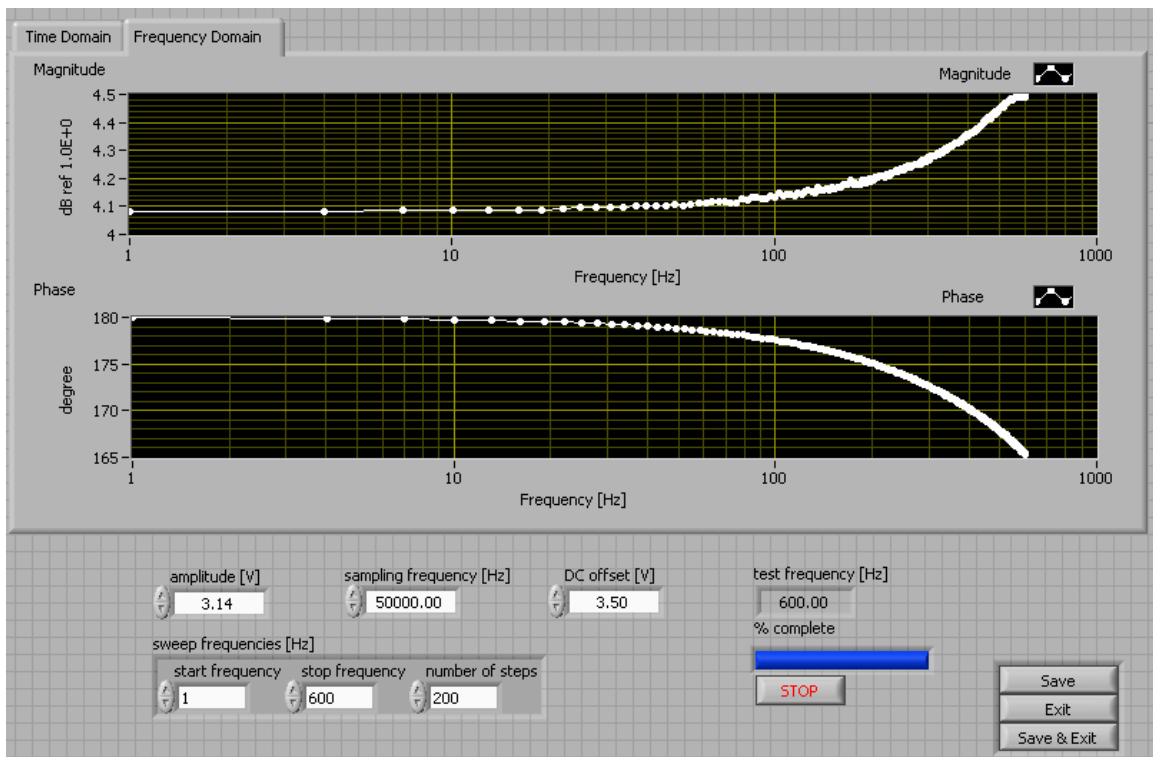


Figure 7-16. “System_ID_v2.vi” front panel

The signal from LabView is sent to the dSPACE board to filter through the closed loop controller before being input into the FTS. Figure 7-17 illustrates the Simulink model used in dSPACE.

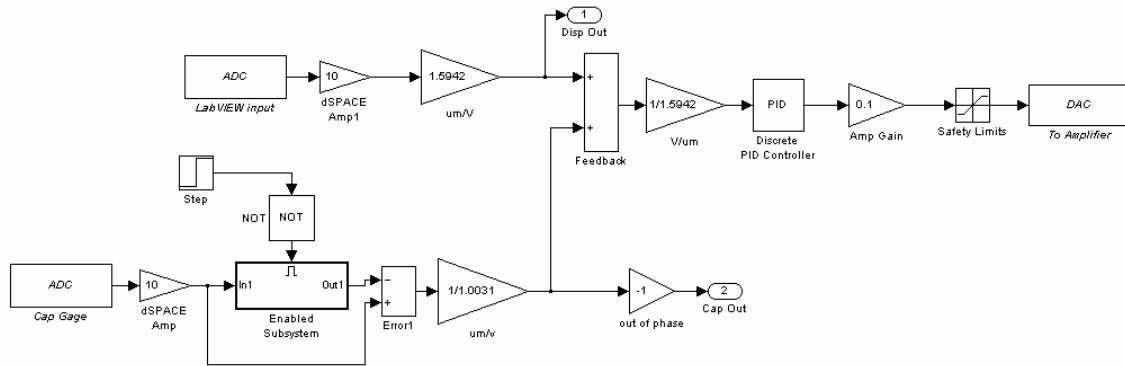


Figure 7-17. Simulink model of the closed loop controller with the LabView input

LabView saves the data as a text file with the frequency and the real and imaginary components. Figure 7-18 shows a sample of the file with the generated header and the frequency response data. This data is transferred to Matlab for further use in the deconvolution algorithm.

```

FTS_3V_800Hz.txt - Notepad
File Edit Format View Help
//Frequency Response Data
//Header
//Serial Number: 0
//Actuator Type: FTS
//Measurement Type: Cap Gauge
//Date: 3:05 PM Wednesday, October 13, 2004
//Gain (mm/V): 0.000000
//Maximum Displacement (mm): 0.000000
//Maximum Velocity (mm/s): 0.000000
//Maximum Acceleration (mm/s**2): 0.000000
//Number of Amplitudes: 1
//*****
//Amplitude Subheader
//Amplitude of Excitation (mm): 0.060000
//Sample Rate (Hz): 50000.000000
//Number of Frequencies: 399
//Freq (Hz)      Real      Imaginary
2.0000000000    -1.6001455013    0.0012882636
4.0050251256    -1.6002004738    0.0025544979
6.0100502513    -1.6004230355    0.0038409834
8.0150753769    -1.6005740712    0.0050451878
10.0201005025   -1.6008820216    0.0064867705
12.0251256281   -1.6008811722    0.0077513907
14.0301507538   -1.6010221306    0.0091707852
16.0351758794   -1.6012413374    0.0104752353
18.0402010050   -1.6012933958    0.0115297711
20.0452261307   -1.6014496951    0.0130766547
22.0502512563   -1.6016348565    0.0145352131
24.0552763819   -1.6020374159    0.0158242451
26.0603015075   -1.6018458127    0.0164749066
28.0653266332   -1.6021161469    0.0184882183

```

Figure 7-18. Sample of data saved by LabView

7.3 APPENDIX C – DTM SPINDLE SPEED CONTROL

The ASG2500 Diamond Turning Machine (DTM) used for the final fabrication of the steel artifact uses open loop control to command the rotational speed of the spindle. The computer controller allows the user to type in a spindle speed with the direction of rotation. However, at lower spindle speeds, the error in actual spindle speed versus commanded spindle speed can be greater than 10%. The fabrication of the swept sine wave on the surfaces of the ring uses a spindle speed of 20 RPM. The values generated for the lookup table are based on this spindle speed. Any difference in speed will cause phase error in the overall wave feature.

The simple solution suggests that the user type in a larger spindle speed to compensate for the lower actual speed of the spindle. However, due to the integer nature of the speed command, the 20 RPM value will never be exact. Figure 7-19 demonstrates the commanded and actual values in each direction.

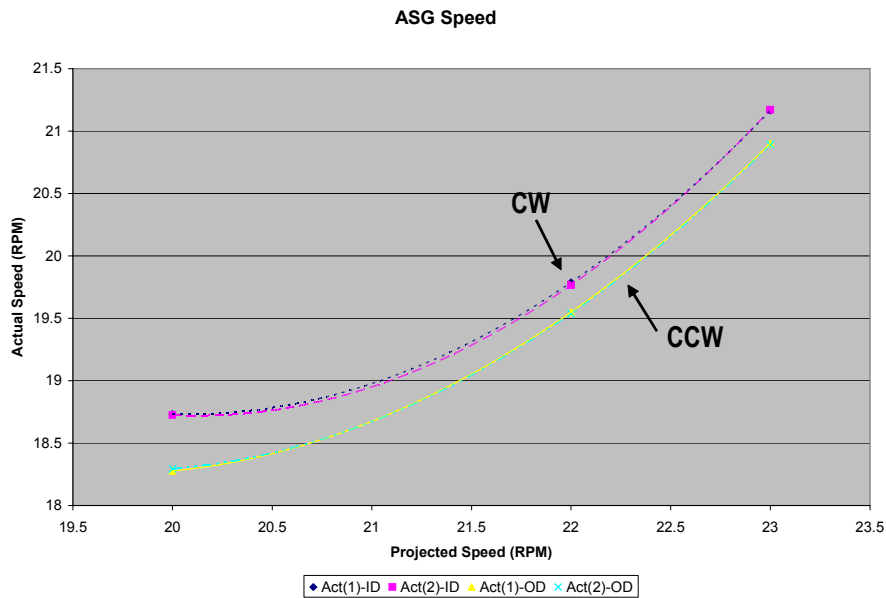


Figure 7-19. x-axis is commanded speed while y-axis is the actual speed

Another fact to note is that the actual speed is dependant on the direction of rotation of the spindle. Due to these uncertainties, the DTM spindle speed will be controlled using closed loop control.

The DTM spindle uses a 20,000 count rotary encoder. Each individual count corresponds to a rotational position of the spindle. After each complete rotation of the spindle, the index on the encoder resets to cause the encoder to begin counting up or down from zero, depending on the direction of rotation. By reading the encoder values, the speed can be controlled. However, to control velocity, the encoder counts have to be converted. Instead of reading incremental counts, the difference in each count may be captured. The output value of the delta position capture will either be 0 or 1, depending on the sampling rate of the dSPACE model. A faster sampling rate than there are available counts causes multiple 0's or 1's in a row. So, these values cannot simply be averaged as a whole; rather, a moving average becomes necessary.

One of the ways to implement a moving average is to use a Finite Impulse Response (FIR) filter. The filter captures a number of input values equal to the order of the filter. Each value is multiplied by a constant which specifies an output range of values or band. The equation below represents the filter equation.

The diagram shows the equation $y[n] = \sum c[k] * x[n-k]$ with three arrows pointing to its components: 'Output' points to $y[n]$, 'previous input' points to $x[n-k]$, and 'coefficients' points to $c[k]$.

$$y[n] = \sum c[k] * x[n-k]$$

The FIR filter used in the dSPACE model uses the same value (0.01) for all the filter coefficients.

To properly design a closed loop controller, the open loop response of the system should be found. A step input of 0.1V was commanded into the system. The encoder delta values were captured and fed through the filter where the output was converted to a voltage for comparison to the input. The open loop step response is shown in Figure 7-20.

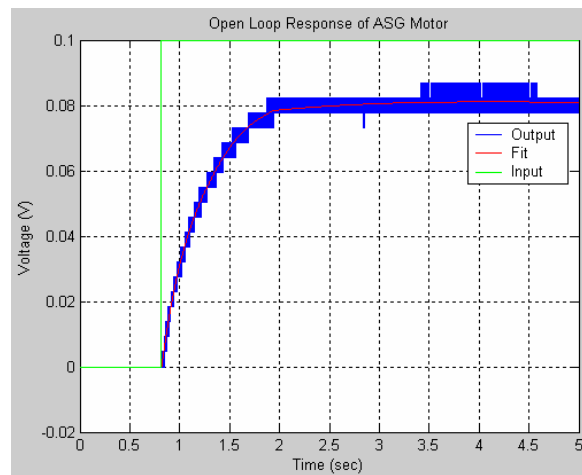


Figure 7-20. Motor open loop step response

The characteristics of the motor were modeled in Matlab to allow for the safe design of a PID controller without having to worry about damaging the motor. The open loop transfer function of a DC motor is shown in Equation 3.

$$\frac{\dot{\theta}}{V} = \frac{K}{(Js + b)(Ls + R) + K^2} \quad (3)$$

where J is the moment of inertia of the rotor

b is the damping ratio of the mechanical system

K is electromotive force constant

R is the electric resistance

L is the electric inductance [22]

The modeled system compares closely to the actual system response. Figure 7-21 demonstrates this comparison.

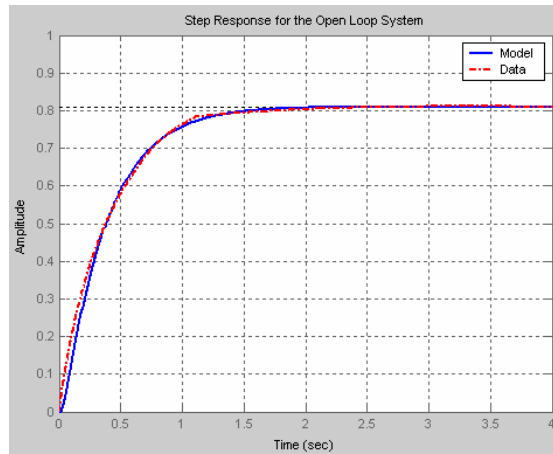


Figure 7-21. Verification of modeled system

After modeling the motor, PID control can readily be implemented for closed loop control. The original system consists of two negative real poles that exhibit a stable system. The closed loop controller is also stable with all poles and zeros on the left side of the pole-zero map. Figure 7-22 shows the step response of the closed loop and open loop system with the pole-zero map.

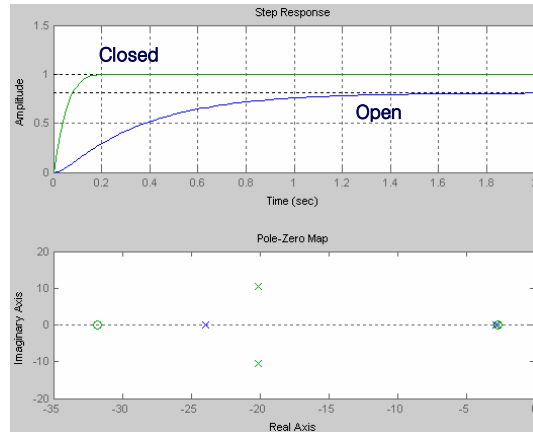


Figure 7-22. Step response of both systems

The closed loop speed control of the DTM was implemented in dSPACE. Figure 7-23 shows the comparison between the open loop control using the DTM controller (red) and the closed loop control using dSPACE (blue). With dSPACE, the encoder counts vary by only ± 2 counts whereas the encoder counts in open loop control vary by ± 20 counts.

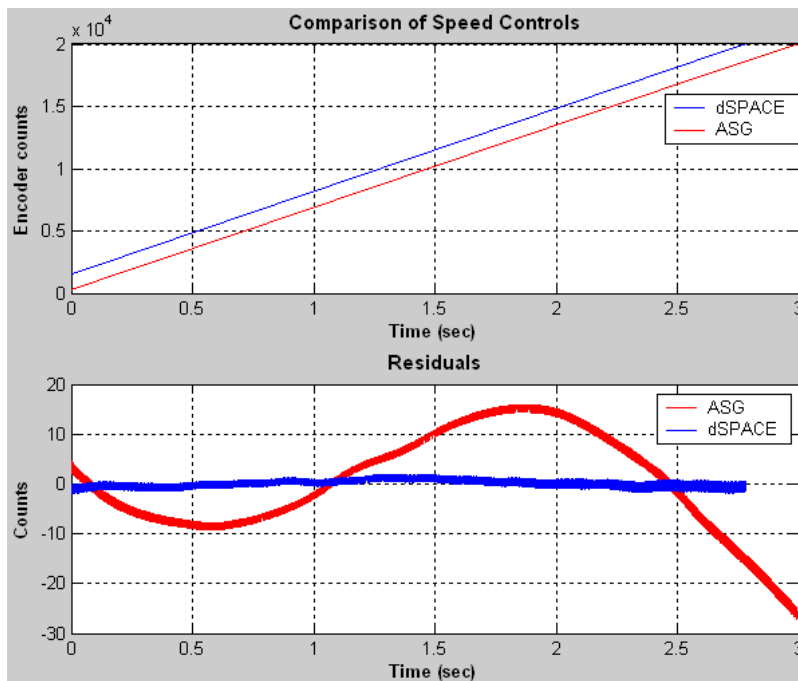


Figure 7-23. Speed control comparison after implementation

7.4 APPENDIX D – MATLAB PROGRAMS

7.4.1 Swept Sine Wave

MATLAB file: sweep.m

```
% Generate a linearly modulated (amplitude and frequency) swept sine wave
% [t,s,su,sd,sp,cv,wv] = sweep(A,b,L,f,d,N)
% [t,s,su,sd,sp,cv,wv] = sweep(N)
% Input
% A starting signal amplitude (mm)      (default = 0.0025)
% b amplitude modulation delta          (default = 0)
% L length of distance vector t        (default = 152.4*pi/4)
% f base frequency                      (default = 10)
% d linear modulation parameter         (default = 200)
% N number of samples to generate      (default = 10000)
% Output
% t vector of distance samples (time or space)
% s vector of wave samples
% su increasing sweep over 1st, 3rd quadrants of L
% sd decreasing sweep over 2nd, 4th quadrants of L
% sp slope along the wave (radians)
% cv curvature along the wave (1/length units)
% wv wave spacing vector (length units)
% distance between zero crossings
%
% The sinusoidal sweep is performed 4 times: up, -down, up, -down to construct a signal
% that is continuous and repeating with period 4*L. The amplitude of the swept wave is
% linearly modulated between A and A-b. If b is positive, the wave amplitude will
% decrease linearly with increasing frequency. A negative value for b will result in a
% linearly increasing wave amplitude as the frequency increases. The sampling
% resolution is 4*L/N. Local slopes are calculated as the arctangent of the rate of change
% of successive values in s. Curvature is approximated using finite differences to
% calculate the change in slope with respect to arc length along the wave. Wave spacing
% is determined by finding the distance between points in the signal vector where the
% sign has changed (- to +, or + to -). An exact zero is treated as a positive value.
%
% For the ring gauge ID,
% [t,s,su,sd,sp,cv,wv] = sweep(0.005,0,152.4*pi/4,16,110,20000)
% This gives a 5µm amplitude wave over a length of 478.7308 mm. The maximum
% slope is 3.51 degrees (0.061 radians), the maximum curvature is 0.7574 (R=0.9605)
```

```

% and the wavelength ranges from 0.4788 to 6.3678mm.
%
% The freq() function can be used to analyze the frequency content of the waveform
% generated by sweep(). If a scale parameter is specified, freq() expresses the harmonics
% of the signal in terms of spatial wave number (= 1/wavelength) instead of temporal
% frequency.
%
% For the ring gauge,
% [f,mag,phase,fq]=freq(s,20000/(152.4*pi),1e-10,(152.4*pi)/4)
% In this case the sample rate parameter is the total number of samples divided by the
% mean circumference of the ring and the scale factor is equal to the length parameter.
% The common factor of (152.4*pi) can be eliminated,
% [f,mag,phase,fq]=freq(s,20000,1e-10,1/4)

```

```

function [t,s,su,sd,sp,cv,wv] = sweep(A,b,L,f,d,N)

```

```

if nargin == 0      % no user arguments, assign defaults
    A = 0.0025;    % starting amplitude
    b = 0;         % amplitude modulation delta
    L = 152.4*pi/4; % length
    f = 10;        % base frequency
    d = 200;       % modulation parameter
    N = 10000;     % number of samples
elseif nargin == 1 % one user argument
    N = A;         % number of samples
    A = 0.0025;   % starting amplitude
    b = 0;        % amplitude modulation delta
    L = 152.4*pi/4; % length
    f = 10;       % base frequency
    d = 200;      % modulation parameter
else
    if nargin < 3, f = 10; end % default base frequency
    if nargin < 4, d = 200; end % default modulation
    if nargin < 5, N = 10000; end % default number of samples
end

n = N/4;          % number of points per quadrant
res = L/n;        % spatial resolution
t1 = (0:res:L-res)'; % generate points on distance vector

```

```

% generate linearly modulated amplitude vector
Amp = (A-b) + b.*(L-t1)/L;

% generate low to high frequency sweep
su = Amp .*sin(2*pi/L* t1 .*(d/L.* t1 +f));

% generate high to low frequency sweep
sd = -flipud(Amp).*sin(2*pi/L*(L-t1).*(d/L.*(L-t1)+f));

% concatenate sequences to form 4 quadrant swept wave
t = vertcat(t1,t1+L,t1+2*L,t1+3*L);
s = vertcat(su,sd,su,sd);

% calculate local slopes using finite differences
dt = diff(t);
sp = atan2(diff(s),dt);

% calculate curvature as delta slope over approximate arc length
% If the wave amplitude is small relative to the wavelength then res is a good
% approximation to arc length. Otherwise the distance between data points should be
% used, i.e. approximate arc length = sqrt(diff(t).^2 + diff(s).^2)
cv = diff(sp)./res;

% replicate end points so sequences are all of length N
sp = vertcat(sp,sp(N-1));
cv = vertcat(cv(1),cv,cv(N-2));

% find vertical axis crossings in swept wave
ss = sign(s); % sign of signal values (-1,0,+1)
ss(find(ss==0)) = 1; % change exact zeros to +1

% derivative of sign vector is nonzero only at axis crossing
ds = diff(ss)/2; % normalize derivative to (-1,0,+1)
ds = [0; ds]; % pad with leading zero
di = find(ds~=0); % extract nonzero elements

% distance between zero crossing elements in signal vector
wv = diff(di) .* mean(dt);

```

7.4.2 Deconvolution

MATLAB file: deconv_ring2.m

```
pzt_gain = 1.5942;
[req1,a,b] = textread('FTS_3V_800Hz.txt','%f%f%f','headerlines',17);

circ_length = 203.2*pi; % 152.4 for ID; 203.2 for OD
N = 80000;
[t,s,su,sd,sp,cv,wv] = sweep(0.005,0,circ_length/4,23,100,N);

wave_max = max(wv)*2 % max wavelength
wave_min = min(wv)*2 % min wavelength

speed = 20; % spindle speed in rpm
spin_rate = speed/60; % spindle speed in Hz
spin_time = 1/spin_rate; % seconds for 1 spindle rev

fq_max = (1/wave_min)*circ_length*spin_rate % maximum frequency
fq_min = (1/wave_max)*circ_length*spin_rate % minimum frequency

if fq_max > max(freq1)
    error('maximum swept wave frequency [%f] exceeds maximum actuator response
frequency', fq_max);
end

ss = fft(s, N+1);
cplx = -(a + b * i); % complex numbers of transfer function

mag = abs(cplx)/pzt_gain; % absolute magnitude
phase = (atan2(b,a)*(180/pi))-180; % system phase

freq2 = [1:spin_rate:799];
cplx2 = interp1(freq1,cplx, freq2,'spline','extrap');
% figure, semilogx(1./freq1,abs(cplx), 1./freq2,abs(cplx2),'ro'), grid;
% figure, plot(freq1, mag), grid;
% figure, plot(freq1, phase), grid;

H = [abs(cplx2(1))*sign(cplx2(1)); cplx2; conj(cplx2(end:-1:1))];

tt = [0:length(H)-1]/freq1(end)/2;
```

```

iH = ifft(H);
h = real(iH);
% figure, plot(tt,h), grid;

% x axis is number of pts, y is magnitude
% figure, plot([1:length(h)],abs(fft(h)),[1:length(H)],abs(H),'ro' ), grid;
% figure, plot([1:length(h)],unwrap(angle(fft(h))),[1:length(H)],unwrap(angle(H)),'ro'),
grid;

freq3 = [0+spin_rate:spin_rate:N*spin_rate/2];
cplx3 = interp1(freq2,cplx2, freq3,'nearest','extrap');
H3 = [abs(cplx3(1))*sign(cplx3(1)); cplx3; conj(cplx3(end:-1:1))];
% figure, plot([0:length(H3)-1]*spin_rate, abs(H3));
% figure, plot([0:length(H3)-1]*spin_rate, unwrap(angle(H3)));

in = (real(ifft(ss./H3)))*pzt_gain; % compensate for hysteresis t gain of PZTs

time = [0:spin_time/N:spin_time-spin_time/N];
figure, plot(time,[s((end)/2+1:end);s(1:(end)/2)],...
time,[in((end-1)/2+1:end-1); in(1:(end-1)/2)],'r.-'), grid;
xlabel('Time (sec)'); ylabel('Displacement (mm)');
title(sprintf('Input to FTS - ID (spin=%f Hz)',spin_rate));
axis([0 spin_time -6*10^(-3) 6*10^(-3)]);

```

7.4.3 Fiducial

MATLAB function: fiducial.m

```
% Input
% doc = depth of fiducial feature (mm)
% h = tool center offset (mm)
% tR = radius of tool (mm)
% L = circumference of ring
% N = number of points
%
% Output
% t = vector of distance samples (spatial)
% fid = vector of fiducial displacement
% theta = included angle of segment (deg)
% len = wavelength of fiducial (mm)
%
% [t,fid,theta,len] = fiducial(0.008,0.200,0.5,203.2*pi,20000);

function [t,fid,theta,len] = fiducial(doc,h,tR,L,N)

res = L/N;          % spatial resolution
siz = tR*pi;       % size of half of feature
x = (-siz:res:siz)'; % range of feature
ypos = doc * cos(2*pi*x/(2*siz)); % for positive y into the work

d = tR - h;
theta = (2 * cos(d / tR))*(180/pi); % included angle of segment (deg)

u = N-length(x); % number of points of constant values needed
z = -doc + (zeros(1, floor(u/2))); % vector of constant values

t = res*(0:1:N-1)'; % vector of distance samples
fid = vertcat(z', ypos, z', -doc); % fiducial vector

% find vertical axis crossings in swept wave
fd = fid + (0.01 - doc); % calculate wavelength based on 10µm doc
ss = sign(fd); % sign of signal values (-1,0,+1)
ss(find(ss==0)) = 1; % change exact zeros to +1

% derivative of sign vector is nonzero only at axis crossing
```

```

ds = diff(ss)/2;    % normalize derivative to (-1,0,+1)
ds = [0; ds];      % pad with leading zero
di = find(ds~=0);  % extract nonzero elements

% distance between zero crossing elements in signal vector
dt = diff(t);
len = diff(di).* mean(dt); % wavelength (mm)

MATLAB file: fid_deconv.m
% applies deconvolution to the fiducial signal

pzt_gain = 1.5942;
L = 203.2*pi; N = 20000; doc = 0.008;
[t,fid,theta,len] = fiducial(doc,0.200,0.5,L,N); % [t,fid,theta,len] = fiducial(doc,h,tR,L,N);

speed = 200;          % rpm
tmax = 60/speed;     % sec/rev
fmax = (1/(len*2))*L*(speed/60) % 680 Hz – maximum frequency

[freq,a,b] = textread('FTS_3V_800Hz.txt','%f %f %f','headerlines',17);

fid = fid + doc;      % creates an entirely positive wave
ss = fft(fid, N+1);  % convert fiducial to the frequency domain
cplx = -(a + b * i); % captured transfer function of FTS

absmag = abs(cplx)/pzt_gain; % absolute magnitude of transfer function
phase = (atan2(b,a)*(180/pi))-180; % phase of transfer function (deg)

freq2 = [1:1/3:799]; % sub-divide frequency content of transfer function
cplx2 = interp1(freq,cplx,freq2,'spline','extrap'); % interpolate

H = [abs(cplx2(1))*sign(cplx2(1)); cplx2; conj(cplx2(end:-1:1))];
% complex #s with its complex conjugate

tt = [0:length(H)-1]/freq(end)/2;
h = real(iff(H)); % convert to time domain to check interpolation

freq3 = [1/3:1/3:N/3/2]; % increase frequency range of transfer function
cplx3 = interp1(freq2,cplx2, freq3,'nearest','extrap'); % interpolate
H3 = [abs(cplx3(1))*sign(cplx3(1)); cplx3; conj(cplx3(end:-1:1))];

```

```
in = (real(iffi(ss./H3)))*pzt_gain;    % comp for hysteresis gain of PZTs
time = [0:tmax/N:tmax-tmax/N];    % based on spindle speed
figure, plot(time, fid, time, in(1:end-1), 'r.-'), grid;
    xlabel('Time (sec)'); ylabel('Displacement (mm)');
    title('Input to FTS - Fiducial'); AXIS([0 tmax -2*10^(-3) 18*10^(-3)]);
    legend('Expected', 'Adjusted');
```

7.4.4 Averaging LVDT Data

MATLAB file: `dspace_sinedata.m`

```
% Process sinewave test part measurement data
% [signal,pv] = dspace_sinedata(dspace_data,sensor_res,encoder_res,trim,zap)
% Input
% dspace_data dspace data collection structure
% sensor_res measurement sensor gain (um/volt), default = 2.4003
% encoder_res encoder resolution (counts/rev), default = 20000
% trim trim to one cycle (boolean), default = 1
% zap average successive duplicates (boolean), default = 1
% Output
% signal time, theta, displacement matrix (n x 3)
% pv peak-to-valley of data (1 x 3)

function [signal,pv] = dspace_sinedata(dspace_data,sensor_res,encoder_res,trim,zap);

error(nargchk(1,5,nargin));
if nargin < 2, sensor_res = 2.4003; end % micrometers per volt
if nargin < 3, encoder_res = 20000; end % counts per revolution
if nargin < 4, trim = 1; end % keep one complete rev (at most)
if nargin < 5, zap = 1; end % average successive duplicates

zap = (zap == 1); % force boolean args
trim = (trim == 1);

T = {dspace_data.X.Data}; % extract time series
D = {dspace_data.Y.Data}; % extract data series

time = T{1}'; % time column vector (sec)
encoder = D{1}'; % encoder column vector (counts)
signal = D{2}'; % measurement column vector (volts)

% normalize, wrap, and extract first complete cycle from encoder data
% [theta,si,sf] = rewrap(encoder,encoder_res,trim);
% when electing not to use "rewrap"
si = find(encoder == 0); % finds index of start of revolution
encoder = circshift(encoder, [-si(1)]); % shift to begin at zero counts
signal = circshift(signal, [-si(1)]);
theta = (encoder./encoder_res)*2*pi;
```

```
% build time,theta,displacement matrix (n x 3)
    %signal = [time(si:sf)-time(si) theta*2*pi signal(si:sf)*sensor_res];
signal = [time theta signal*sensor_res];

% average runs of duplicate encoder readings
if zap, signal = zapdup(signal,2); end

% find peak-to-valley of data
pv = range(signal);
```

7.4.5 Find Transfer Function

MATLAB file: xfer.m

% Calculate transfer function of two signals and plot magnitude and phase

% [fT,mag,phase,fq,h] = xfer(X,Y,rate,threshold,nstyle)

% Input

% X input signal vector

% Y output signal vector

% rate sample rate in Hz (default = 100)

% threshold cutoff value for trim filter (default = 1e-10)

% nstyle maximum vector length for stem plots (default = 502)

% Output

% fT FFT(Y) / FFT(X)

% mag absolute magnitude of fT, signal units

% phase unwrapped phase of fT, degrees

% fq frequency values for mag and phase, dc to Nyquist

% h figure object handle for magnitude and phase plots

function [fT,mag,phase,fq,h] = xfer(X,Y,rate,threshold,nstyle)

if nargin < 3, rate = 100; end

if nargin < 4, threshold = 1e-10; end

if nargin < 5, nstyle = 502; end

% calculate fft of signal vectors

fX = fft(X);

fY = fft(Y);

% set NaNs and values below threshold to zero

ffX = cplxfilt(fX,threshold);

ffY = cplxfilt(fY,threshold);

% transfer function = fft(output) divided by fft(input)

warning off MATLAB:divideByZero;

fT = ffY ./ ffX;

fT = cplxfilt(fT,threshold);

warning on MATLAB:divideByZero;

% calculate magnitude ratio and phase difference

[mag,phase,fq] = magphase(fT,rate,1,1);

```
% correct dc and Nyquist magnitude ratio scaling
mag(1) = 2*mag(1);
if ~rem(length(fT),2) % no Nyquist value for odd length vectors
    mag(end) = 2*mag(end);
end

% plot magnitude and phase vs frequency
h = plotfreq(fq,mag,phase,1,nstyle);
```

7.5 APPENDIX E – DTM PROGRAMS

Command **x** **z** **feed rate (mm/min)**

- all x and z values in mm

Faceoff.mm (constant depth of cut)

```
move 5.0 0.0 100
line 0.0 0.0 20
line 0.0 -27.0 3.2 ← based on 500 rpm, 0.5mm tool with PVtheo=10nm
move 5.0 -27.0 100
move 5.0 0.0 250
```

Raised.mm (creates a mid-section that is higher than outside edges)

```
move 2.0 0.0 100
line -0.01 0.0 10
line -0.01 -6.25 3.2 ← based on 500 rpm, 0.5mm tool with PVtheo=10nm
move 2.0 -6.25 100
move 2.0 -18.25 50
line -0.01 -18.25 10
line -0.01 -25.0 3.2
move 2.0 -25.0 100
move 2.0 0.0 250
```

- * the -0.01 values are changed to -0.019 and -0.02 in successive passes to establish the depth of cut

Wave.mm (begins wave cut within the low portion to reduce cutting forces)

```
move 2.0 -6.20 100
line 0.001 -6.20 10
line 0.001 -18.30 0.1 ← based on 20 rpm, 0.5mm tool with PVtheo= 6nm
move 2.0 -18.30 100
move 2.0 -6.20 250
```

- * the 0.001 values are changed to 0.0 for the last pass; first pass cuts 9 μ m of the wave whereas the final pass cuts the last 1 μ m of the wave

Fiducial.mm (creates a 4mm wide, 10 μ m deep fiducial)

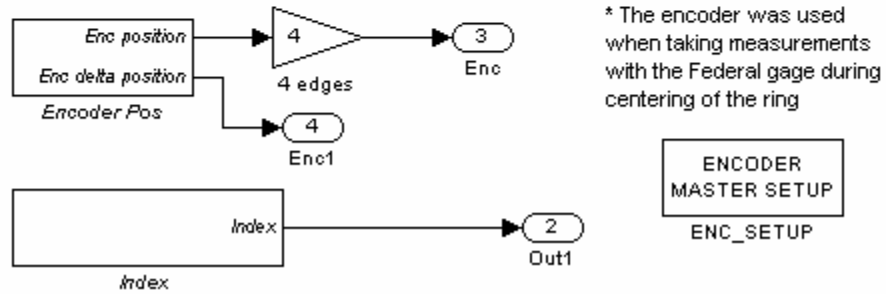
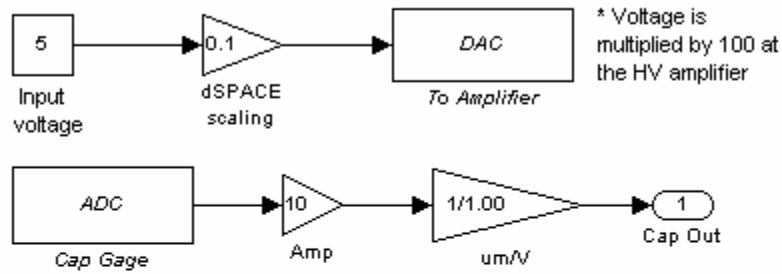
```
move 2.0 0.0 100
line -0.013 0.0 10
line -0.013 -4.0 1.0 ← based on 200 rpm, 0.5mm tool with PVtheo= 6nm
move 2.0 -4.0 100
move 2.0 0.0 250
```

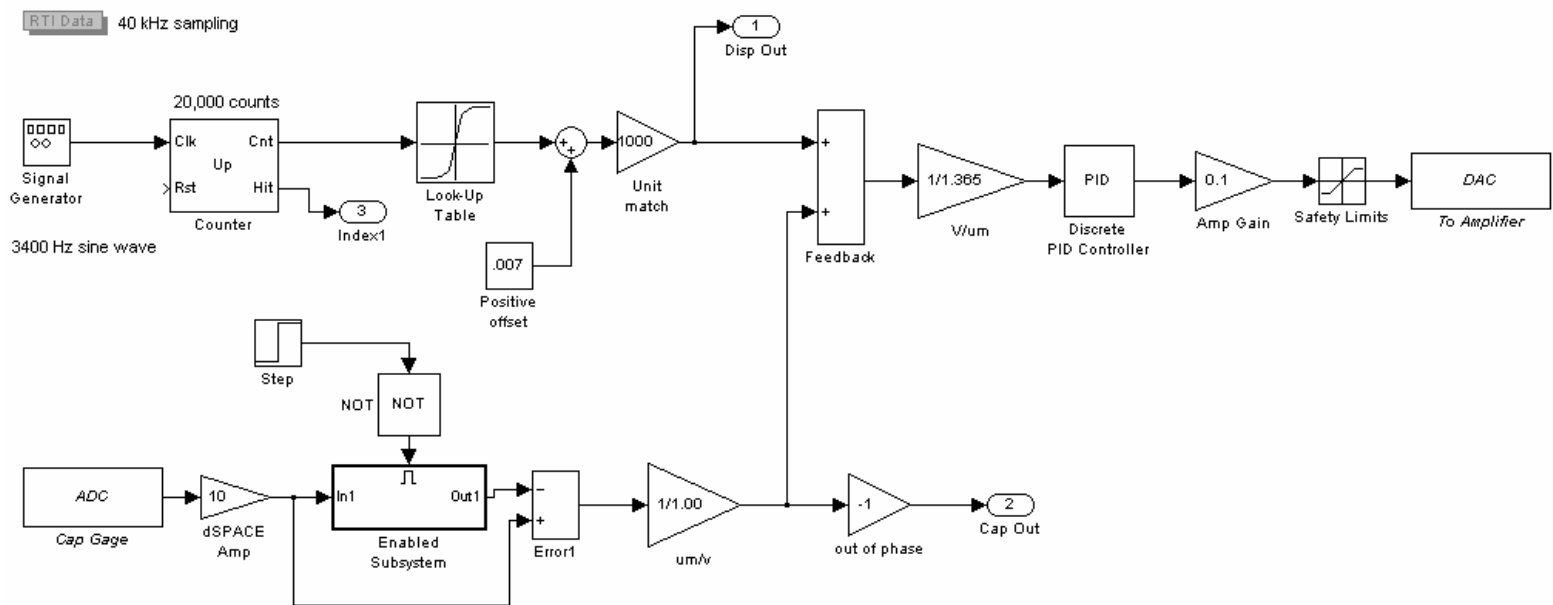
* the -0.013 values are changed to -0.014 for the finish pass (1 μ m depth of cut)

7.6 APPENDIX F – SIMULINK MODELS

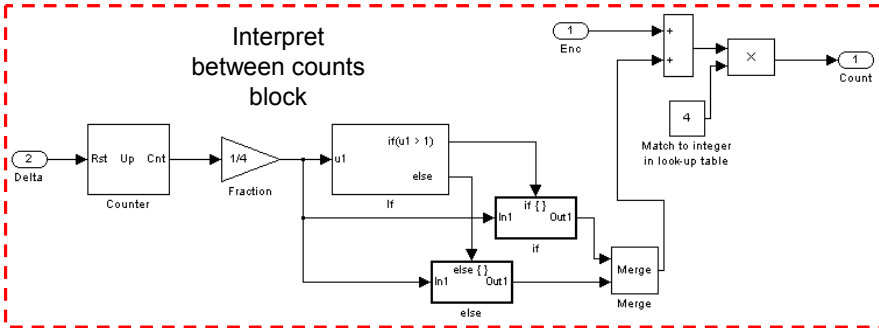
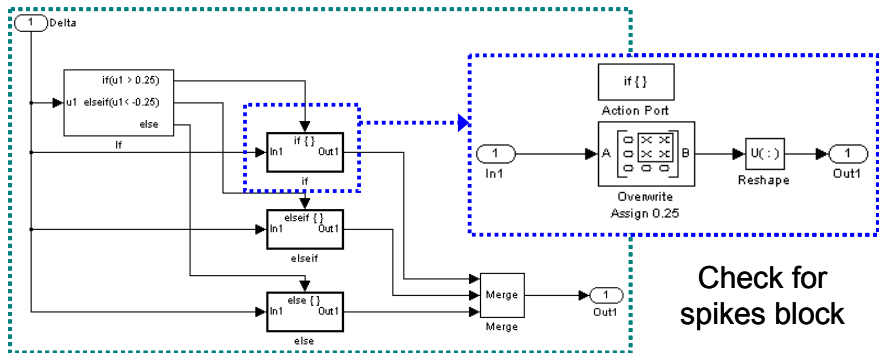
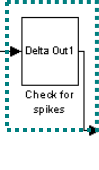
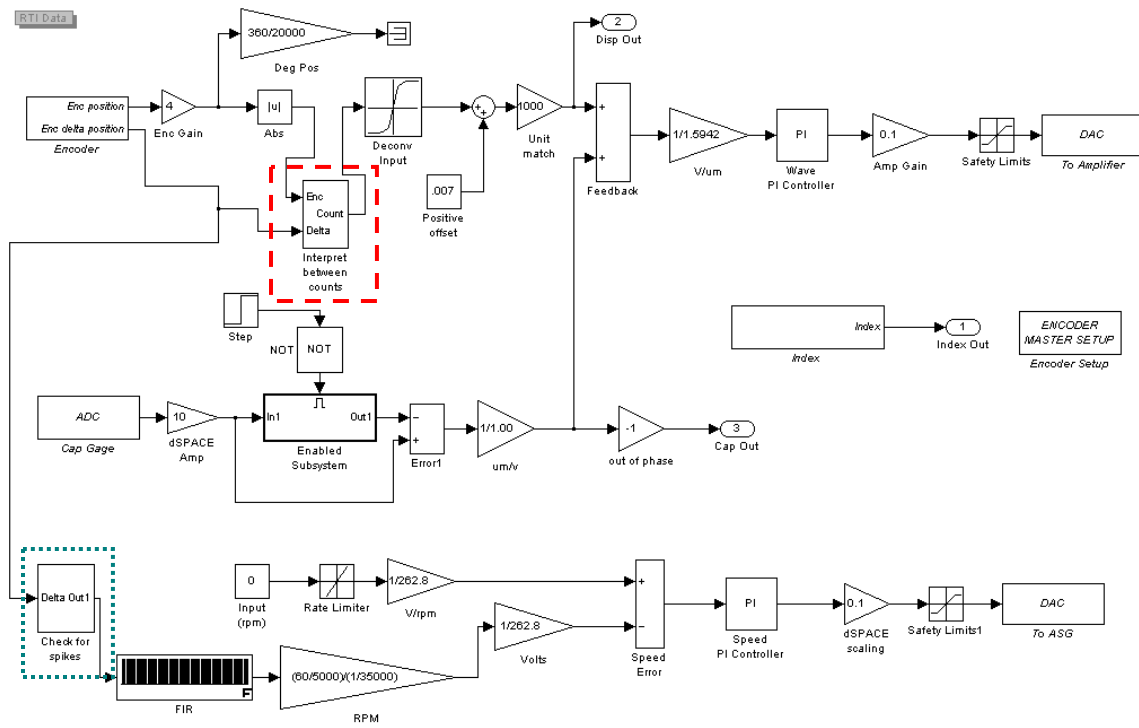
cap_center.mdl

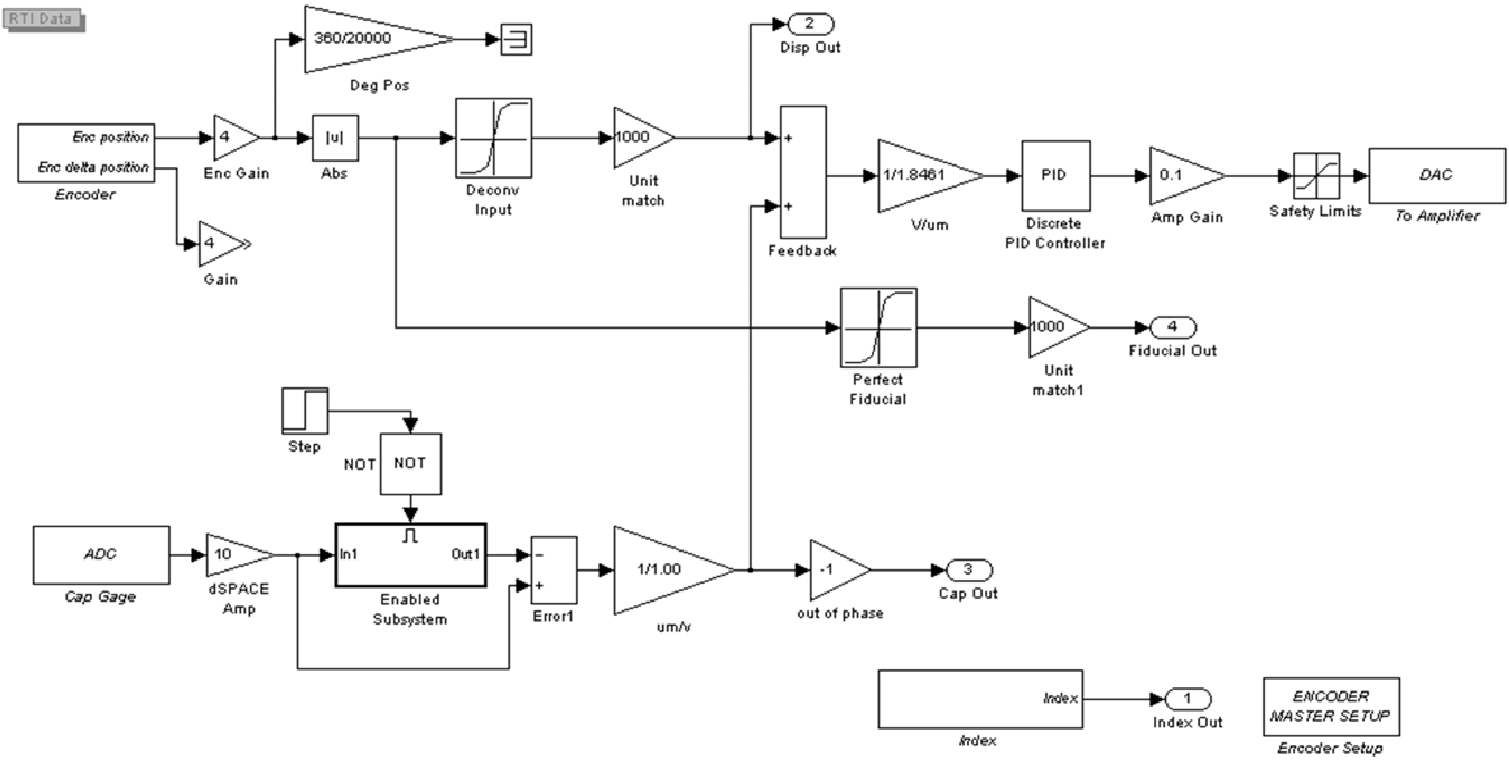
RTI Data





closed_ring_cut_interp.mdl





RTI Data

